Supplementary Materials (SM) for

Global carbon intensity of LNG value chain amid intensifying energy security and climate trade-offs

Wennan Long, Liang Jing, Zemin Eitan Liu[†], Muhammad Y. Jabbar[†], Zhenlin Chen[†],
Diego Moya, Bo Ren, Haoming Ma, James Littlefield, Farah Ramadan,
Amjaad Al-Qahtani, Dabo Guan, Xiaotao T. Bi, Joule Bergerson,
Arvind P. Ravikumar, Adam R. Brandt[*], Hassan El-Houjeiri[*], Mohammad S. Masnadi[*]
[*]Corresponding author. Email: m.masnadi@pitt.edu; hassan.elhoujeiri@kapsarc.org; abrandt@stanford.edu
[†]These authors contributed equally to this work.

This PDF file includes:

Materials and Methods

Additional Results

Validation

Figures S1 to S71

Tables S1 to S34

Contents

Materials and Methods

1 Definitions and assumptions

1.1 LNG value chain and system boundary

The LNG value chain includes the process of producing, processing, transporting, liquefaction, and regasification (*1*). Figure 1 shows the LNG value chain and defines the system boundaries used in this study. The LNG value chain has seven main LCA stages:(i) Exploration and Drilling, (ii) Production, (iii) Processing, (iv) Transmission and Transport (e.g., pipelines), (v) Liquefaction, (vi) Shipping (LNG carriers), and (vii) Regasification. More broadly, we can divide the LNG value chain into three major segments that contain the seven stages above. The upstream covers stages i through iii (Exploration and Drilling, Production, Processing). The midstream consists of stage iv (Transmission and Transport). The downstream includes stages v through vii (Liquefaction, Shipping, Regasification).

We then define two system boundaries for this study. The Well-to-Liquefaction boundary includes stages i through v, covering all processes from exploration and drilling to the production of LNG in liquid form on the liquefaction terminal. We use this boundary for LNG exporters, as it shows the LNG carbon intensity (CI) before shipment. The Well-to-Regasification boundary covers all stages of Well-to-Liquefaction plus shipping and regasification (stages vi and vii). It is used for LNG importers. This is a more relevant metric for importers because it represents the intensity of a cargo of gas ready to be injected into the consuming country's pipeline system.

1.2 Defining GHG emissions and carbon intensity

This study considers multiple greenhouse gases (GHGs) across the LNG value chain. The GHGs tracked include carbon dioxide (CO_2), methane (CH_4), and volatile organic compounds (VOCs). The VOCs consist of ethane (C_2), propane (C_3), and heavier hydrocarbons (C_4+). We also consider nitrogen (N_2) and hydrogen sulfide (H_2S) in the model, although these are not tracked as GHGs. We use the 100-year global warming potential (GWP) values from the IPCC Sixth Assessment Report (AR6), where CO_2 = 1, carbon monoxide (CO) = 2.7, CH_4 = 29.8, VOCs = 4.5, and nitrous oxide

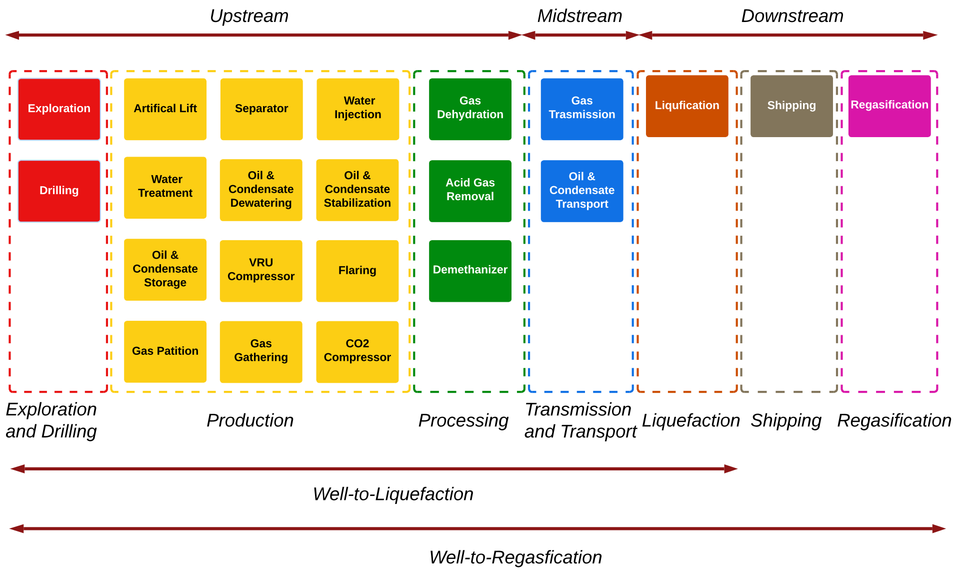

Figure 1: **LNG value chain and life cycle assessment system boundaries.** The LNG value chain has seven main stages: Exploration and Drilling, Production, Processing, Transmission and Transport, Liquefaction, Shipping, and Regasification. In this study, each stage includes multiple processes. Stages i through iii are defined as the upstream, stage iv is the midstream, and stages v through vii are the downstream. The Well-to-Liquefaction boundary covers the first five stages, while the Well-to-Regasification boundary includes all seven stages.

(N_2O) = 273.

For energy consumption, we assume all processes use produced natural gas instead of external imported gas (e.g. pipeline gas) for upstream onsite operations. All studied fields produce enough gas to support their operational needs. Some processes use grid electricity. We account for country-specific electricity CI values, which include the full upstream emissions from electricity generation, measured in gCO_2eq./btu. These country-level upstream electricity CI values are: Algeria (0.18), Australia (0.27), Indonesia (0.32), Malaysia (0.23), Nigeria (0.14), Oman (0.17), Papua New Guinea (0.13), Qatar (0.15), Russia (0.20), and the United States (0.19). The fuel combustion emissions factors and equipment efficiency values use the default value in OPGEE documentation (*2*).

Table 1 presents the combustion emission factors for key upstream processes. The equipment efficiency values are 75% for compressors and 65% for pumping units (refer to OPGEE documentation (*2*) for details). We define CI for LNG in terms of g CO_2eq./MJ using the LHV basis of the LNG. The methane loss rate (MLR) is calculated as the ratio of methane (CH_4) leaked or vented mass to the mass of methane (CH_4) produced out of the ground.

Table 1: **Combustion emission factors for LNG processing equipment.** Factors represent CO_2 emissions from natural gas and diesel combustion in typical upstream operations.

Equipment Type	Emission Factor (g/MMBtu)
Artificial Lift	71,037
Separator	59,569
Water Injection	71,037
Dewatering	59,569
Stabilization	59,569
VRU Compressor	71,037
CO_2 Compressor	71,037
Gas Dehydration	59,569
Acid Gas Removal	59,569
Demethanizer	59,569

1.3 Co-production method

We allocate emissions across different products in the LNG value chain using an energy-based method. For upstream operations described in Section 1.1, we distribute emissions among all products (crude oil, condensate, natural gas liquids (NGLs), and natural gas) based on their LHV. The midstream and downstream follow a direct allocation approach. We assign midstream emissions to natural gas products and downstream emissions to LNG. To determine the natural gas LHV after processing, we analyze the gas composition and calculate the mass-energy density of each component. All methane emissions (Section 3) are treated as upstream emissions.

1.4 Input data and method overview

This study uses data from commercial and public sources. We process this data using Python-based tools to align with our modeling framework. For the upstream, we use the Oil & Gas Production Greenhouse Gas Emissions Estimator (OPGEE) model v4.0, which is written in Python (*3*). OPGEE requires field-level data such as production volumes (oil, water, gas), gas composition, reservoir conditions (pressure and temperature), flaring rates, and production methods. We also use some of these variables to estimate field-level superemitter emissions (Section 3.2.2 and Section 3.2.3). All time-dependent data (production volumes, flaring rates, methane emissions) are averaged annually at the field level. Figure 2 shows that for the complete value chain analysis, three connected models written in Python are used: OPGEE for upstream emissions, a transmission model for pipeline network emissions, and an LSR model for liquefaction, shipping, and regasification emissions. The full value chain LCA results combine outputs from all three models.

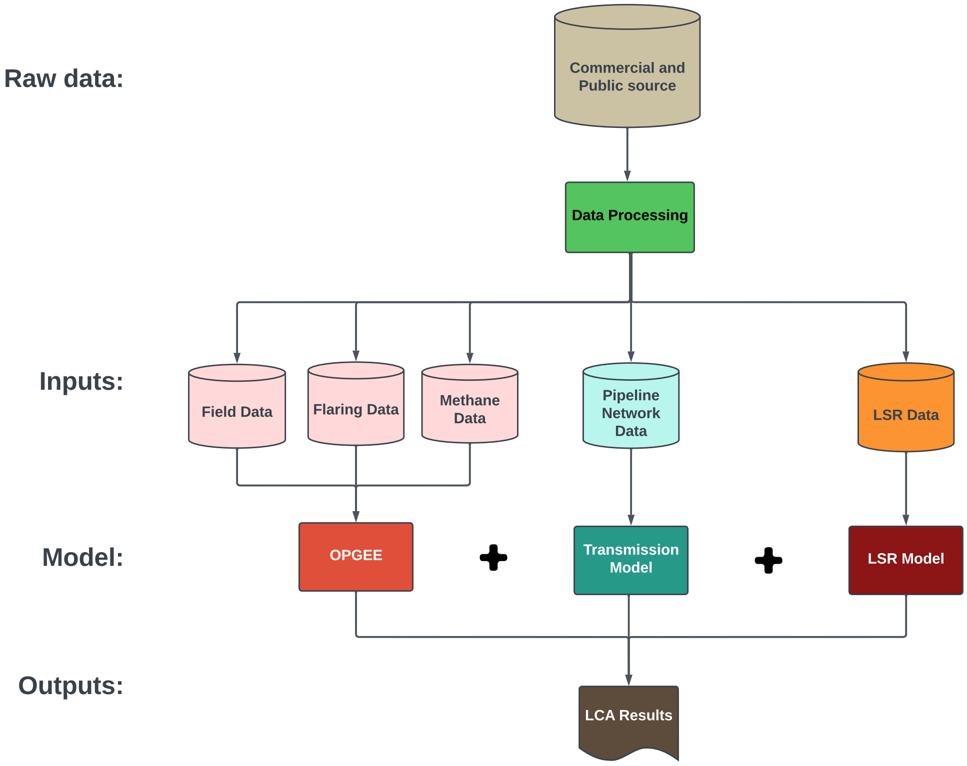

Figure 2: **Data sources and processing framework for LNG value chain analysis.** The framework integrates commercial and public data sources through Python-based processing tools. Field-level data include production volumes, gas composition, and operational parameters. The analysis uses three models: OPGEE for upstream emissions, a transmission model for midstream emissions, and an LSR (liquefaction, shipping, regasification) model for downstream emissions. All data represent yearly averages at the field level.

2 Upstream

2.1 LNG fields

We modeled 2,454 LNG fields in the top ten LNG exporters, which account for 85% of global LNG supply. We classify these fields into two categories: US fields and non-US fields. For US fields, we define LNG fields as gas fields with a gas-to-oil ratio (GOR) greater than or equal to 10,000 scf natural gas produced per barrel of crude oil produced (scf/bbl). Fields with GOR less than 10,000 scf/bbl are classified as oil fields (see the method used by Masnadi et al. 2018 (*4*)). We assume that all US LNG comes from gas that is produced and processed from gas fields. US gas differs from other regions due to its transportation infrastructure. Unlike other countries where we can identify direct connections between specific fields and LNG facilities, US gas moves through an interconnected pipeline transmission system. This network complicates the traceability of gas from specific fields to LNG terminals, requiring us to treat US fields differently in this study (Section 4). This study simulates all gas fields in the US, which account for 84% of US gas production in 2022.

For non-US fields, we use commercial datasets to identify the source fields for LNG production. In these cases, LNG can come from both gas fields and oil fields. This study includes 25 oil fields that supply LNG: 1 in Indonesia, 19 in Nigeria, 1 in Russia, and 4 in Malaysia. This means that LNG from these countries may be produced from associated gas from oil fields, unlike the US case, where we assume LNG comes exclusively from gas fields.

As shown in Table 2, the United States accounts for 92% (2,252) of total fields in this study. Of the 2,454 total fields, 72 are offshore fields, concentrated in Malaysia (26 fields), Australia (14 fields), Nigeria (14 fields), and Indonesia (8 fields). Qatar's LNG production comes exclusively from offshore fields. The table also shows the average daily production rates of oil and natural gas from these LNG fields. Production rates are measured in million barrels per day (MMbbl/day) for oil and billion cubic feet per day (bcf/day) for natural gas. The United States has the highest production volumes, accounting for 42% of oil production (1.0 MMbbl/day) and 65% of gas production (110 bcf/day) among the studied countries. Australia and Qatar follow as major gas producers, each producing approximately 13 to 14 bcf/day. Together, these ten countries produce 2.4 MMbbl/day of oil and 170 bcf/day of natural gas from the fields that supply LNG exports.

Table 2: **LNG field distribution and production rates by country.** This table shows the number of fields (total and offshore) and daily production rates for oil (MMbbl/day) and natural gas (bcf/day) from modeled fields in each country. The United States dominates in both field count and production volumes, while Malaysia has the highest number of offshore fields.

Country	**Total Fields**	**Offshore Fields**	**Oil Rate** (MMbbl/day)	**Gas Rate** (bcf/day)
Algeria	21	0	0.14	8.4
Australia	52	14	0.19	14
Indonesia	13	8	0.056	3.2
Malaysia	44	26	0.098	4.9
Nigeria	49	14	0.31	4.0
Oman	7	0	0.065	3.1
Papua New Guinea	4	0	0.023	1.3
Qatar	8	8	0.41	13
Russia	4	2	0.11	7.4
United States	2,252	0	1.0	110
Total	2,454	72	2.4	170

2.2 Estimated ultimate recovery

Estimated Ultimate Recovery (EUR) is the total amount of hydrocarbon (oil and gas) expected to be economically recovered from a field over its lifetime. In this study, we use EUR to amortize the energy consumption and associated emissions from exploration, drilling, and land use activities to the year of analysis. We collect EUR data for both oil (million barrels) and gas (billion cubic feet) for all fields. We convert volumetric EUR to energy units using LHV to calculate the cumulative energy content.

For oil, the energy content is calculated using Equation 1:

$$\mathrm{EUR}_{\mathrm{oil,energy}} = \mathrm{EUR}_{\mathrm{oil}} \times \rho_{\mathrm{oil}} \times \mathrm{LHV}_{\mathrm{oil}} \tag{1}$$

where ρ_{oil} is oil density and $\mathrm{LHV}_{\mathrm{oil}}$ is the mass energy density of oil.

For gas, the energy content calculation accounts for gas composition as shown in Equation 2:

$$\mathrm{EUR}_{\mathrm{gas,energy}} = \mathrm{EUR}_{\mathrm{gas}} \times \sum_i (x_i \times \rho_i \times \mathrm{LHV}_i) \tag{2}$$

where x_i is the molar fraction of component i, ρ_i is the density of component i at standard temperature and pressure, and LHV_i is the mass energy density of component i.

2.3 Gas composition

We model seven gas components as inputs to OPGEE (*2*): nitrogen (N_2), carbon dioxide (CO_2), methane (C_1), ethane (C_2), propane (C_3), heavier hydrocarbons (C_4+), and hydrogen sulfide (H_2S). For US fields, we derive gas compositions using inverse distance weighting (IDW) interpolation from United States Geological Survey datasets (*5*). The interpolated composition $C_{i,j}$ for component i at field j is calculated using Equation 3:

$$C_{i,j} = \frac{\sum_k w_{jk} c_{i,k}}{\sum_k w_{jk}} \tag{3}$$

where w_{jk} is the inverse distance weight between field j and measurement point k, and $c_{i,k}$ is the measured composition of component i at point k. The weight is calculated according to Equation 4:

$$w_{jk} = \frac{1}{d_{jk}^p} \tag{4}$$

where d_{jk} is the haversine distance between locations and p is the power parameter (set to 2 in this study).

For non-U.S. countries, we handle missing gas composition data with a hierarchical method. We first use gas composition data from individual fields if available. If field-level data are not available, we rely on country-average values. When neither field nor country data exist, we apply a global average. Methane composition varies substantially between countries, from 52.1% in Nigeria to 86.8% in Indonesia (Figure 3). Nigeria's notably low methane content and high content of heavier hydrocarbons (C_4+ at 32.9%) results from limited data; only one field (Ibewa-1) has complete data available. Australia, Indonesia, and Malaysia have relatively high acid gas levels, with carbon dioxide concentrations above 5% (5.42%, 6.72%, and 6.71%, respectively). Russia has the lowest carbon dioxide content (0.810%) but the highest hydrogen sulfide content (1.73%). Nitrogen content ranges from 0.470% in Australia to 6.00% in Algeria. Ethane and propane levels are similar across most countries, though Indonesia has slightly lower concentrations.

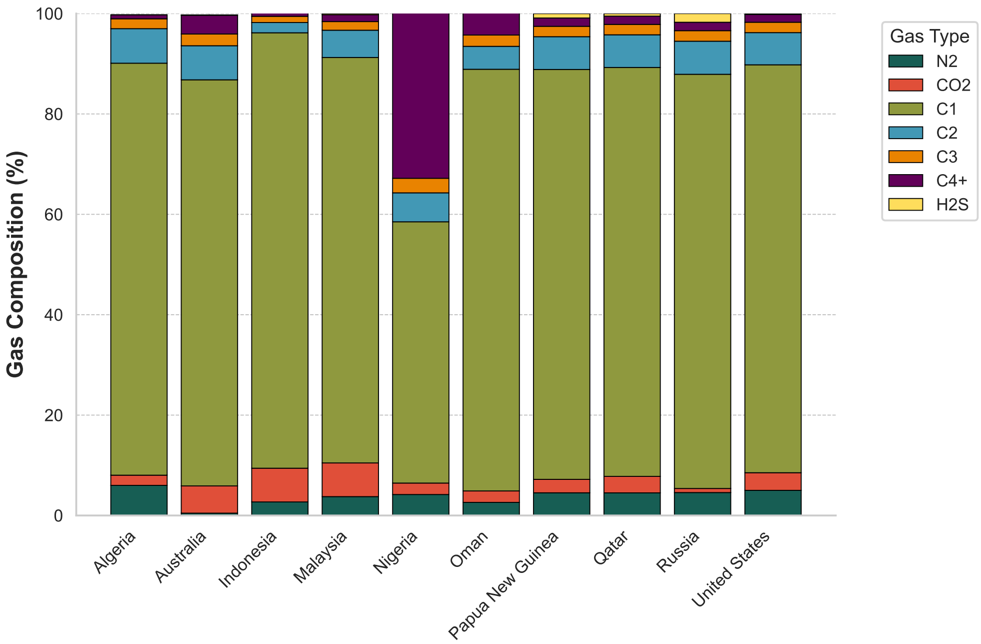

Figure 3: **Gas composition distribution across LNG exporters.** Molar fractions of seven gas components (N_2, CO_2, C_1, C_2, C_3, C_4+, H_2S) in natural gas from LNG fields. Values represent production-weighted averages for each country. Higher C_4+ content in Nigerian fields reflects limited composition data availability. Australia, Indonesia, and Malaysia show notable acid gas (CO_2 and H_2S) content exceeding 5%.

2.4 Acid gas capture

Acid gases CO_2 and H_2S must be removed to very low concentrations in LNG systems. H_2S is corrosive and poisonous, and is typically removed from all gas systems. CO_2 must be removed to very low levels in LNG systems, beyond that practiced for natural gas systems in general, because its presence in LNG would cause rapid buildup of dry ice (CO_2 in solid form) in heat exchangers and other equipment. Thus, LNG requires essentially complete removal of both of these species. We model fields known to inject captured CO_2 underground. If capture status is unknown, we assume CO_2 is vented. All H_2S removal is modeled as conversion to elemental sulfur, either disposed of or sold commercially.

This study considers fields equipped with acid gas removal and carbon capture systems at processing plants handling at least 1,000 tonnes of CO_2 daily. The highest CO_2 concentrations occur in the United States, notably at Wyoming's Big Piney-LaBarge field region. Lake Ridge and Fogarty Creek fields here contain 59.9% and 61.9% CO_2, respectively. CO_2 from these fields is captured and stored at the LaBarge/Shute Creek Gas Plant. In Alaska, high-CO_2 fields such as Prudhoe Bay (11.9%), Endicott (11.1%), and Northstar (10.6%) manage acid gases by reinjecting them underground (*6–9*).

In Australia, the Gorgon project (13.6% CO_2) and Ichthys field (10.5% CO_2) have carbon capture facilities at their processing plants. Algeria's Rhourde Nouss field (7.5% CO_2) also utilizes carbon capture technology. Qatar implements systematic CO_2 management across its LNG facilities. At Ras Laffan Gas Processing Plant, CO_2 levels range between 2.5% and 5.0%. The Qatargas and RasGas facilities use methods including injection into saline aquifers, processing around 2.2 million tonnes of CO_2 annually.

2.5 Subsurface and surface pressure

This study analyzes both subsurface pressures (reservoir and bottomhole pressures) and surface pressures (wellhead and pipeline pressures). For U.S. LNG fields, we use direct measurements of bottomhole pressure. For fields outside the U.S., we calculate bottomhole pressures using well diameter, productivity index, and reservoir pressure, following methods described in OPGEE documentation (*2*).

Wellhead pressure must equal or exceed pipeline inlet pressure to maintain proper gas flow into transportation systems. We set default pipeline inlet pressures at 800 psi for gas fields (gas-to-oil ratio, GOR ≥ 10,000 scf/bbl) and 500 psi for oil fields (GOR < 10,000 scf/bbl) (*10, 11*). For gas fields, wellhead pressure (P_{wh}) is determined by reservoir pressure (P_r) according to Equation 5:

$$P_{wh} = \begin{cases} P_r & \text{if } P_r < 800 \text{ psi and GOR} \geq 10,000 \\ 800 & \text{if } P_r \geq 800 \text{ psi and GOR} \geq 10,000 \end{cases} \tag{5}$$

For oil fields, we apply a similar rule with a 500 psi threshold as shown in Equation 6:

$$P_{wh} = \begin{cases} P_r & \text{if } P_r < 500 \text{ psi and GOR} < 10,000 \\ 500 & \text{if } P_r \geq 500 \text{ psi and GOR} < 10,000 \end{cases} \tag{6}$$

When wellhead pressures are lower than required pipeline pressures, gas compression is used to increase pressure. We assume the gas reaches temperatures of 197°F after compression for gas fields and 150°F for oil fields. Post-compression pressures match pipeline inlet pressures of 800 psi for gas fields and 500 psi for oil fields.

2.6 OPGEE and process flow diagram

OPGEE is an engineering-based life cycle assessment model that calculates upstream CI in oil and gas operations. Since its first release in 2012 (*12, 13*), OPGEE has developed through four versions with expanding capabilities. Version 1 created the first systematic LCA framework for oil and gas analysis. Version 2 (2018) added exploration emissions, embodied energy, CO_2 enhanced oil recovery, and heavy oil production methods (*14*). Version 3 (2019) introduced detailed equipment-level emission calculations and improved AGR modeling (*2, 15, 16*). The current Version 4 (2023), completely rewritten in Python, with significant modeling improvements, bug fixes, and standardization of mass tracking. Version 4 of OPGEE includes specific improvements for analyzing gas fields. Gas fields make up over 99% of LNG fields in this study (*3*).

Figure 4 shows how OPGEE models the processing of oil, gas, and water in LNG fields. The diagram tracks these three fluids (shown as colored arrows) from underground through various processing steps (shown as boxes). Processing units with dashed outlines incorporate two types of methane emissions: non-superemitter emissions modeled from Section 3.1 and superemitter emissions from Section 3.2. OPGEE ensures mass balance by limiting total emissions to available methane at each processing unit.

Initially, a mixture of oil, gas, and water is extracted and directed through pumping systems and separation units. After separation, each fluid follows distinct treatment processes: oil undergoes water removal and stabilization before storage; water is treated and reinjected underground; gas passes through water removal, acid gas removal, and compression stages before liquefaction into LNG. At the system boundary, the model measures oil, LNG, and natural gas liquids (NGLs) to calculate CI.

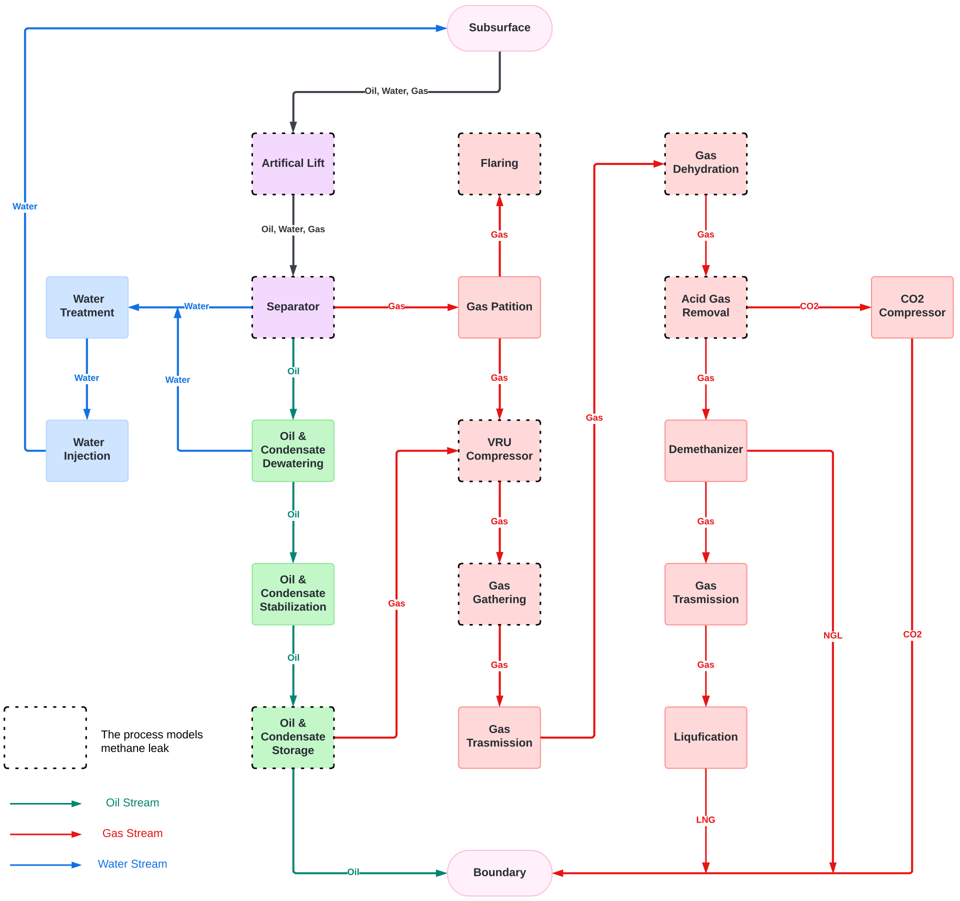

Figure 4: **Process flow diagram for LNG field surface operations in OPGEE.** Boxes show processing units, with dashed outlines marking units that include methane emissions calculations. Arrows indicate fluid movement: oil (green), gas (red), and water (blue). The diagram shows how mixed fluids from underground are separated and processed into final products.

3 Methane

3.1 Estimation of non-superemitter emissions

This section describes our methodology for quantifying non-superemitter emissions (emissions below 100 kg CH_4/hour), which contributes approximately 13% of well-to-regasification emissions in the global LNG value chain. We build on the component-level fugitives model developed by Rutherford et al. (*17*). This bottom-up approach combines component-level emissions data, component counts, and a fraction of components emitting to produce an equipment-level emissions factor. We refine Rutherford's methodology by implementing a more precise classification threshold, using a gas-to-oil ratio (GOR) of 10,000 scf/bbl to differentiate oil and gas fields compared to the Rutherford et al. 100,000 scf/bbl threshold. We examine eight field measurement studies from Rutherford's methodology. Most studies directly classify fields as oil or gas fields. However, the API 1993 study (*18*) classified fields based on API gravity. It defines light crude as those with API gravity ≥ 20 and heavy crude with API gravity < 20.

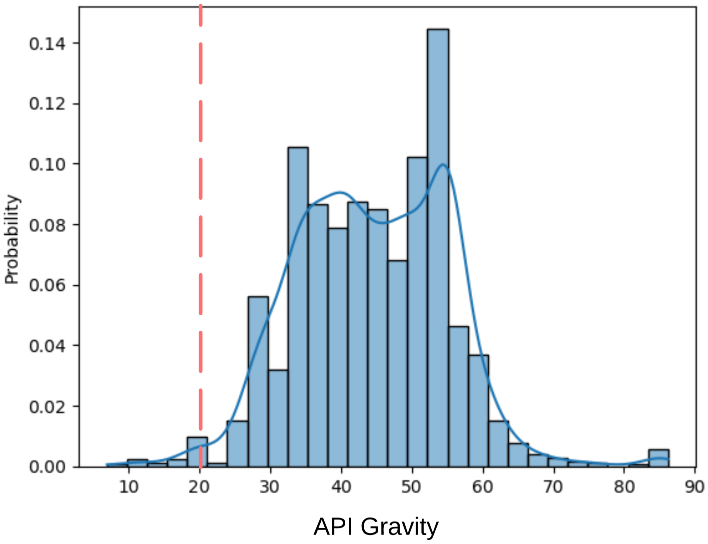

Figure 5: **Distribution of API gravity in gas fields.** The histogram shows the API gravity distribution for all gas fields in the dataset. The red dashed line indicates the API gravity threshold of 20 used in the API 1993 study to differentiate light crude from heavy crude production sites. The distribution demonstrates that over 99% of gas fields have API gravity above this threshold, validating the classification of light crude sites as gas fields.

Figure 5 shows this study of API gravity distribution across gas fields. This analysis supports the API classification approach. Over 99% of gas fields have an API gravity greater than 20. This indicates that API 1993 light crude figures are likely to be more representative of gas-oil-coproduction operations or gas fields in our model. Using the updated component counts in Tables 27 and 28, we calculate equipment-level emissions factors for oil and gas fields separately. For oil fields (Figure 6), most equipment shows similar emission distributions below 100 kg CH_4/day. However, tanks exhibit the highest emission factors, reaching up to 400 kg CH_4/day. Tanks as large sources is a well established pattern in the methane literature.

We compared our results with Rutherford et al.'s study using cumulative distribution function (CDF) differences. For oil fields, our study shows higher CDF differences at low emission rates

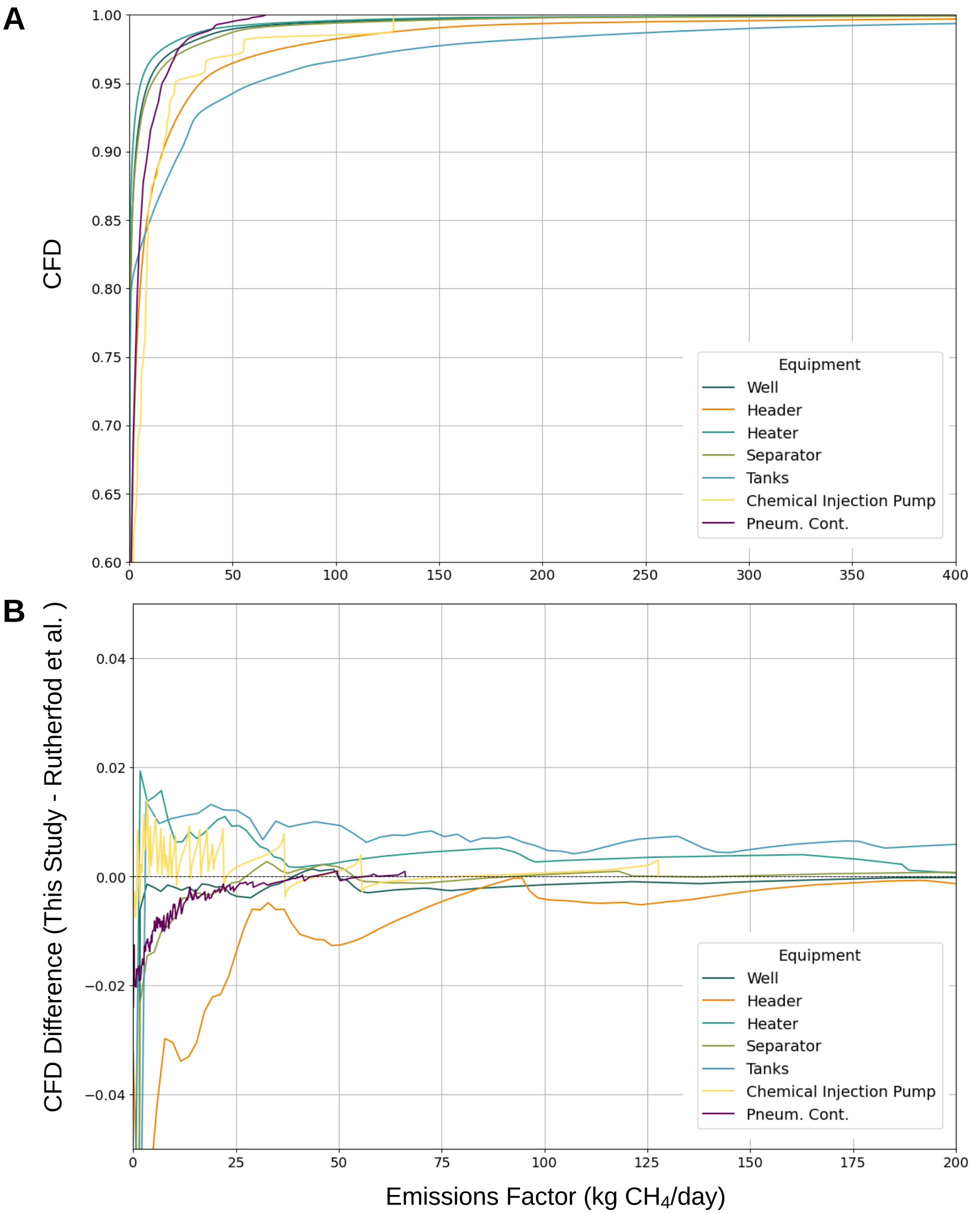

Figure 6: **Equipment emissions factor in oil fields.** (**A**) Cumulative distribution functions of equipment emission rates. Most equipment shows emissions below 100 kg CH_4/day, while tanks reach up to 400 kg CH_4/day. (**B**) CDF differences with Rutherford et al.'s study reveal equipment-specific patterns: higher CFD difference of low emissions for heaters and chemical injection pumps, lower for wells and pneumatic controllers.

(less than 25 kg CH_4/day) for heaters, tanks, and chemical injection pumps. We found lower CDF differences for wells and pneumatic controllers. Headers in our study tend toward higher emission factors. For gas fields (Figure 7), most equipment emissions concentrate below 150 kg CH_4/day and reach maximum values of 250 kg CH_4/day. Tanks show a more gradual distribution, indicating more frequent high emissions.

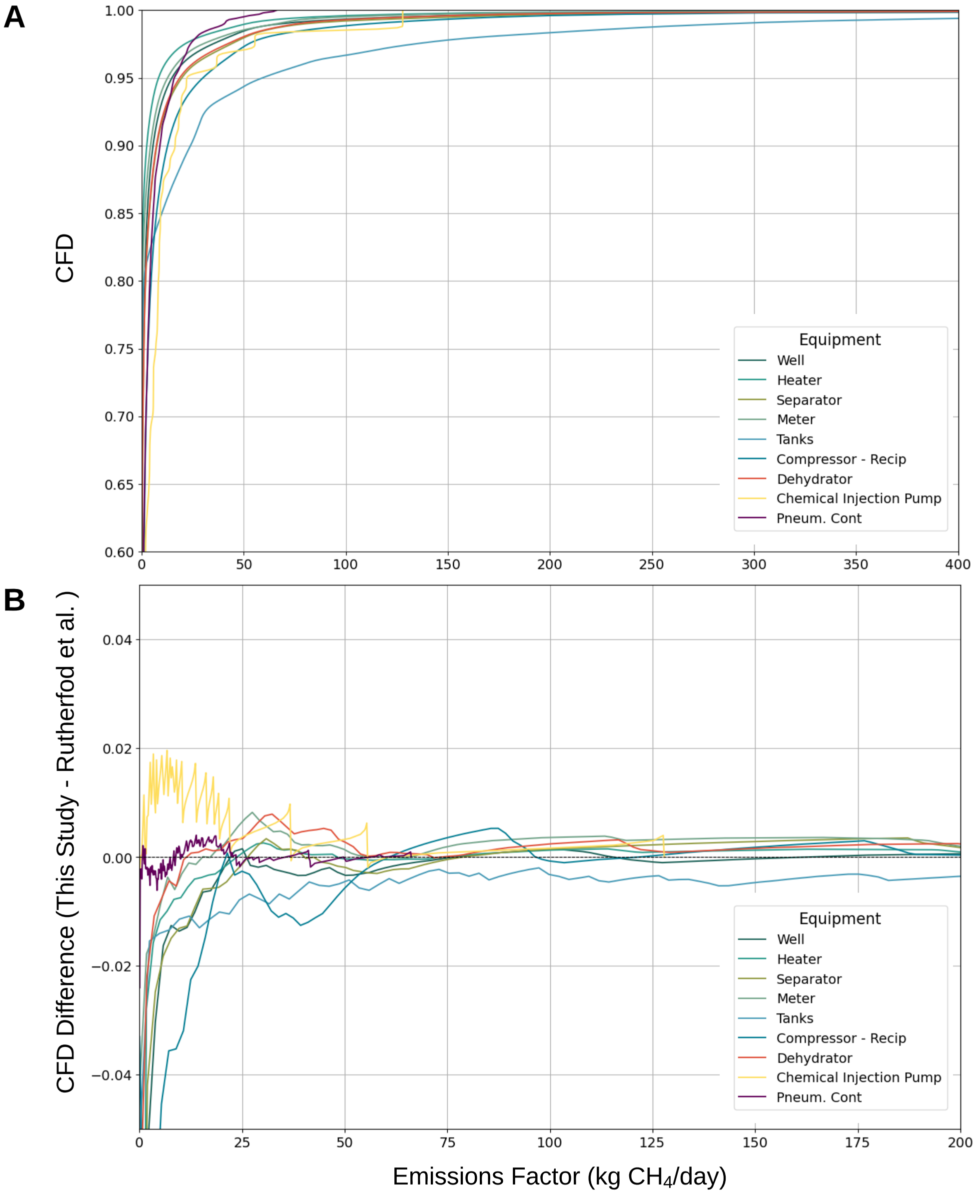

Figure 7: **Equipment emissions factor in gas fields.** (**A**) Cumulative distributions show most equipment emissions below 150 kg CH_4/day, with tanks showing a more gradual increase, indicating frequent high emissions. (**B**) CDF differences show varying patterns by emission rate: higher CFD difference for chemical injection pumps at low rates, higher for dehydrators and meters at higher rates, and consistently lower for tanks.

The CDF comparison for gas fields reveals different patterns. At low emission rates (less than 10 kg CH_4/day), only chemical injection pumps show higher CDF differences. Dehydrators, meters, and separators show higher CDF differences at higher emission factors. Tanks consistently show lower CDF differences, suggesting our study predicts higher tank emissions. Both systems strongly agree with Rutherford et al.'s results for emission factors above 175 kg CH_4/day.

In this study, we use Monte Carlo simulations with 5,000 realizations to estimate equipment emissions factors for oil and gas fields. While the detailed methodology can be found in Rutherford et al. (*17*), we present the key points of our approach here. It is important to note that while the exact number of equipment units per field is not directly known, we do know the number of wells per LNG field. Therefore, we assume that equipment counts scale with the number of wells using the same scaling factors provided in Supplementary Table 3 of Rutherford et al. (*17*). This approach allows us to estimate equipment distributions across fields of varying sizes based on their well counts.

While this approach is the only one applicable given current datasets, it may introduce some difficulties. For example, if some regions tend to have fewer equipment pieces per well, then the scaling factors here could over-estimate equipment. Absent comprehensive global equipment databases, this is the only currently feasible approach. In the future, counting of equipment via remote sensing may become more prevalent.

The emission rate $E_{i,j}$ for equipment i at well site j is calculated as shown in Equation 7:

$$E_{i,j} = EF_i \times AF_i \times I_{i,j} \tag{7}$$

where EF_i is the equipment emissions factor, AF_i is the activity factor, and $I_{i,j}$ is a binary indicator (0 or 1) determining equipment presence based on random sampling.

We differentiate between oil and gas fields using the GOR as defined in Equation 8:

$$\text{Field Type} = \begin{cases} \text{Gas Fields,} & \text{if GOR} > 10,000 \\ \text{Oil Fields,} & \text{if GOR} \leq 10,000 \end{cases} \tag{8}$$

Total emissions E_{total} are calculated by summing across all equipment types and wells as shown in Equation 9:

$$E_{\text{total}} = \sum_{j=1}^{N_{\text{wells}}} \sum_{i=1}^{N_{\text{equipment}}} E_{i,j} \tag{9}$$

After running 5,000 Monte Carlo simulations for all LNG fields, we analyzed the relationship between equipment emissions and producer counts. Figure 8 shows that equipment emissions increase log-linearly with producer counts. This relationship follows the general form shown in Equation 10:

$$\log_{10}(E) = m \log_{10}(P) + b \tag{10}$$

where E is the equipment emission rate (kg CH_4/day), P is the producer count, and m and b are the slope and intercept parameters, respectively.

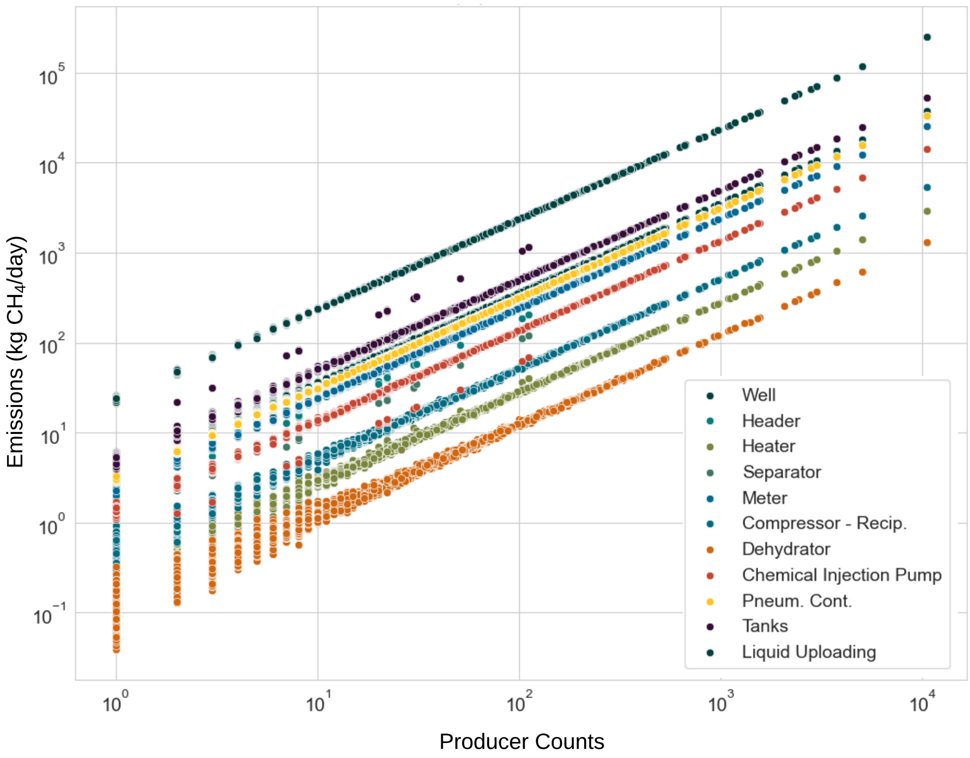

Figure 8: **Equipment emissions scale with producer counts.** Log-log plot shows linear relationships between simulated emissions and producer counts for different equipment types, averaged over 5,000 Monte Carlo realizations. Liquid uploading shows the steepest scaling (slope = 23.78), while dehydrators show the shallowest (slope = 0.12).

Table 3 shows these parameters for each equipment type. The linear correlations are strong across all equipment types (r-value = 1.0). Liquid uploading shows the steepest slope (23.78), followed by tanks (5.01) and wells (3.59).

Beyond mean emission rates, we analyze how uncertainty in equipment emissions scales with

Table 3: **Equipment emission scaling parameters.** Linear regression results for log-transformed emissions versus producer counts, showing slope and intercept values for each equipment type. All correlations show r-value = 1.0.

Equipment	**Slope**	**Intercept**
Liquid Uploading	23.78	-0.35
Tanks	5.01	1.39
Well	3.59	-0.30
Separator	3.19	-0.51
Pneum. Cont.	3.16	0.03
Meter	2.43	0.10
Header	1.83	0.57
Chemical Injection Pump	1.38	-0.21
Compressor	0.52	0.02
Heater	0.28	0.03
Dehydrator	0.12	-0.01

producer counts. Figure 9 shows the relationship between emission uncertainty and producer counts for each equipment type. We define uncertainty as the difference between the 97.5th and 2.5th percentile values. Similar to mean emissions, uncertainties show a logarithmic relationship with producer counts as expressed in Equation 11:

$$\log_{10}(U) = m \log_{10}(P) + b \tag{11}$$

where U is the emission uncertainty (tonne CO_2eq./day), P is the producer count, and m and b are fitting parameters shown in Table 4.

Uncertainties scale consistently with producer counts for fields with more than 10 producers (R-values > 0.8). Smaller fields show higher uncertainty variability. This occurs because individual component variations have a greater relative impact in smaller fields. In larger fields, extreme results on an equipment or well basis tend to average away.

We integrate equipment-level emission rates into the OPGEE process flow (Figure 4) by allocating emissions to specific processes marked with dashed outlines. The allocation combines related equipment emissions into process-level rates. For example, separation emissions include contributions from separators, pneumatic controllers, and meters as shown in Equation 12:

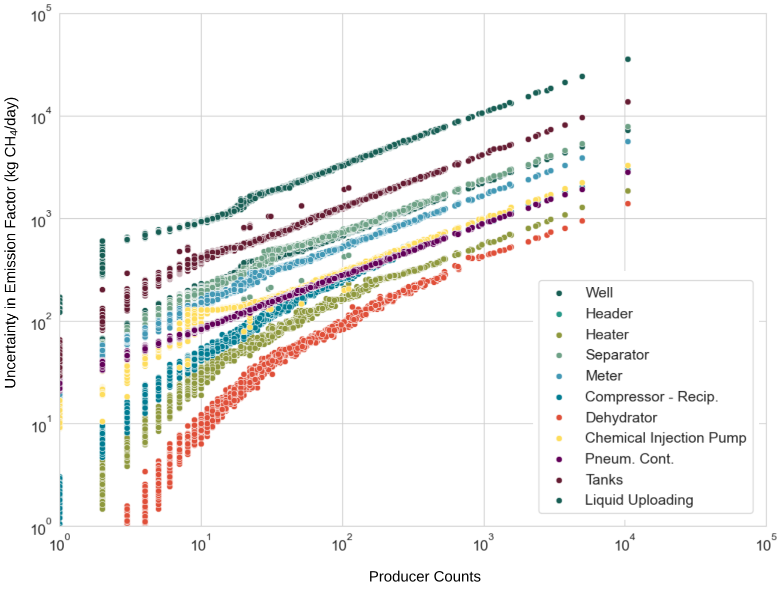

Figure 9: **Equipment emission uncertainties increase with producer counts.** Log-log plot shows relationships between emission uncertainties and producer counts for different equipment types. Headers and liquid uploading show the steepest uncertainty scaling (slopes of 6.42 and 5.37), while dehydrators and heaters show more modest increases (slopes of 0.21 and 0.29). Fields with fewer than 10 producers show higher uncertainty variability.

Table 4: **Equipment uncertainty scaling parameters.** Linear regression results for log-transformed uncertainties versus producer counts, showing slope and intercept values. All correlations show R-values above 0.8.

Equipment	Slope	Intercept
Header	6.42	101.56
Liquid Uploading	5.37	1188.68
Tanks	2.10	452.36
Separator	1.19	245.53
Well	1.11	245.29
Meter	0.85	183.14
Chemical Injection Pump	0.50	108.68
Compressor	0.47	71.97
Pneum. Cont.	0.43	102.56
Heater	0.29	45.10
Dehydrator	0.21	22.51

$$E_{\text{separation}} = E_{\text{separator}} + E_{\text{pneumatic}} + E_{\text{meter}} \tag{12}$$

We use mass tracking approaches built into the fundamentals of OPGEE modeling. Each downstream process sees an incoming stream that accounts for any leaks already occurring upstream of that unit. For example, the separator sees a gas stream that already accounts for any losses at the wellhead.

Table 5: **Equipment to process emissions allocation.** Mapping of equipment-level emission rates to OPGEE process units for methane emissions calculations.

Process	**Equipment**
Artificial Lift	Wells, Headers, Chemical Injection Pumps
Oil & Condensate Storage	Tanks
Oil & Condensate Dewatering	Heater
Gas Dehydration	Dehydrator
Separation	Separator, Meter, Pneum.Cont.
VRU Compressors, CO_2 Compressors	Compressor

Table 5 shows how other equipment emissions are combined into process-level emissions. To maintain mass balance, we limit process emissions to available methane using Equation 13:

$$E_{\text{process}} = \min(E_{\text{equipment}}, F_{\text{CH}_4}) \tag{13}$$

where E_{process} is the final process emission rate, $E_{\text{equipment}}$ is the combined equipment emission rate, and F_{CH_4} is the methane flow rate entering the process. This approach ensures that predicted emissions cannot exceed physically available methane, and our approach cannot ever result in a non-physical loss rate exceeding 100%.

In addition to component-level fugitives, we model emissions from AGR, flaring, and gas gathering systems. We use site-level models for AGR units and gas gathering systems as detailed in the OPGEE documentation (*14*). For methane emissions from flaring, we use a fixed methane non-combustion ratio of 7%. This value is based on Zhang et al.'s study and is supported by further empirical work from the Kort et al.'s group (*19, 20*).

This value includes both incomplete combustion of hydrocarbons in the flame (so-called stripping of hydrocarbons from the flame front) and extinguished or unlit flares. Empirical work using airplane surveys of 100s of flares (*20*) suggests that both of these sources of methane are important, and that both of them tend to increase with wind speed. That is, as wind speed increases, the chance of a flare becoming unlit increases, as does the rate at which hydrocarbons are stripped from the flame region before combustion. Extensive work in wind tunnels and other flare experimental work supports these relationships. Note that this loss rate of 7% is significantly higher than that typically assumed by governments.

3.2 Estimation of superemitter emissions

We used multiple methods to estimate large sources of methane, so-called methane superemitters. Methane super emitters are now commonly defined as point sources of methane releasing at least 100 kg of CH_4 per hour. These sources significantly contribute to global methane emissions.

Because of their very dispersed and global nature, remote sensing via airplane and satellite has emerged as the key method of detecting superemitters. A few major challenges exist though:

1. They tend to be very infrequent, occurring at a small number of sites in any given "snapshot" picture of emissions. This means that large sample sizes are required to obtain evidence around size distribution and frequency.
2. They tend to not be included in the datasets used to generate emissions factors, like those used in the OPGEE model above, based on earlier regulatory work. Those surveys typically examine a small number of sites in great detail, thus almost by definition missing very infrequent but large events.
3. Superemitters can occur offshore, where remote sensing methods generally fail (see below)
4. Superemitters can occur in cloudy regions, which obscures the methane because the relevant wavelengths are not transmitted through clouds.
5. Superemitters can occur regions with poor light availability or low sun angle, which makes observing difficult or impossible for parts of the year (e.g. Russia, Alaska).

3.2.1 Literature and satellite-based estimation

Our first method to generate global methane superemitter combines satellite data with published methane intensities.

We first gather methane plume data from TROPOMI and EMIT satellites (2022–2024) (*21*). From this dataset we identified 677 superemitters across six LNG exporters (Figure 10, Table 6). Russia had the highest number (264), followed by the United States (244) and Algeria (160). These three countries accounted for 99% of all detected superemitters.

Satellite observations did not detect superemitters in Indonesia, Malaysia, and Qatar. These countries produce LNG mainly from offshore fields, showing a limitation in satellite-based methane

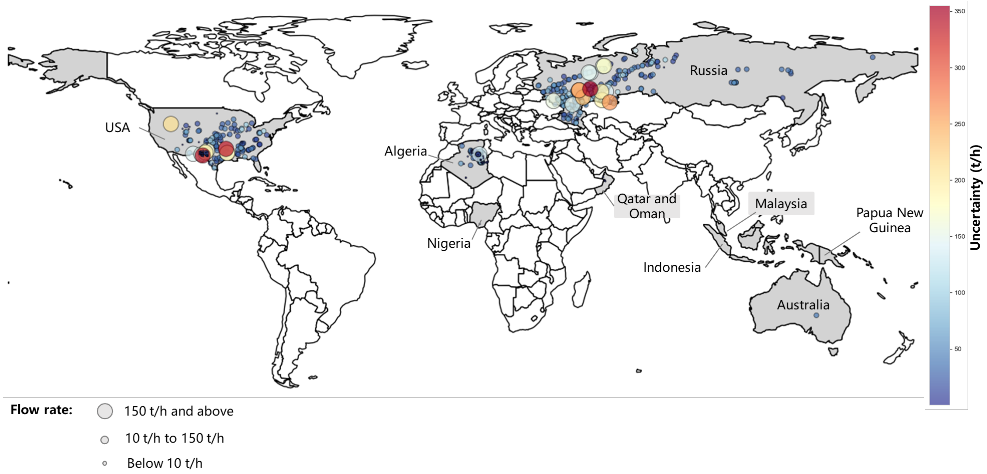

Figure 10: **Global distribution of superemitters in LNG exporters.** Circle sizes represent plume leak rates (tonnes/hour). Colors indicate measurement uncertainty (high uncertainty in red, low uncertainty in blue), defined as the difference between upper and lower leak rate bounds. The map shows 677 superemitters detected across six countries, with significant clustering in Russia, the United States, and Algeria.

Table 6: **Distribution of superemitters across LNG exporters.** Number of detected superemitters and their total emission rates by country.

Country	Super-Emitter Count	Total Rate (tonnes/hr)
Russia	264	14,518
United States	244	9,199
Algeria	160	4,585
Oman	7	13.4
Australia	1	45.8
Nigeria	1	2.25
Total	677	28,363

measurement over water surfaces. Water strongly absorbs the infrared wavelengths used for methane detection, making traditional satellite observations ineffective for offshore facilities (*22*). Additionally, satellite observations are limited by cloud cover and weather conditions, particularly in equatorial regions, northern areas, and mountainous terrains (*23*). Emerging ”glint mode” observations show promise for some offshore methane detection (*24*), but this technology was unavailable for this study.

Our data reveals that plume rates correlate strongly with measurement uncertainties (Figure 11). Data points cluster near the one-to-one line, indicating that larger plumes produce higher measurement uncertainties.

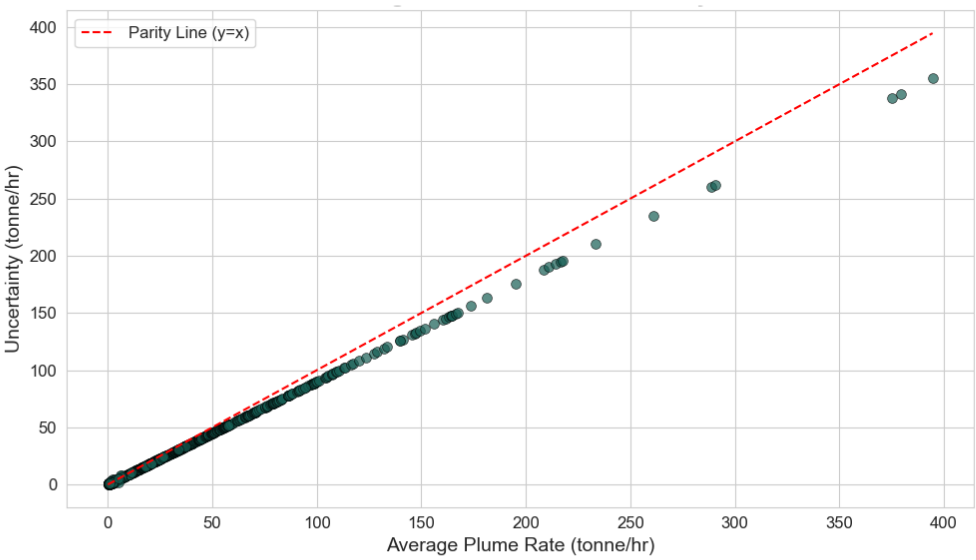

Figure 11: **Relationship between methane plume rates and measurement uncertainties.** Each point represents a detected superemitter, with the average plume rate (tonnes/hr) on the x-axis and measurement uncertainty (tonnes/hr) on the y-axis. The red dashed line indicates parity (y=x). The plot demonstrates increasing measurement uncertainty with larger plume sizes, particularly for emissions above 150 tonnes/hr.

To transform satellite observations into usable emissions data, we implemented a three-step process. First, we calculated average emission rates for locations with multiple plume detections using Equation 14:

$$\bar{E}_{x,y} = \frac{1}{n}\sum_{i=1}^{n} E_i, \quad \bar{L}_{x,y} = \frac{1}{n}\sum_{i=1}^{n} L_i, \quad \bar{H}_{x,y} = \frac{1}{n}\sum_{i=1}^{n} H_i \tag{14}$$

where n is the number of plume detections at that location, E_i represents individual emission measurements, and L_i and H_i represent the lower and upper uncertainty bounds, respectively.

Second, we addressed the 3.5 km satellite resolution limit for the TROPOMI instrument by combining plumes within this distance. We calculated distances using spherical geometry (Equation 15):

$$d = R_{earth} \arccos(\sin\phi_1 \sin\phi_2 + \cos\phi_1 \cos\phi_2 \cos(\Delta\lambda)) \tag{15}$$

where d is the distance between two points, R_{earth} is Earth's radius (6,371 km), ϕ represents latitude, and λ represents longitude in radians.

Third, we allocated processed methane emissions to oil and gas fields using a two-step geographical approach. For plumes with nearby fields (within 3.5 km), we divided the emission rate based on each field's gas production (Equation 16):

$$E_f = E_p \times \frac{Q_f}{\sum_i Q_i} \tag{16}$$

where E_f represents emissions allocated to field f, Q_f is that field's gas production rate, and $\sum_i Q_i$ represents total gas production within range.

For plumes without nearby fields, we distributed emissions across all fields in that country, weighted by production (Equation 17):

$$E_{f,c} = E_p \times \frac{Q_f}{\sum_j Q_{j,c}} \tag{17}$$

where $E_{f,c}$ is the allocated emission to field f in country c, and $\sum_j Q_{j,c}$ is total country gas production.

This allocation approach makes a key simplification regarding value chain segments. The satellite-detected plumes originate from the entire oil and gas sector—upstream (production fields), midstream (processing and transportation), and downstream (refineries and distribution) (*21*). However, our allocation method does not differentiate between these segments, as we often lack details on what kind of equipment and what value chain stage the superemitters occur in. This is especially true in regions with poor data availability. When plumes cannot be matched to nearby fields within the 10 km threshold, we allocate them to upstream production fields based on their relative production rates. This does not create double-counting issues as our methodology does not separately account for midstream and downstream methane emissions.

Table 7 shows emission rates for LNG fields by country after applying this allocation methodology. The United States, Algeria, and Russia dominate with 97% of allocated emissions. The distribution shifts compared to Table 6, with Russia's share decreasing from 51% to 24% and the United States' share increasing from 32% to 56%, reflecting differences in field coverage and production weighting.

A critical challenge in using satellite-detected superemitter data is that these observations

Table 7: **Allocated superemitter rates for LNG fields.** Total allocated emission rates by country after applying production-based distribution to detected superemitters.

Country	Total Rate (tonnes/hr)
United States	5,989
Algeria	3,232
Russia	1,434
Oman	9.12
Australia	39.2
Nigeria	1.73

represent instantaneous snapshots rather than continuous monitoring. To convert these instantaneous detections to annual averages, we determined how frequently these superemitters are active (their intermittency).

We first calculated country-specific intermittency factors using methane intensity (MI) measurements from recent studies. These studies can be categorized into two distinct methodological approaches. The first approach utilizes direct atmospheric observations to compute methane intensity at regional or country levels, using multiple measurement platforms including satellites, scientific aviation, and aerial surveys. Studies by Foulds, Maasakkers, Lu, and Chen fall into this category. The second approach relies on spatially-resolved greenhouse gas inventories based on reported activities and emissions factors, represented by Scarpelli and EDGAR v4.2. Table 8 presents country-level methane intensity values from these studies, with measurements grouped by their methodological approach.

For countries with significant superemitter detections (Algeria, Russia, and the United States), we selected the highest reported ML values to ensure conservative estimates. For other countries, we calculated the average of available ML values. To calculate country-specific intermittency factors, we used an iterative calibration approach. We initially assumed all superemitters were continuously active (intermittency factor = 1.0) and converted hourly emission rates to daily values. We then calculated annual field-level emissions and integrated them with non-superemitter emissions from the OPGEE model to derive field-level methane intensities, which we aggregated into country-level methane intensities.

We compared these modeled intensities with literature values and systematically adjusted the

Table 8: **Country-level methane intensity (MI) measurements from literature and values used in this study.** Comparison of MI values (gCH_4/MJ) across multiple studies (2021-2024), with the rightmost column showing the values used for calibrating our model. Studies are grouped by methodological approach: satellite-based measurements and inventory-based estimates.

Country	**Satellite-based measurements**				**Inventory-based**		**This Study**
	Foulds (*25*)	**Maasakkers (*26*)**	**Lu (*27*)**	**Chen (*28*)**	**Scarpelli (*29*)**	**EDGAR (*30*)**	
Algeria	–	0.027	0.147	0.022	0.175	0.326	**0.326**
Australia	0.069	–	–	–	–	–	**0.069**
Indonesia	–	–	–	–	0.180	–	**0.180**
Malaysia	–	0.303	–	–	0.203	0.278	**0.290**
Nigeria	–	0.444	0.041	–	0.515	0.709	**0.500**
Oman	–	–	–	0.901	0.199	–	**0.550**
Qatar	–	–	–	0.026	0.084	0.246	**0.096**
Russia	–	0.231	0.349	–	0.083	0.199	**0.349**
United States	–	0.228	0.280	–	0.115	0.180	**0.280**

intermittency factors until our modeled country-level methane intensities matched the target values. The resulting country-specific intermittency factors are presented in Table 9. For countries with predominantly offshore production or limited satellite coverage, matching literature-reported methane intensities solely by adjusting intermittency factors was not possible. In these cases, we quantified the difference as a "top-down gap" representing emissions detected in larger-scale atmospheric measurements but not captured by our satellite-based superemitter analysis.

Table 9: **Super-emitter intermittency factors by country.** Factors convert processed plume detections to annual averages, derived by calibrating OPGEE results to top-down measurements from Table 8.

Country	**Intermittency factor**
Nigeria	0.300
Australia	0.230
United States	0.162
Oman	0.150
Russia	0.065
Algeria	0.028

The variation in intermittency factors (0.028 to 0.30) reflects differences in emission patterns, detection capabilities, and infrastructure characteristics. Lower factors suggest more intermittent emissions or fewer detection opportunities, while higher factors indicate more persistent emission sources. After applying these intermittency factors, we obtained the annual average superemitter rates for LNG fields, as shown in Table 10.

We cannot discount in this analysis that superemitter data are highly entangled with geographic and/or meteorological characteristics as well as with actual superemitter frequency. For example, Russia has a number of these characteristics which make remote sensing challenging, including: (1) high latitude causing low sun angles and low solar availability over much of the year (2) cloudy conditions over much of the year, (3) significant amounts of standing water and/or lakes which reduce infrared reflection to satelite sensors, thus making observing more challenging. It is still an open problem in the literature about how to adjust for these factors when attempting to compute the actual MI from observations.

In general, estimates from regions with bright conditions, low cloud cover, and little water should be considered much more complete than regions with the opposite in each sense. This is particularly the case for countries with mostly offshore production, as noted above, as that precludes these measurements almost entirely.

Table 10: **Annual average superemitter rates for LNG fields.** Total emission rates by country after applying intermittency factors to convert from instantaneous detections to annual averages.

Country	**Total Average Rate (tonnes/day)**
United States	23,285
Russia	2,233
Algeria	2,190
Australia	216
Oman	32.8
Nigeria	12.4

Figures 12 and 13 illustrate the relative contributions of different emission sources across LNG exporters. Figure 12 shows the percentage breakdown of methane emissions by source type, revealing that some countries (Algeria, Russia, United States, and Australia) have emissions dominated by superemitters, while others (Indonesia, Malaysia, Qatar, Oman, Papua New Guinea, and Nigeria) show significant top-down gaps. Figure 13 presents ML values (g CO_2eq./MJ) by country, showing that Nigeria and Oman have the highest intensities, while Australia has the lowest.

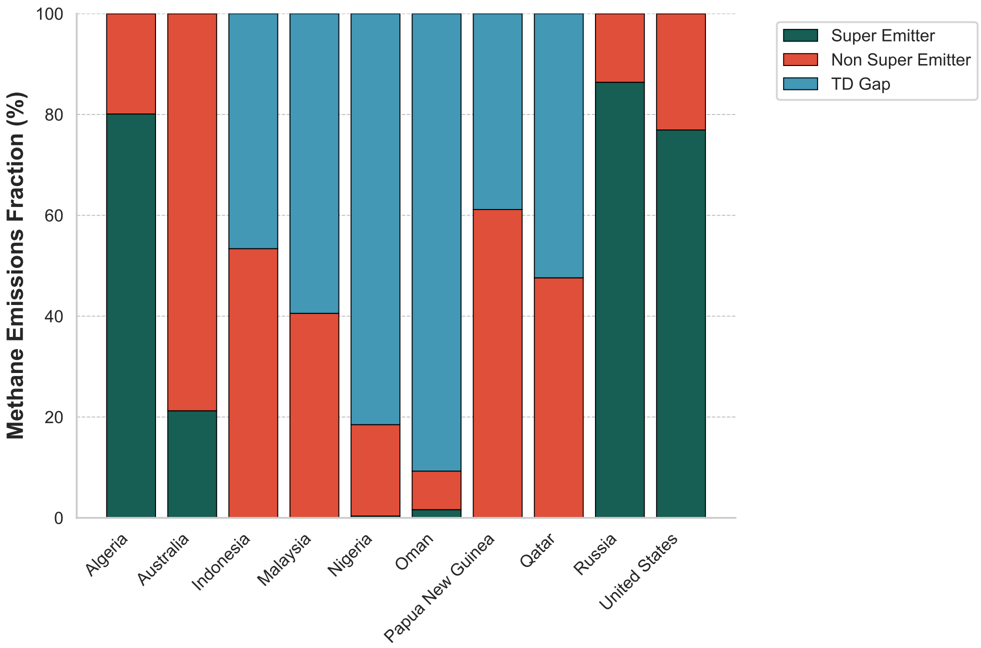

Figure 12: **Methane emissions breakdown by country and source type.** Stacked bars show the relative contributions of superemitters (green), non-superemitters (red), and top-down gap (blue) to total methane emissions for each LNG exporter. Countries show distinct patterns ranging from superemitter dominated (Algeria, Russia, US) to those with significant top-down gaps (Indonesia, Malaysia, Qatar).

3.2.2 US basin similarity based estimation

Given the challenge and importance of this issue, we also developed an alternative method for estimating the contribution of superemitters using established superemitter data from US basins. This approach leverages the relationship between non-superemitter and superemitter contributions in six major US gas production basins to estimate superemitter emissions for global LNG fields.

Our method uses non-superemitter to superemitter ratios from six US basins quantified by Sherwin et al. (*31*). The Sherwin et al. paper leverages the largest dataset of airplane measurements thus examined, including nearly one million overflights of oil and gas wells with remote sensing plume detection equipment. By combining a very large number of direct measurements with the Rutherford et al. model to estimate emissions below the detection limit of each airborne sensor, Sherwin et al. estimate a breakdown in each region between superemitter and non-superemitter emissions.

Table 11 presents these basin-specific ratios, where low and high bounds represent aerial site

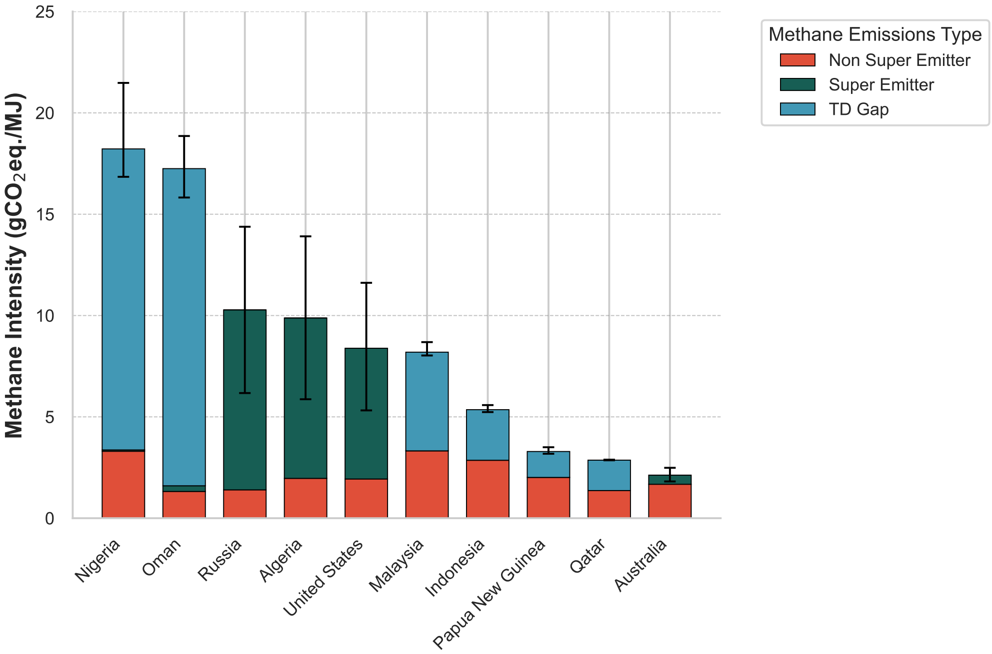

Figure 13: **Methane CI by country and source type.** Stacked bars show methane CI (g CO_2eq./MJ) contributions from superemitters (green), non-superemitters (red), and top-down gap (blue) for each LNG exporter. Error bars indicate uncertainty ranges. Nigeria and Oman show the highest methane intensities, while Australia demonstrates the lowest.

measurements from different campaigns within the same basin. As seen in the table, in some regions superemitters contribute as much as 75% of emissions, while in other places they contribute only 15%. For Pennsylvania, Uinta, and Fort Worth, identical low and high bounds indicate single-campaign measurements. We implemented a two-step process to associate global LNG fields with these US basins. First, we assigned US fields to basins based on geographic coordinates, defining polygon boundaries for each basin. This yielded 717 US fields distributed across the six basins (Table 12), with Pennsylvania and Permian basins containing the most fields.

For non-US fields and US fields outside these basins, we implemented a feature-based similarity classification using key production and geological parameters (OPGEE inputs): number of producers, oil production volume, gas-to-oil ratio, gas composition, reservoir conditions, API gravity, flaring-to-oil ratio, production methods (downhole pump and water reinjection), and product energy content. We standardized these parameters using Equation 18:

$$z_i = \frac{x_i - \mu}{\sigma} \tag{18}$$

Table 11: **Non-superemitter to superemitter ratios for US basins.** Ratio bounds from field measurements in six US basins, representing the proportion of non-superemitter to superemitter emissions.

Basin	Low Bound	High Bound
Permian	0.238	0.472
San Joaquin	0.362	0.639
Denver-Julesburg	0.845	0.851
Pennsylvania	0.233	0.233
Uinta	0.661	0.661
Fort Worth	0.388	0.388

Table 12: **Distribution of US fields across basins.** Geographic assignment of US fields to production basins based on coordinate boundaries.

Basin	Field Count
Pennsylvania	359
Permian	284
Uinta	26
Fort Worth	25
Denver-Julesburg	15
San Joaquin	8

where z_i is the standardized value, x_i is the original value, and μ and σ are the mean and standard deviation of the feature across all fields.

We then calculated Euclidean distances between each non-US field and all US fields in this standardized feature space using Equation 19:

$$d(f_1, f_2) = \sqrt{\sum_{i=1}^{n} (z_{1i} - z_{2i})^2} \tag{19}$$

where $d(f_1, f_2)$ represents the similarity distance between fields, x_{1i} and x_{2i} are the values of feature i for fields f_1 and f_2 respectively, σ_i is the standard deviation of feature i, and n is the total number of features considered.

Statistical analysis of similarity distances reveals significant differences between countries (one-way ANOVA: F(9,2444) = 128.68, p < 0.0001), as illustrated in Figure 14. Algeria and Indonesia show the highest mean similarity distances (554.9 and 537.3, respectively), indicating their fields are least similar to US basins. In contrast, Australia (54.3) demonstrates relatively strong similarity to US fields despite its geographic remoteness. This pattern suggests that geological and operational characteristics drive field similarity rather than geographic proximity. Countries represented by only a few fields, such as Indonesia (N = 13) and Papua New Guinea (N = 4), show wider 95% confidence intervals, sometimes extending below zero. The negative lower bounds arise from the symmetric, normal-based CI calculation and simply highlight greater statistical uncertainty.

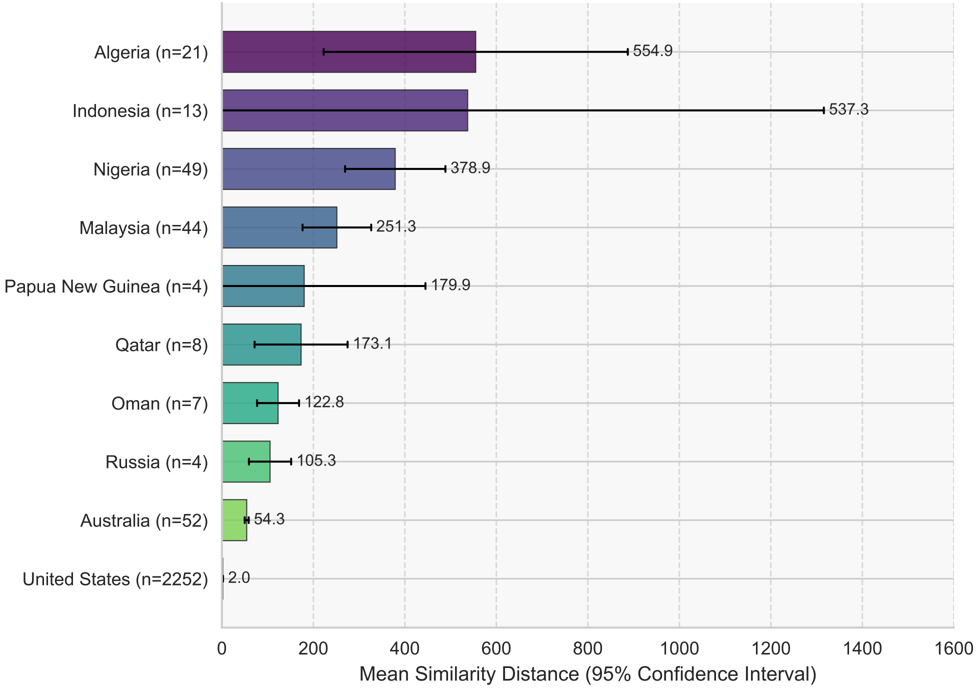

Figure 14: **Mean similarity distances between non-US LNG fields and their closest US field matches.** Horizontal bars show mean Euclidean distances in standardized feature space with 95% confidence intervals shown as error bars. Lower values indicate greater similarity to the six US basins. Countries are ordered by decreasing similarity distance, with Algeria showing the greatest dissimilarity and the US fields showing minimal distances. The number of fields analyzed for each country is indicated in parentheses (n).

For each non-US field, we identified its nearest labeled US field and assigned the corresponding basin non-superemitter to superemitter ratio. Once all global fields were labeled to US basins, we estimated superemitter emissions using Equation 20:

$$E_{\text{super}} = \frac{E_{\text{non-super}}}{r_{\text{basin}}} \tag{20}$$

where E_{super} is the estimated superemitter emissions rate, $E_{\text{non-super}}$ is the small source (non-superemitter rate) from the statistical model embedded in OPGEE as described above, and r_{basin} is the non-superemitter to superemitter ratio for the assigned basin as shown in Table 11.

By applying both low and high ratio values from Table 11, we generated uncertainty ranges for superemitter estimates.

This method has advantages in that it leverages an enormous compendium of airplane data, and these airplanes are able to see below the superemitter threshold, as shown in controlled tests (*32*). However, there are some challenges with this approach. First, by assigning alignment to US fields via similarity scores, we are inherently projecting US superemitter frequencies to other regions. This may or may not be true: in some countries fields with similarities to a given US field may have lower emissions than the US field, while in some countries they may have higher emissions. Without more measurements in other countries, it is difficult to know the balance of this effect. More measurement and comparison across regions is required.

3.2.3 Neural network-based superemitter estimation

To address the limitations of the basin similarity approach, we developed a machine learning solution using a multilayer perceptron (MLP). This methodology leverages the complete US field dataset (OPGEE inputs same as Section 3.2.2), containing both non-superemitter emissions (from OPGEE) and superemitter emissions (from literature and satellite approach), to directly predict superemitter emissions for non-US fields with hopefully greater accuracy. We selected US fields specifically because they represent the largest available dataset without significant top-down gaps in emissions accounting.

Our approach used 2,252 US fields with OPGEE inputs, non-superemitter emissions, and superemitter emissions as training data. After removing extreme outliers beyond the 99.9th percentile (superemitter values exceeding 26,259 tonne/day), we retained 2,249 fields for model training. The neural network architecture incorporated several feature engineering techniques to improve performance. First, we standardized all numeric features using robust scaling to minimize the influence of outliers. Second, we applied power transformations (Yeo-Johnson method) to normalize feature distributions. For highly skewed features (skewness > 1), we created additional log-transformed versions, which significantly improved model performance for fields with large emissions. We also engineered interaction features, particularly between non-superemitter intensities and production characteristics.

Table 13 displays our optimized neural network architecture, which consists of an input layer accepting 38 engineered features, followed by three hidden layers with decreasing neuron counts (128, 64, and 32). Each hidden layer incorporates LeakyReLU activation functions (with $\alpha = 0.1$), batch normalization, and dropout regularization (rate = 0.3) to prevent overfitting. The output layer uses a linear activation function to predict superemitter emissions.

Table 13: **Neural network architecture for superemitter prediction.** Optimized multilayer perceptron architecture with regularization techniques for superemitter methane CI prediction.

Layer	Output Shape	Parameters	Activation
Input	(38)	0	-
Dense	(128)	4,992	LeakyReLU
BatchNormalization	(128)	512	-
Dropout (0.3)	(128)	0	-
Dense	(64)	8,256	LeakyReLU
BatchNormalization	(64)	256	-
Dropout (0.3)	(64)	0	-
Dense	(32)	2,080	LeakyReLU
BatchNormalization	(32)	128	-
Dropout (0.3)	(32)	0	-
Dense (Output)	(1)	33	Linear

Total Parameters: 16,257 (Trainable: 15,809, Non-trainable: 448)

We implemented a custom weighted loss function that places higher emphasis on accurately predicting large emission values. Standard mean squared error (MSE) tends to underestimate large values, which are particularly important in superemitter contexts. Statistical analysis of superemitter distributions revealed that a small number of ”super-superemitters” (fields in the highest quartile) account for a disproportionately large fraction of total emissions. The custom loss function, defined in Equation 21, applied progressively greater weights to larger target values:

$$\mathcal{L}_{\text{weighted}} = \frac{1}{n}\sum_{i=1}^{n}(y_i - \hat{y}_i)^2 \cdot (1 + |y_i|) \tag{21}$$

where y_i represents the true superemitter value, $\hat{y}_i$ is the predicted value, and $(1 + |y_i|)$ applies greater weight to larger values.

Additionally, we implemented sample weighting during training, applying a factor of 5.0 to samples exceeding the 75th percentile threshold (105.26 tonne/day), thereby ensuring the model adequately learned from the critical high-emission cases. Model training used an Adam optimizer with an initial learning rate of 5×10^{-4}, which was dynamically reduced when validation performance plateaued. We applied early stopping with a patience of 25 epochs to prevent overfitting, and all performance metrics were evaluated on a held-out test set comprising 20% of the data. Figure 15 illustrates the training process, showing the evolution of loss and mean absolute error for both training and validation sets over 180 epochs, along with the adaptive learning rate schedule.

The model achieved an overall coefficient of determination (R^2) of 0.829 on the test set, with a mean absolute error (MAE) of 81.7 tonne/day. Performance analysis by emission ranges revealed that prediction accuracy varied significantly across the value spectrum, as illustrated in Figure 16. For standard superemitter intensities (below 105.26 tonne/day), the model demonstrated excellent accuracy ($R^2 = 0.610$, MAE = 6.127, RMSE = 15.382). For high values exceeding the 75th percentile threshold ($>$105.26 tonne/day), performance remained robust ($R^2 = 0.804$, MAE = 318.230, RMSE = 805.787), indicating the model effectively captured the extreme emission events that contribute disproportionately to total emissions. As can be seen in the parity charts, at the highest emissions rate, our model tends to under-predict emissions (orange dots at RHS of figure 16B. Thus, it is more probable that our model underestimates the largest sources, rather than overestimates them.

This stratified performance analysis approach provides critical insight into model reliability across the emissions spectrum, particularly highlighting the effectiveness of our custom weighted loss function (Equation 21) in capturing the high-value superemitters that dominate total methane emissions.

We developed an uncertainty estimation framework to account for variability in superemitter measurements. Rather than relying on a single model prediction, we trained three separate neural networks using identical architecture (Table 13) and OPGEE input features, but with different target values representing the uncertainty bounds in US field measurements. Specifically, we trained a low-bound model using the minimum superemitter values reported for US fields, an average model using mean values, and a high-bound model using maximum reported values. Each model maintained the same non-superemitter emissions values while varying only the superemitter targets. We generated three estimates per field when applying these models to predict superemitter emissions for global LNG fields, creating a complete uncertainty envelope around our predictions. Because each model was trained independently to optimize different target distributions, the predicted values

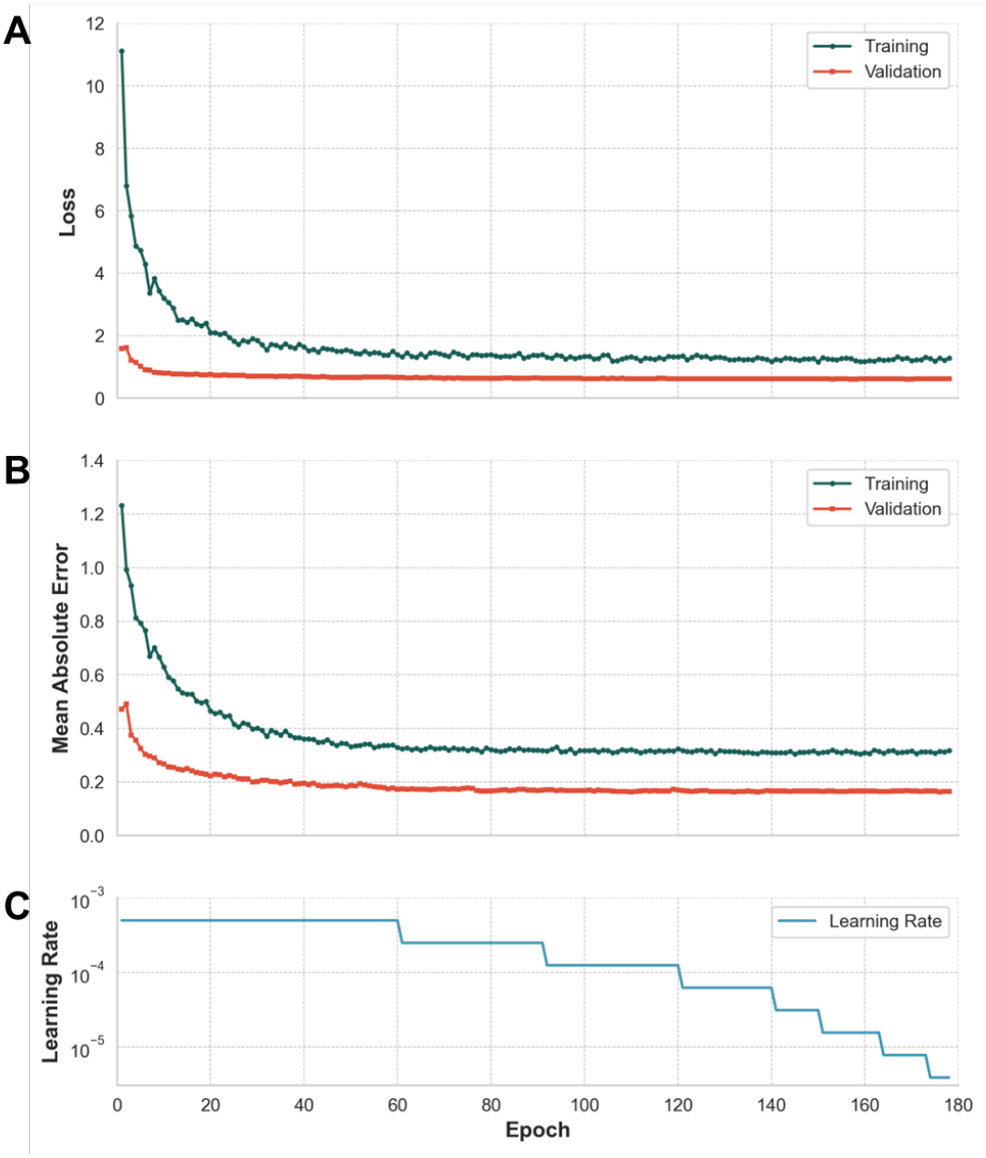

Figure 15: **Neural network training metrics over 180 epochs.** (**A**) Custom weighted loss function values for training (green) and validation (red) datasets, showing rapid initial convergence followed by gradual refinement. (**B**) Mean absolute error for training and validation sets, demonstrating consistent improvement throughout training while maintaining a healthy gap between training and validation performance. (**C**) Adaptive learning rate schedule showing strategic reduction from 5×10^{-4} to 4×10^{-6} in response to validation performance plateaus, enabling increasingly fine-grained parameter optimization.

occasionally did not preserve the expected ordering (low ≤ average ≤ high). In such cases, we sorted the predictions in ascending order to establish consistent uncertainty bounds.

The neural network approach has several advantages over the similarity-based method described in Section 3.2.2. First, it can directly learn complex, non-linear relationships between field charac-

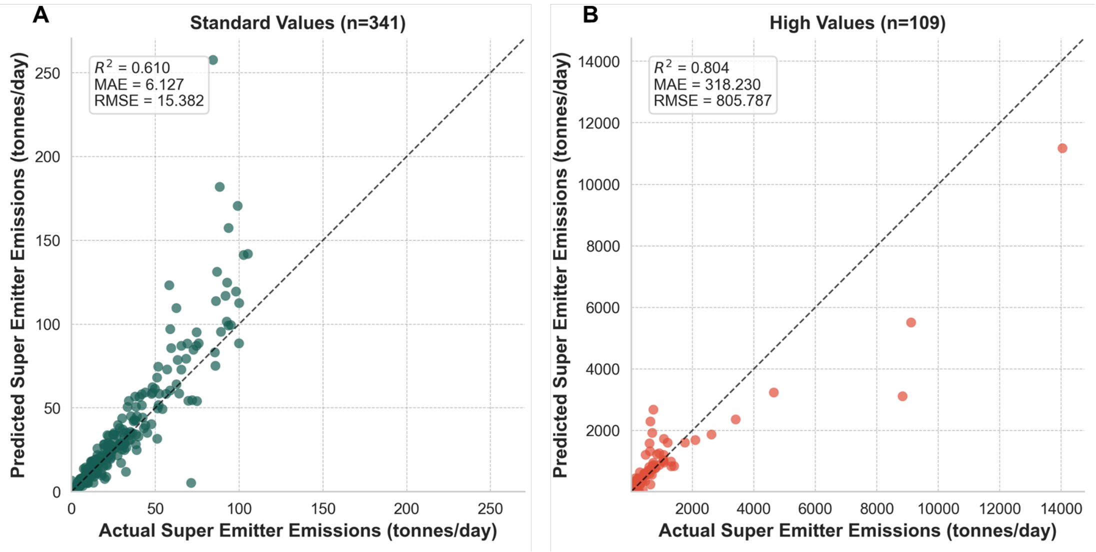

Figure 16: **Neural network prediction performance across emission ranges.** (**A**) Parity plot for standard superemitter values (n=341, <105.26 tonne/day), showing strong correlation between predicted and actual emissions with R^2 = 0.610, MAE = 6.127, and RMSE = 15.382. The dashed line represents perfect prediction. (**B**) Parity plot for high superemitter values (n=109, ≥105.26 tonne/day), demonstrating robust performance (R^2 = 0.804, MAE = 318.230, RMSE = 805.787) despite the challenging nature of predicting extreme emission events. Note the different scales between panels, with high values reaching over 14,000 tonnes/day compared to 250 tonnes/day for standard values.

teristics and superemitter patterns, rather than relying on simple distance metrics in feature space. Second, it leverages the complete dataset, incorporating information from all US fields simultaneously rather than just the nearest match. Third, through our custom loss function and sample weighting, it specifically optimizes for the accurate prediction of large values of superemitter emissions that dominate total methane emissions.

While the model's complexity makes interpretation less straightforward than the similarity approach, potentially reducing transparency for some stakeholders, the neural network methodology is well-suited to future improvements as additional data becomes available. The global supply of satellite-based methane observations is set to grow rapidly. MethaneSAT already provides open regional flux maps at 100–500 m resolution (*33*), and CarbonMapper's Tanager-1 spacecraft, launched in August 2024, now publishes hundreds of facility-scale plume detections each month (*34*). GHGSat plans to launch nine additional satellites by 2026, nearly doubling its constellation and enabling weekly revisits of major production basins (*35*). As these observations accumulate, researchers can integrate the direct measurements to refine the model, boost predictive accuracy, and reduce uncertainty. The model's architecture is adaptable to assimilating new measurement data, enabling continuous improvement as methane-measurement technologies advance.

3.3 Integrated multi-method approach for methane emissions estimation

To leverage the complementary strengths of our three estimation approaches (literature-satellite, US basin similarity, and neural network), we developed an integrated sampling methodology that combines their outputs into a unified superemitter estimate for each field. This approach maximizes the information value of each approach while mitigating their limitations, providing more robust estimates.

The integration framework applies uniform field-level sampling across the three approaches (referred to as "Literature & Satellite," "US Similarity," and "NN"). For each LNG field in our dataset, we extract the low, average, and high superemitter estimates from each approach, ensuring that uncertainty bounds are preserved throughout the integration process. The sampling procedure follows a field-centric approach, treating each production field as an independent sampling unit to maintain geographical coherence in the resulting estimates.

For fields with results available from all three approaches, we implement a balanced sampling where each approach contributes equally to the integrated estimate. This is formalized as Equation 22:

$$S_{f,c} = \{s_{f,m,c} | m \in M_f\} \tag{22}$$

where $S_{f,c}$ represents the set of samples for field f at confidence level c (low, average, or high), $s_{f,m,c}$ is the estimate from approach m for field f at confidence level c, and M_f is the set of applicable approaches for field f.

For special cases where certain approaches are inapplicable or less reliable, we implement adaptations to the general framework. In particular, for fields in Papua New Guinea, we exclude the literature-satellite approach due to no literature reporting ML. It only uses the neural network and basin similarity approaches as shown in Equation 23:

$$M_f = \begin{cases} \{\text{NN, US Similarity}\}, & \text{if field } f \text{ is in Papua New Guinea} \\ \{\text{Literature \& Satellite, NN, US Similarity}\}, & \text{otherwise} \end{cases} \tag{23}$$

The minimum available sample size across applicable approaches determines the number of

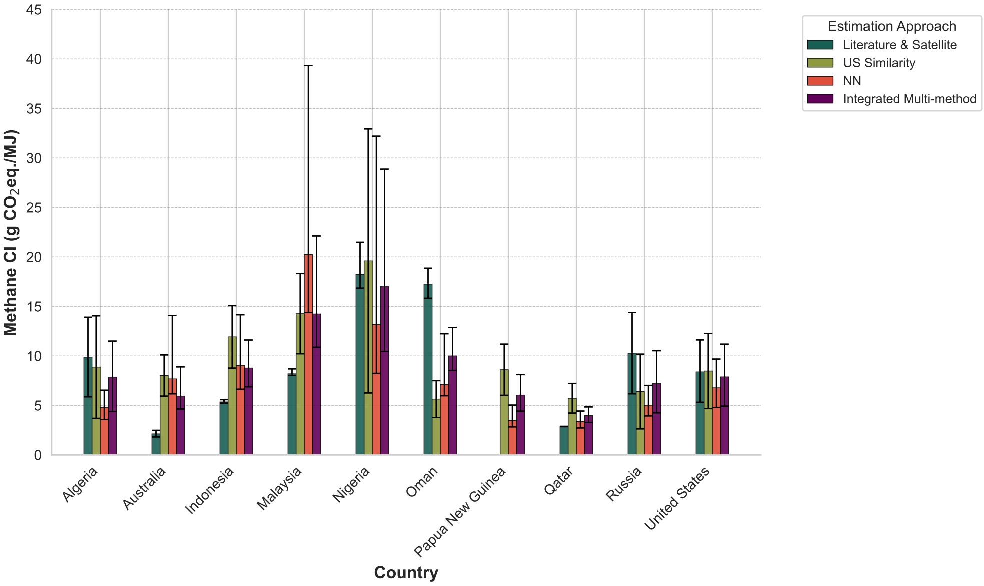

Figure 17: **Comparison of methane carbon intensity estimates by country across different approaches.** Bar chart showing methane CI values (g CO_2eq./MJ) for major LNG exporters using four estimation methods. The three individual approaches (Literature & Satellite, US Similarity, and NN) demonstrate varying estimates, with the Integrated Multi-method approach (purple) providing a balanced composite estimate. Error bars represent uncertainty ranges. Nigeria, Malaysia, and Indonesia show the highest methane intensities, while Qatar demonstrates the lowest values across all approaches.

samples drawn from each approach, ensuring balanced representation. Since our field-level dataset contains one estimate per approach for each field, this typically results in one sample per approach in the final integration. Once samples are collected for all fields across all confidence levels, we organize them into separate datasets corresponding to the low, average, and high confidence bounds.

The comparison of methane emissions across countries reveals significant heterogeneity in methane emissions profiles between different geographical regions. Nigeria, Malaysia, and Indonesia demonstrate higher methane intensities with wider uncertainty ranges, while Qatar consistently shows the lowest intensities. The integrated multi-method approach successfully captures this international variability while providing more balanced estimates than any single approach alone.

4 Midstream

The midstream links natural gas production to liquefaction facilities, as shown in Figure 1. This link requires tracking gas flows from production fields through processing plants to liquefaction terminals. Gas traceability differs between US and non-US operations. In the United States, current datasets lack direct connections between fields, processing plants, and liquefaction terminals. We optimize gas movements through the pipeline network instead. This method maps regional gas flows rather than specific field-to-facility pathways. For operations outside the United States, we have detailed connection data. These datasets show specific pathways from production fields to processing plants and liquefaction terminals. Each major facility has documented links to its source fields. This detailed tracking maps precise gas movement patterns through the value chain, identifying which fields supply gas to specific processing plants and terminals.

4.1 Transmission schemes

Natural gas transmission has two main components: functional infrastructures and transportation infrastructures. Functional infrastructures consist of fields, processing plants, and liquefaction plants at export ports. Transportation infrastructures include pipeline networks. To analyze natural gas transportation costs within a region using pipeline systems, we construct a weighted graph $G = (N, E, W)$ to determine optimal transportation schemes between infrastructures.

In this graph representation, N represents the set of all nodes (including inner and crossing nodes) belonging to each pipeline. E represents the set of pipelines connecting two nodes in N. W represents the weight of the corresponding edge in the network, defined as the distance (or length) of each pipeline. The Haversine formula is widely used in practical applications due to its stability and accuracy in computations involving extreme conditions (*36*). We calculate the length L_{ij} of a pipeline e_{ij} using Equation 24:

$$\begin{cases} a = \sin^2\left(\frac{\Delta\text{lat}}{2}\right) + \cos(\text{lat}_i)\cdot\cos(\text{lat}_j)\cdot\sin^2\left(\frac{\Delta\text{lon}}{2}\right) \\ c = 2\cdot\text{atan2}\left(\sqrt{a}, \sqrt{1-a}\right) \\ L_{ij} = R_{\text{Earth}}\cdot c \end{cases} \tag{24}$$

where Δlat and Δlon represent the differences in latitude and longitude between nodes n_i and n_j, respectively, and R_{Earth} is the radius of the Earth (set to 6371 km here).

The infrastructure must be integrated into the pipeline network to evaluate the natural gas transportation distance between two infrastructure elements through pipelines. For processing plants and liquefaction plants, we calculate the geographical distance between each infrastructure and all nodes within the network through Equation 24. Then, we virtually assign the infrastructure to the nearest node. This integration process ensures that all facilities are properly connected to the pipeline network for accurate distance calculations.

The total production of fields exceeds the total processing capacity of processing plants, since gas is processed locally in some fields. Therefore, we employ a strategic methodology to ensure that gas fields are selected based on their proximity and production capacity relative to the processing capabilities before the fields' integration. We first calculate the distance from each field to the nearest node in the pipeline network, and sort these distances in ascending order to prioritize fields based on proximity. Starting with the nearest field, we calculate the cumulative production capacity until it matches or exceeds the total processing capacity of the plants. This step helps identify which fields are feasible to connect to the existing processing infrastructure without exceeding its capacity. We identify the critical distance—the maximum distance at which the cumulative production capacity matches the processing plants' total capacity. In this scenario, the critical distance was determined to be 20 miles. We select fields that fall within the critical distance for pipeline connection, ensuring that the fields selected are those that can effectively feed into the processing plants without overburdening the system.

Using the US as a reference, the total number of fields considered viable for integration decreased from 3767 to 3599. This reduction aligned the total production capacity from 135.81 billion cubic feet per day (bcfd) to 123.32 bcfd, which closely matches the processing capacity of 122.38 bcfd, with a minimal error margin of 0.77%. We integrate the selected fields into the pipeline network using the same method as processing plants and liquefaction plants. This systematic approach ensures optimal field selection based on both geographical proximity and capacity constraints.

To determine or optimize the operations (flow rate) within different facilities, we evaluate the distance between two specific facilities. Understanding that shorter distances generally correlate with lower transportation costs and reduced carbon emissions, operators are likely to minimize transportation distance. Thus, we select the shortest path within the pipeline network as the metric for determining the distance between two facilities. This approach reflects real-world operational preferences and helps validate our model against actual industry practices.

Since every facility is integrated onto a node in the pipeline network, we employ Dijkstra's algorithm to calculate the shortest path between two facilities (*37*). We initialize all nodes with an infinite distance and set the starting point's distance to zero. For the active node, we consider all its unvisited neighbors and calculate their tentative distances through the node. We compare the newly calculated tentative distance to the current assigned value and assign the smaller one. Once we have considered all unvisited neighbors of the current node, we mark the current node as visited. A visited node will not be checked again. We continue with the node possessing the smallest tentative distance, repeating the process. The process completes when all nodes have been visited, and the algorithm has found the shortest path from the starting node to all other nodes.

Finally, we store three shortest path datasets (from every field to every processing plant, from every processing plant to every liquefaction plant, and from every field to every liquefaction plant) in a dictionary as the transportation cost between two specific facilities. These datasets serve as the foundation for optimizing gas flow allocation throughout the supply chain. The comprehensive nature of these calculations allows for detailed emissions tracking and cost optimization across the entire midstream infrastructure. By maintaining these interconnected datasets, we can analyze multiple routing scenarios and their environmental impacts efficiently.

4.2 Transmission problem

Natural gas pipeline transportation involves complex logistics due to varying demand, supply constraints, and operational costs. Linear programming has a structured approach to tackle these challenges by providing a framework for optimizing pipeline flows while minimizing costs. The linear programming model for natural gas transportation is formulated in this part.

4.2.1 Objective function

The total cost of NG transportation including economic and environmental aspects. The economical part includes costs for supplying natural gas, operating costs of the chain facilities, and operating costs of transmission, among others. The environmental part includes GHG emissions, electricity consumption, gas consumption, water consumption, and wastewater generation, among others. All these factors are related to the NG capacity (MMcfd) and the transportation distance (miles). Since the capacity allocations are optimized within an existing system, and the production capacities of fields, the processed capacities of processing plants, and the exportation capacities of liquefaction plants are already known, transportation costs are directly proportional to the aggregate distance per unit flow of natural gas transported (MMcfd · miles). Therefore, the objective is to minimize the total transportation cost:

$$\min Z = \sum_{i,j} c_{ij} x_{ij}$$

where c_{ij} represents the cost of transporting gas from source i to destination j, it is the length of the shortest path from node i to node j in the pipeline network; and x_{ij} is the capacity of gas transported from source i to destination j which is the decision variable need to be optimized.

4.2.2 Constraints

The model is subject to the following constraints:

- Supply constraint at each source:

  $$\sum_{j} x_{ij} \leq s_i \quad \forall i$$

  where s_i is the supply available at source i.

- Demand fulfillment at each destination:

  $$\sum_i x_{ij} \geq d_j \quad \forall j$$

  where d_j is the demand at destination j.

- Non-negativity constraint:

  $$x_{ij} \geq 0 \quad \forall i, j$$

The linear programming problem is solved using the simplex method, which iteratively moves toward the optimal solution by improving the objective function at each step.

4.3 Case study

Classification of export terminals represents a critical preprocessing step in the optimization framework. The analysis encompasses 33 export ports globally, which undergo classification based on two fundamental criteria before determining LNG source pathways. The first criterion evaluates whether the source fields for each port are known, as this information directly influences the capacity to trace gas origins and establish reliable supply chains. The second criterion assesses whether the source gas undergoes processing at dedicated processing plants, which affects both the quality specifications and operational constraints of the transported gas. This classification system enables systematic analysis of port characteristics and ensures appropriate handling of different terminal types within the optimization model.

4.3.1 Case 1: USA

For the export ports in the US, since the source fields are unknown, we assume the natural gas transmission pathway is from the field to the processing plant (total capacity of the produced gas should be processed) and then to liquefaction plants (the proportion for exportation should be liquefied).

The first step is to deal with the original data of the US. Since the 7 liquefaction plants are all located in the continental US, the fields and processing plants in Alaska are eliminated from the dataset. Afterward, the total fields are reduced from 3767 to 3739, and the total production capacity is reduced from 135.81 bcfd to 125.46 bcfd. The total processing plants are reduced from 897 to 893, and the total processing capacity is reduced from 130.14 bcfd to 122.38 bcfd. Then, capacity balance is handled according to 4.1. 20 miles are selected to be the critical distance and 3599 fields are integrated into the pipeline graph finally. The final production capacity for subsequent processing and liquefaction is 123.32 bcfd.

The second step is to establish the two shortest path datasets from fields to processing plants and from processing plants to liquefaction plants according to 4.1. Each item of the dataset represents the shortest pathway information from the start node and the end node, including the facilities integrated into the start node and end node, the capacities of the start node (supply) and end node (demand), and the total length of the connected pipelines.

The third step is to find the optimal pathways for transporting all the gas produced in fields to processing plants to process according to 4.2. The results are shown in Figure 18. There are 2828 pathways with a total cost of 34 901.02 bcfd · mile and a total processing amount of 114.43 bcfd. The difference is assumed to be processed locally caused by disconnection within the pipeline network.

This shortest path methodology is meant to approximate physical flow modeling: physical flows will follow paths of least resistance to ensure that supply equals demand at the LNG nodes. Distance is a reasonable proxy for least resistance (of course, other factors like pipeline size and control valves can affect the actual path taken by gas molecules). Note that this modeling does not take a contractual or monetary approach. We do not, for example, find which upstream producers are contracted to supply to LNG producers.

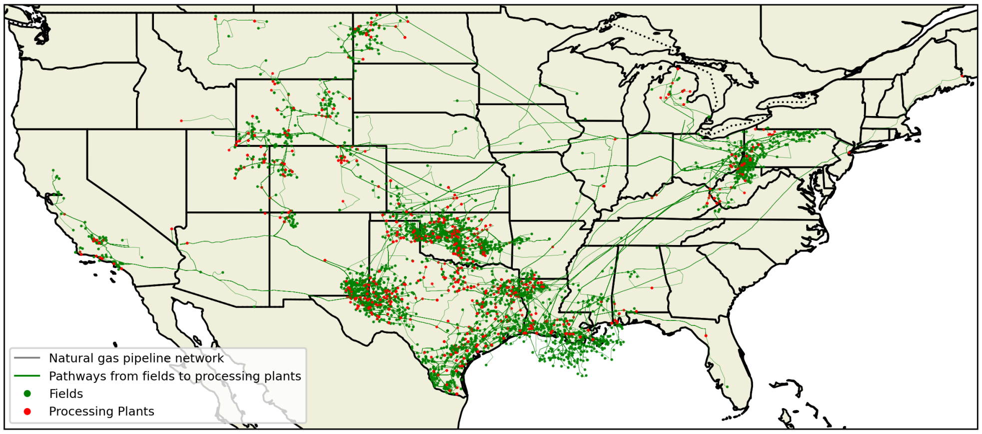

Figure 18: **Natural gas pipeline network from field to processing plant in the United States.** Map showing the geographical distribution of gas fields and their connections to processing plants through the pipeline network.

Before applying this method to identify optimal pathways from processing plants to liquefaction facilities, it is necessary to determine what fraction of processed gas is allocated for LNG export. The total U.S. LNG export capacity is 9.82 bcfd, accounting for 8.6% of the nation's processed capacity. However, since not all gas processing plants supply LNG, we tested proportions ranging from 10% to 40%, assuming the supplying plants allocate the same fraction of their output to LNG. Our results indicate that a 15% allocation aligns with reported flows from seven major export terminals. In total, 322 pathways were identified, with a combined transportation cost of 3971.11 bcfd · mile. Figures 19 through 25 illustrate the resulting natural gas pathways from fields to processing plants and onward to each liquefaction facility.

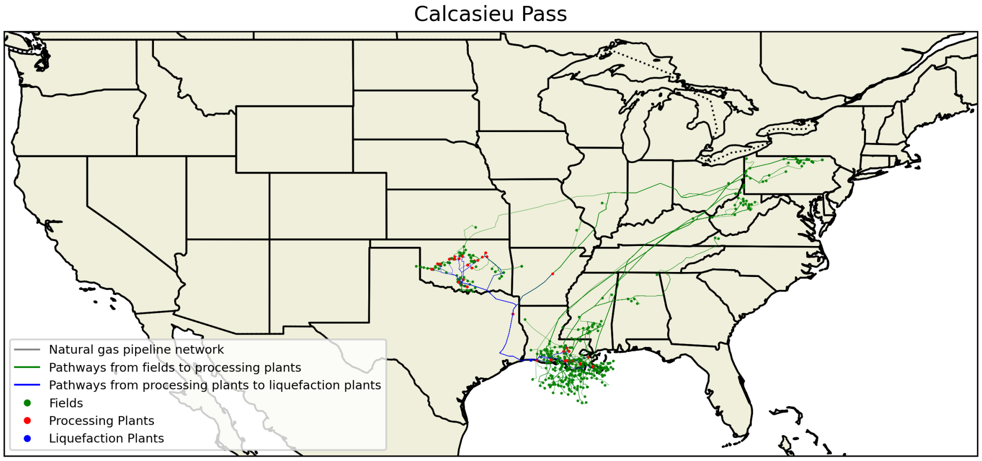

Figure 19: **Calcasieu Pass**

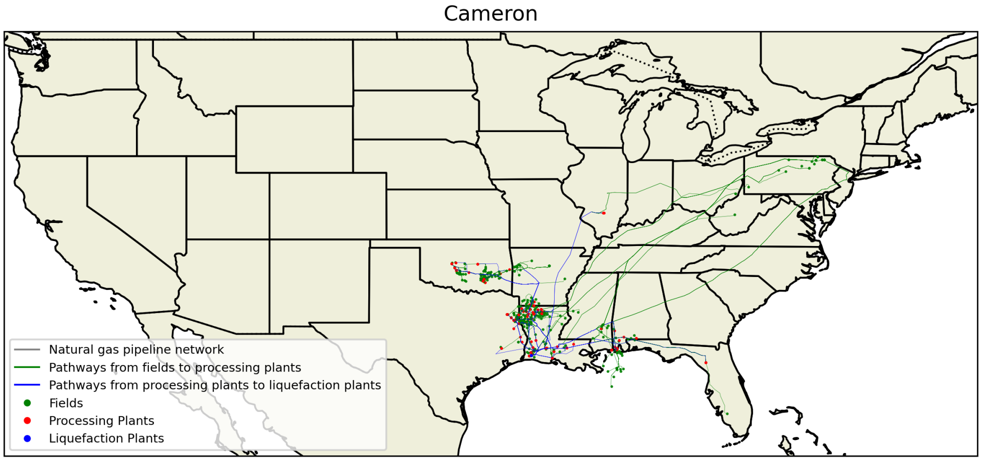

Figure 20: **Cameron**

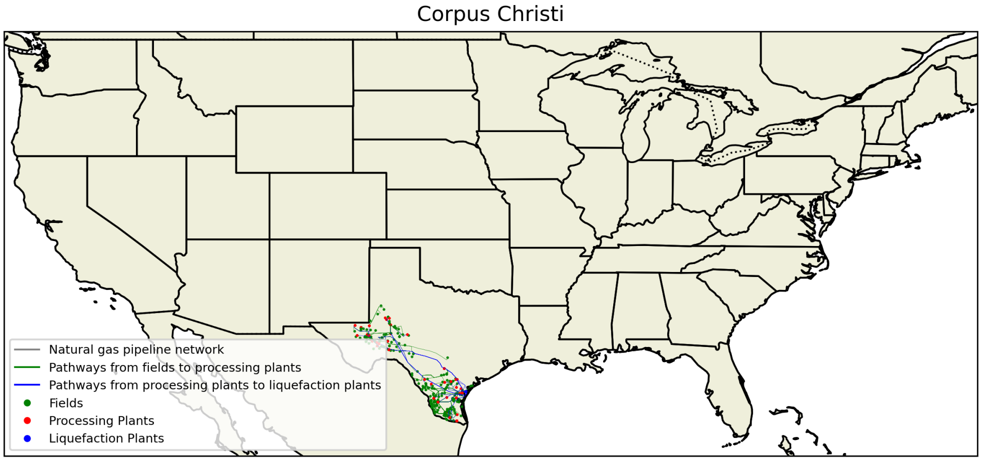

Figure 21: **Corpus Christi**

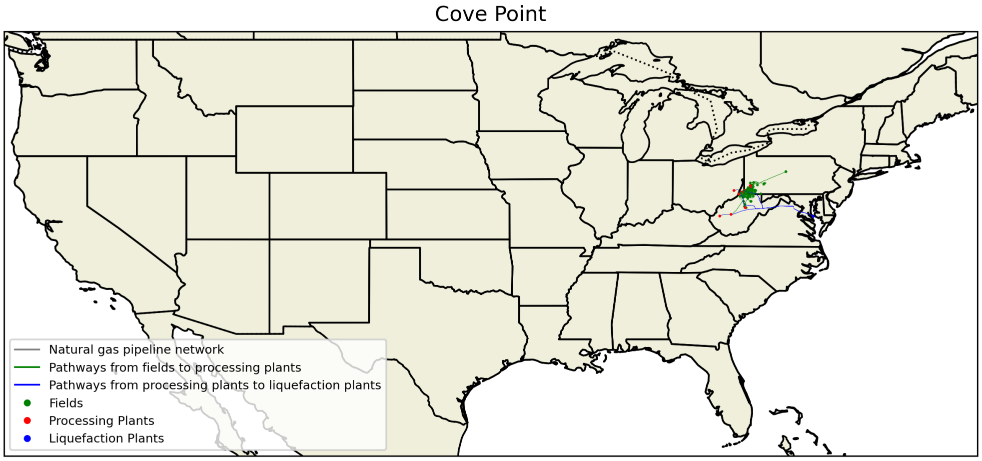

Figure 22: **Cove Point**

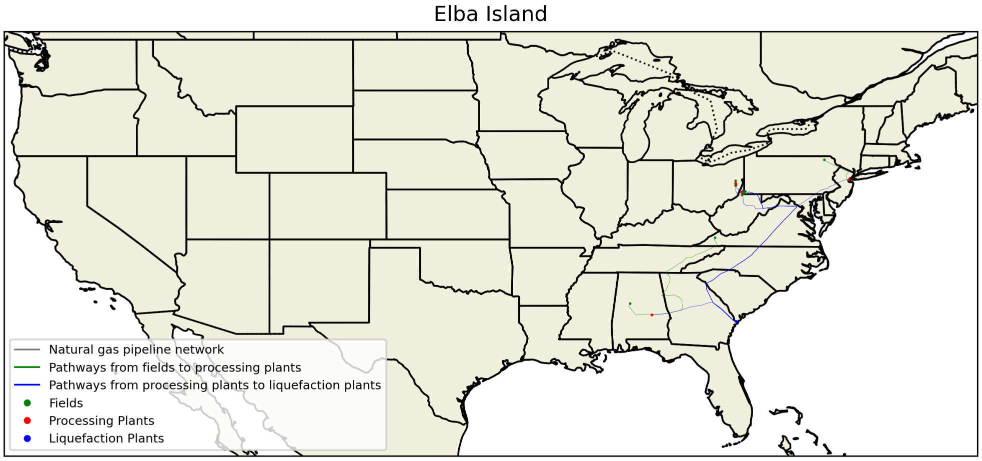

Figure 23: **Elba Island**

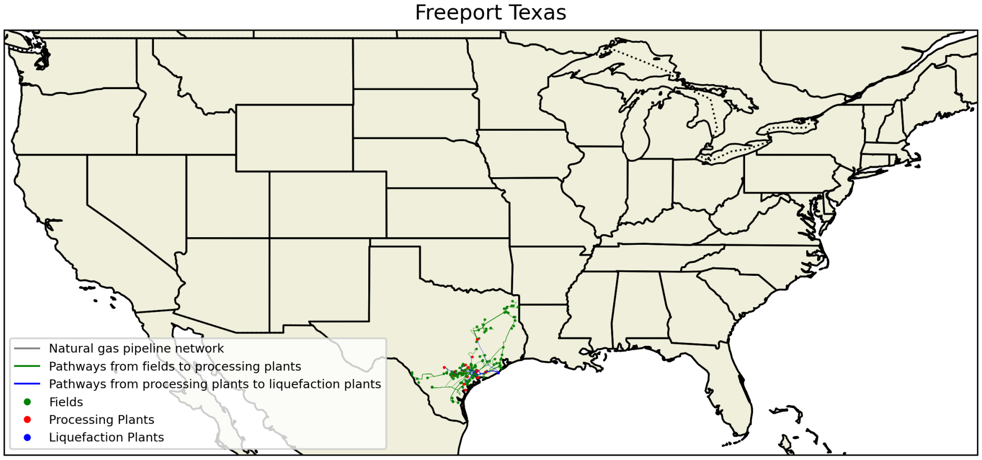

Figure 24: **Freeport Texas**

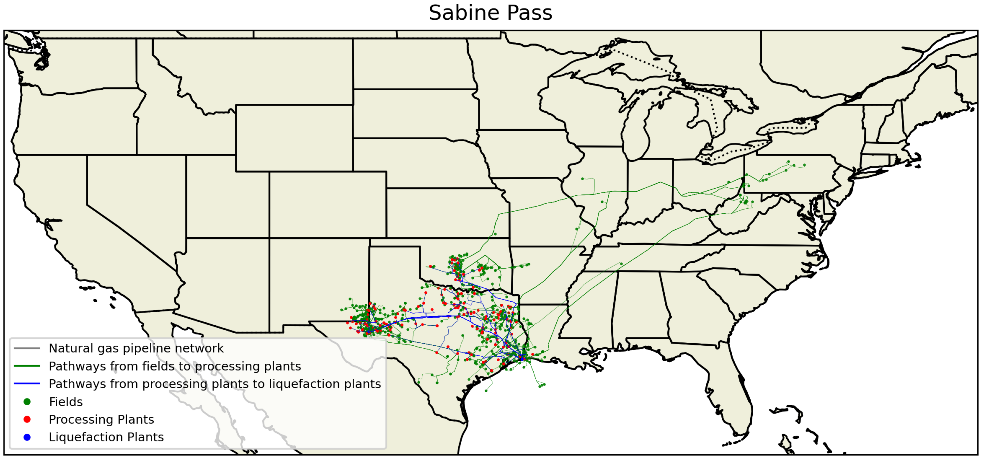

Figure 25: **Sabine Pass**

4.3.2 Case 2: Global

In this case, we examine the other 26 export ports in the top 10 LNG exporters, excluding the United States (see Table 14). The dataset specifies which gas fields supply each liquefaction plant. Prior to mapping LNG pathways, these liquefaction plants are categorized as either Type A or Type B based on whether or not the gas is processed at a dedicated processing plant. The criteria for each type are defined below:

- **Type A**: For a given export port, if the connected area (including gas fields and processing plants linked via pipelines) contains processing plants whose total capacity exceeds the total production capacity of its supply fields, the liquefaction plants in this area are defined as Type A.
- **Type B**: If no processing plants exist in the connected area, or if the total processing capacity is smaller than the total production capacity of the supply fields, the liquefaction plants are defined as Type B.[1]

Figures 26 through 34 depict the connections among gas fields, processing plants, and liquefaction facilities for the major LNG exporters (excluding the United States). Each map shows how natural gas travels from fields to terminals, based on the Type A or Type B classifications outlined above.

---

[1] While other scenarios may exist in practice, only these two appear in the original dataset.

Table 14: **Global LNG export terminals outside the US.** Major liquefaction plants by country, including plant IDs and assigned types. Type A indicates onshore terminals with sufficient processing capacity, while Type B denotes terminals lacking sufficient onshore processing.

Liquefaction Plant	**Plant ID**	**Country**	**Type**
Arzew-Bethioua	l_1	Algeria	A
Skikda	l_2	Algeria	A
APLNG	l_3	Australia	A
Darwin	l_4	Australia	B
Gladstone	l_5	Australia	A
Gorgon	l_6	Australia	B
Ichthys	l_7	Australia	B
North West Shelf	l_8	Australia	B
Pluto	l_9	Australia	B
Prelude FLNG	l_10	Australia	B
QCLNG	l_11	Australia	A
Wheatstone	l_12	Australia	B
Bontang	l_13	Indonesia	A
DSLNG	l_14	Indonesia	B
Tangguh	l_15	Indonesia	B
Bintulu	l_16	Malaysia	B
PFLNG 1 Sabah	l_17	Malaysia	B
PFLNG 2	l_18	Malaysia	B
Bonny	l_19	Nigeria	A
Qalhat	l_20	Oman	A
PNG LNG	l_21	Papua New Guinea	A
Ras Laffan	l_22	Qatar	B
Sakhalin II	l_23	Russian Federation	A
Yamal	l_24	Russian Federation	B
Portovaya	l_25	Russian Federation	A
Vysotsk	l_26	Russian Federation	A

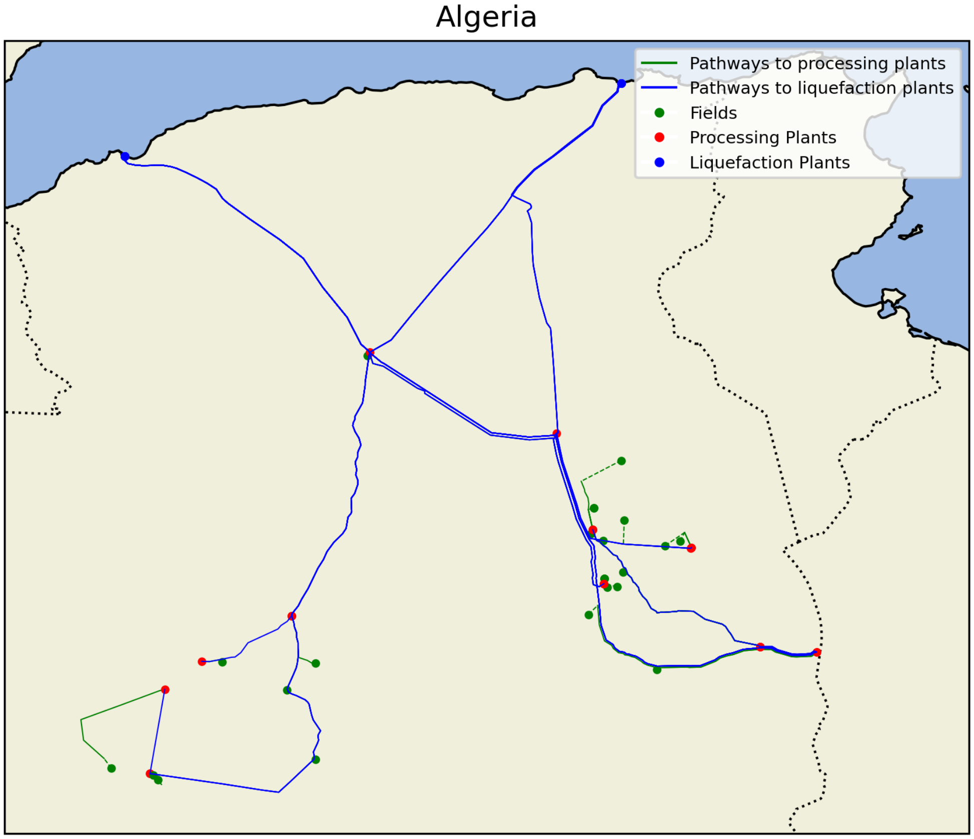

Figure 26: **Algeria**

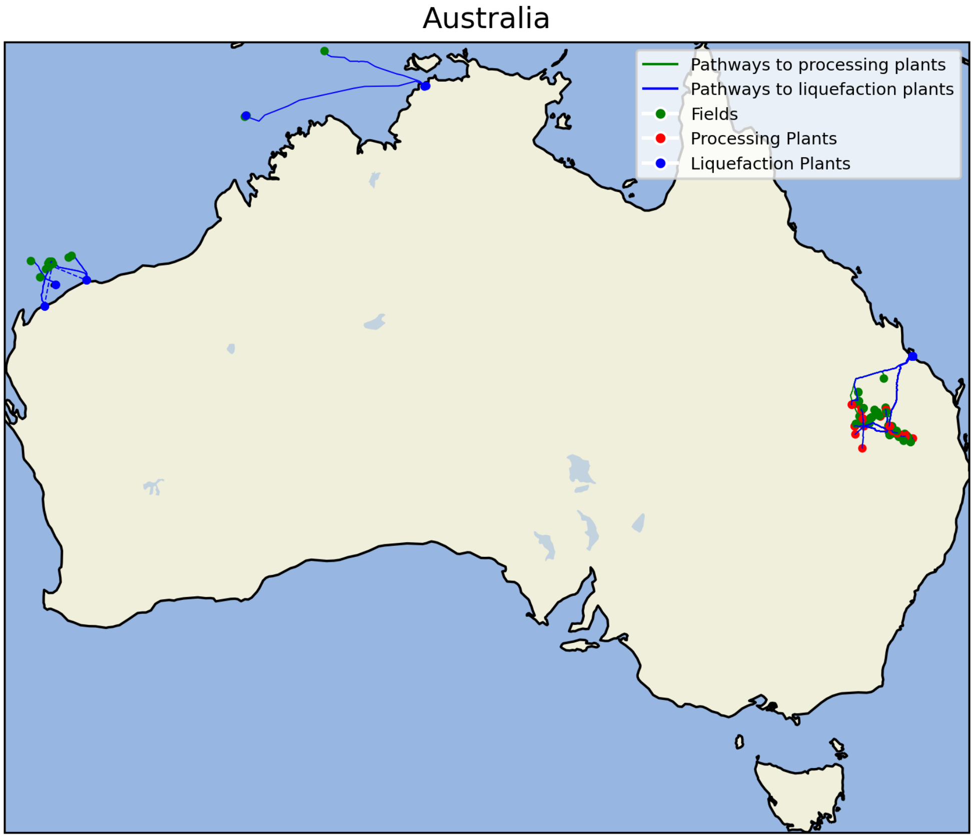

Figure 27: **Australia**

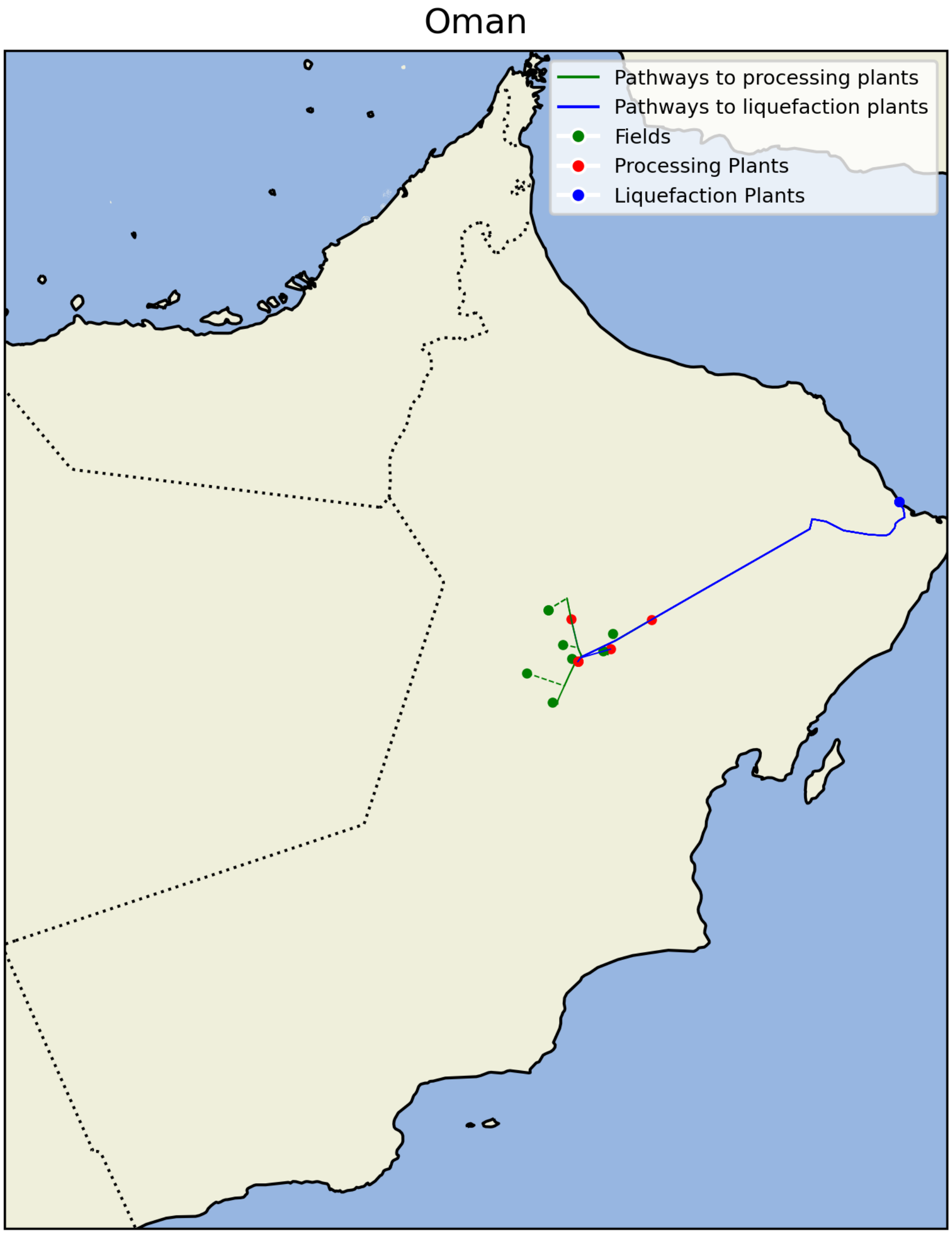

Figure 28: **Oman**

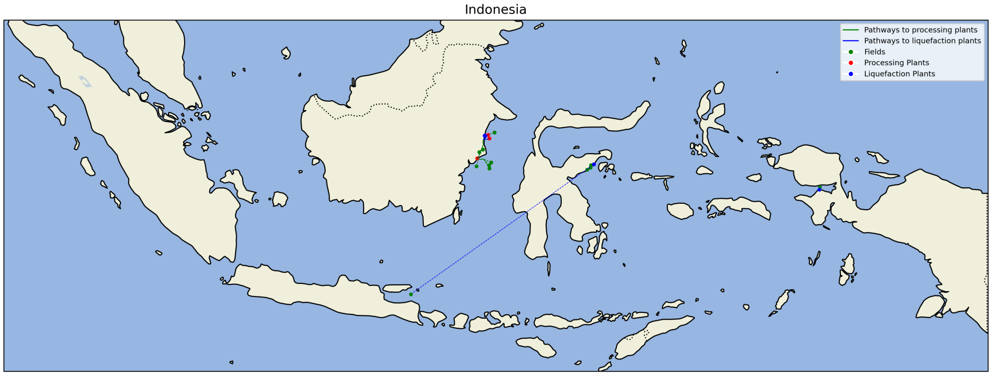

Figure 29: **Indonesia**

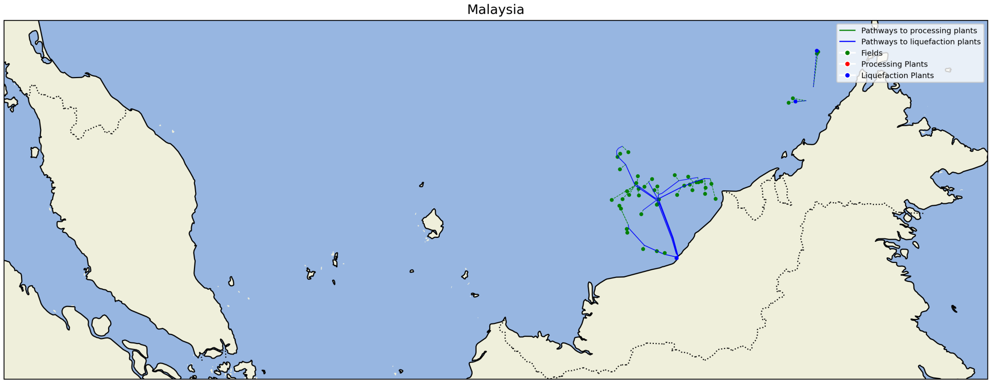

Figure 30: **Malaysia**

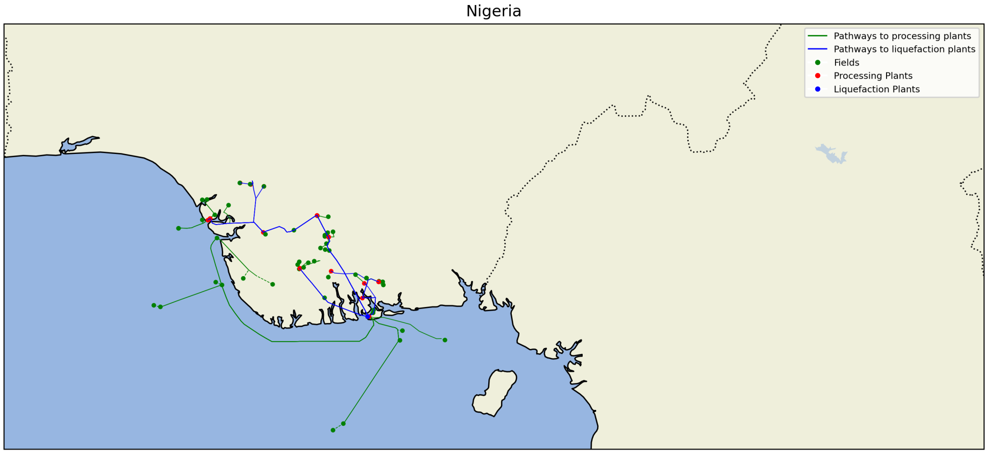

Figure 31: **Nigeria**

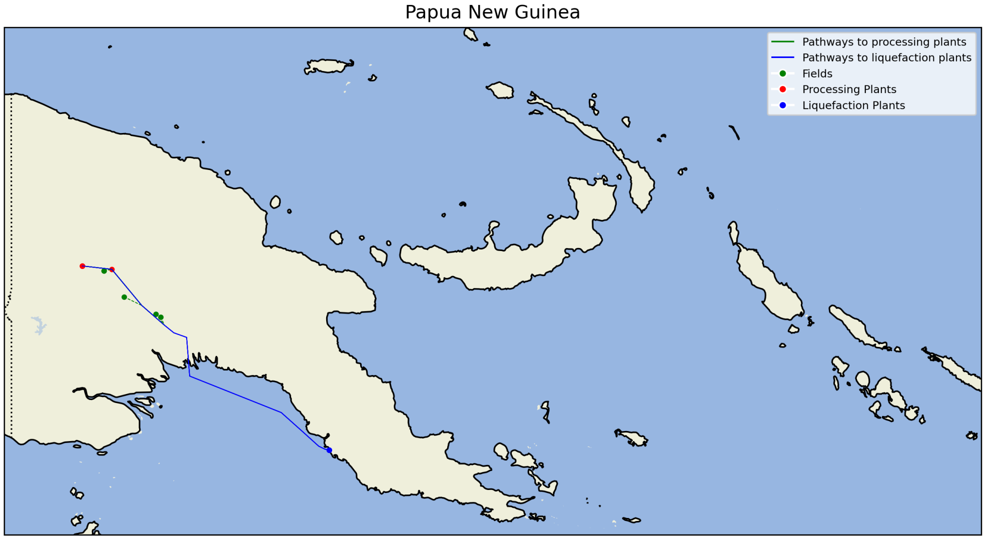

Figure 32: **Papua New Guinea**

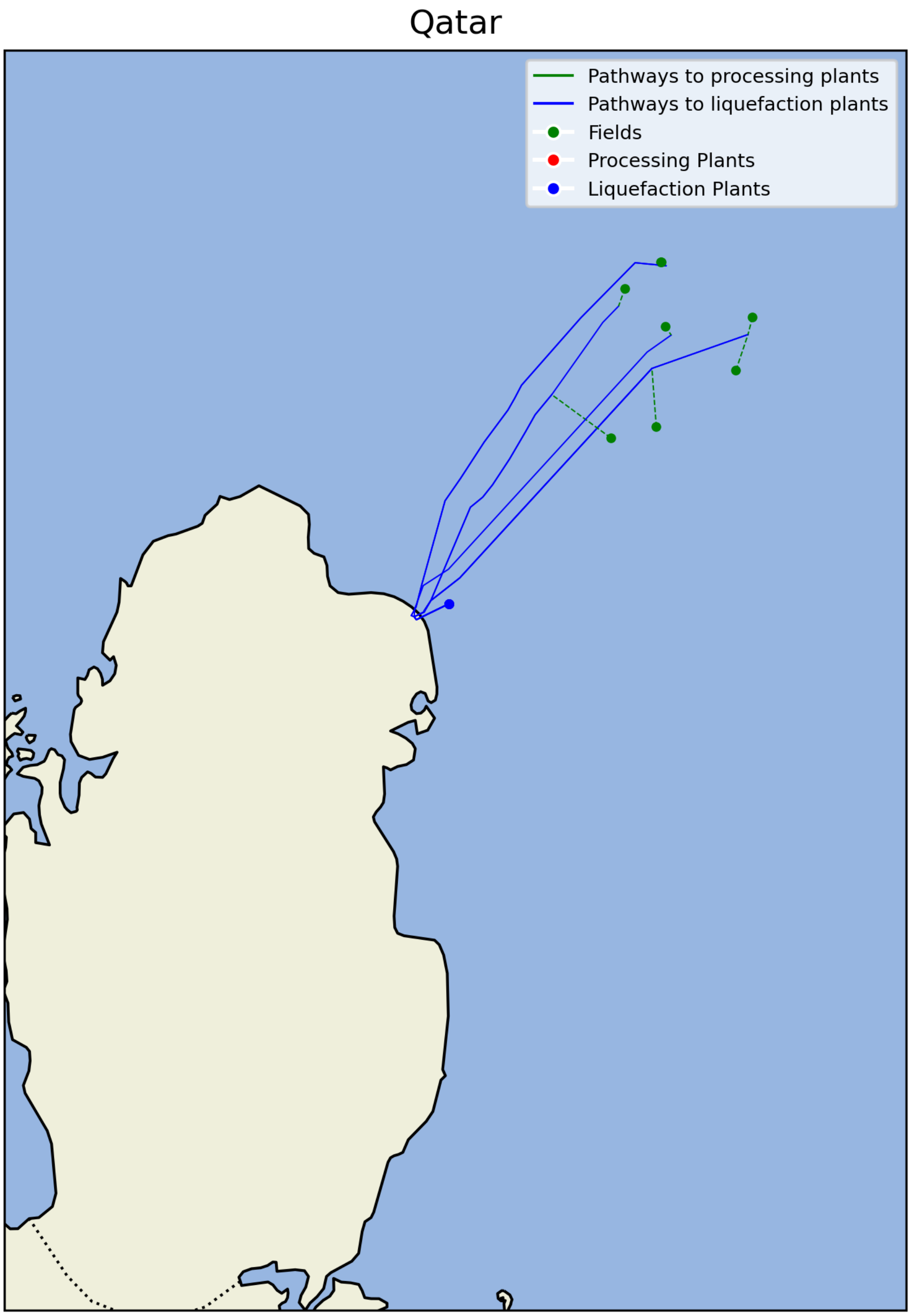

Figure 33: **Qatar**

Figure 34: **Russian Federation**

4.3.3 Methodology

For Type A liquefaction plants, gas processing occurs at centralized facilities within connected pipeline networks. Within each connected area, processing plant capacity must exceed the combined production from both LNG supply fields and all other fields in the network, as these facilities handle the entire area's gas production. Supply fields are located within the connected area, with total production capacity meeting or exceeding export requirements.

We establish two shortest-path datasets following the methodology in Section 4.1: (i) from fields to processing plants and (ii) from processing plants to liquefaction facilities. Each dataset entry contains pathway information between start and end nodes, including integrated facilities, node capacities (supply and demand), and total pipeline length.

The optimization procedure follows Section 4.2 to determine optimal gas transport pathways from supply fields to processing plants. We assume each liquefaction plant connects to all processing plants handling gas from its designated supply fields. Gas flow along pathway i for LNG export is calculated by Equation 25.

$$Q^i = Q^i_{\mathrm{f2p}} \cdot \frac{Q^i_{\mathrm{l}}}{Q^i_{\mathrm{l,\ total\ supply}}} \tag{25}$$

where Q^i represents gas flow for LNG export along pathway i; Q^i_{f2p} is total gas flow from field to processing plant; Q^i_{l} is the liquefaction plant's export capacity; and $Q^i_{\mathrm{l,total}}$ is total production from all supply fields serving the liquefaction plant.

For Type B liquefaction plants, gas undergoes local processing at field sites before transport to liquefaction facilities, eliminating the need for centralized processing plants. Supply field production must meet or exceed export capacity requirements.

Transport methodology depends on the field location:

- Fields within the connected pipeline network: Gas transport follows shortest pathways established per Section 4.1.
- Fields outside the connected network: Alternative transport methods (e.g., truck or ship) are employed, though these are beyond the scope of this analysis.

The gas flow along each pathway i corresponding with LNG can be determined by Equation 26.

$$Q^i = Q^i_{\mathrm{f}} \cdot \frac{Q^i_{\mathrm{l}}}{Q^i_{\mathrm{l,\ total\ supply}}} \tag{26}$$

where Q^i_{f} is the field's total production along pathway i, with other variables defined as in Equation 25.

4.4 Emissions Calculation

Estimating the CI of natural gas pipeline networks requires comprehensive consideration of thermodynamics, fluid mechanics, and emissions dynamics. While natural gas behavior in pipelines generally follows the ideal gas law , real gas behavior under varying pressure and temperature conditions necessitates adjustments using the compressibility factor (Z). The study accounts for multiple critical factors, including pressure drops due to elevation changes and pipeline equipment, temperature variations resulting from ambient conditions and Joule-Thomson effects, flow dynamics affecting pressure drops through friction, and compressor efficiency with associated energy requirements. These interconnected phenomena collectively influence the overall energy consumption and emissions profile of gas transmission systems.

The computational model operates under specific assumptions to ensure physical accuracy and computational feasibility. Gas behavior is considered non-ideal and is corrected using a Z factor as defined in Equation 30. The compression process is modeled as adiabatic with no heat exchange between the compressor and its surroundings, while heat transfer between the gas and the pipeline is assumed to be negligible. Flow conditions are maintained at steady state, and the compression process is treated as isentropic. Gas composition remains constant throughout the pipeline, ensuring consistent thermodynamic properties across the transmission network. These assumptions provide a mathematically tractable framework while maintaining engineering accuracy.

Operating pressures are established based on global standards from major natural gas networks (Table 15). The maximum operating pressure is set at 10.73 MPa, representing the average of maximum pressures across worldwide transmission systems. This standardization ensures compatibility with existing infrastructure while optimizing performance across different operational regions. The selected pressure range balances the need for efficient gas transport against safety considerations and material limitations. Regional variations in pressure standards reflect local geological conditions, regulatory frameworks, and historical infrastructure development patterns.

The comprehensive emissions model quantifies the CI of natural gas transmission through Equation 27. This formulation integrates thermodynamics, fluid mechanics, and emissions calculations by dividing total carbon dioxide equivalent emissions by LNG production volume. Total GHG emissions are calculated by multiplying compressor energy consumption by the grid emission factor,

Table 15: **Global transmission pipeline pressure standards.** Values from major natural gas networks worldwide.

Region	Average (MPa)	Maximum (MPa)	Source
China	8.3	9.85	(*38*)
Europe	6.7	12.0	(*39*)
United States	5.8	10.34	(*40*)

representing the emissions associated with electricity generation. Annual LNG production is determined by the product of flow rate and operational days. This methodology provides a standardized metric for comparing emissions across different pipeline networks and operating conditions.

$$CI = \frac{CO_{2e}}{LNG_{\text{production}}} \tag{27}$$

Compressor energy consumption calculation forms the cornerstone of emissions estimation, as shown in Equation 28. The energy required for compression depends on both the work performed and the efficiency of the compressor system. Reciprocating compressors, commonly used in pipeline applications, typically achieve 75% efficiency. The compressor work is determined through Equation 29, which accounts for real gas behavior through the compressibility factor. This integration enables accurate prediction of energy requirements under varying operational conditions.

$$E_c = \frac{W_c}{\eta} \tag{28}$$

$$W_c = \int_{V_1}^{V_2} Z \cdot P \cdot dV = Z \cdot P \cdot (V_2 - V_1) \tag{29}$$

The Z factor in Equation 30 accounts for deviations from ideal gas behavior under actual pipeline conditions. This empirical correlation adjusts for intermolecular forces and finite molecular volumes that become significant at elevated pressures. The relationship between volume, pressure, and temperature follows Equation 31, incorporating both real gas behavior and process thermodynamics. Temperature variations during compression are described by Equation 32, ensuring accurate thermal state predictions throughout the transmission process.

$$Z = \frac{100}{100 + 1.734 \cdot P_i^{1.15}} \tag{30}$$

$$V_2 = \frac{V_1 \cdot P_1 \cdot T_1}{P_2 \cdot T_2 \cdot Z} \tag{31}$$

$$T_2 = \frac{T_1 \cdot P_2}{Z \cdot P_1} \tag{32}$$

Pressure drop calculations consider both frictional losses and elevation effects through Equation 33. Frictional pressure drop follows the Darcy-Weisbach equation (Equation 34), modified for compressible flow. The friction factor varies with flow regime, transitioning between laminar and turbulent conditions as described in Equation 35. Gas properties required for these calculations, including viscosity and density, are determined using established correlations that account for composition and state conditions.

$$\Delta P_{\text{total}} = \Delta P_{\text{friction}} + \Delta P_{\text{elevation}} \tag{33}$$

$$\Delta P_{\text{friction}} = f \cdot \frac{L \cdot \rho \cdot V^2}{2D_i} \tag{34}$$

$$f = \begin{cases} 0.00958 \cdot D^{-0.2} & \text{for turbulent flow} \\ \frac{64}{Re} & \text{for laminar flow} \end{cases} \tag{35}$$

Gas viscosity calculations employ the Lee et al. correlations (Equation 36) to account for temperature, pressure, and compositional effects. Parameters L_1, L_2, and L_3 are temperature and composition-dependent coefficients defined in Equations 37, 38, and 39. These correlations provide accurate viscosity predictions across the operational range of natural gas pipelines. The density calculation (Equation 40) incorporates the compressibility factor to account for real gas behavior under varying pressure and temperature conditions.

$$\mu = L_1 \exp\left[L_2 \left(\frac{\rho}{A}\right)^{L_3}\right] \tag{36}$$

$$L_1 = 10^{-4}\frac{(7.77 + 0.0063M)T^{1.5}}{122.4 + 12.9M + T} \tag{37}$$

$$L_2 = 2.57 + \frac{1914.5}{T} + 0.0095M \tag{38}$$

$$L_3 = 1.11 + 0.04L_2 \tag{39}$$

$$\rho = \frac{P \cdot M}{Z \cdot R \cdot T_f} \tag{40}$$

Temperature profile modeling within pipelines uses Equation 41 to predict gas temperature variations along the transmission route. This equation considers heat transfer between the gas and the surrounding soil, accounting for burial depth and thermal properties of both the soil and pipeline materials. The fluid flow temperature influences gas density and viscosity, directly affecting pressure drop calculations and energy requirements. Accurate temperature predictions are essential for optimizing compressor placement and ensuring safe operation within design parameters.

$$T_f = \frac{t \cdot h \cdot T_s + T_i}{1 + h \cdot t/k} \tag{41}$$

The model segments pipelines into 140 km sections between compressor stations, aligning with engineering practice for efficient transmission system design. This spacing optimizes the balance between pressure maintenance and infrastructure investment while ensuring reliable gas delivery. Pipeline burial depth is standardized at 2.5 m per ASME B31.8-2003 specifications to provide adequate protection and thermal stability (*41*). Maximum allowable pressure drop per segment and country-specific annual average ambient temperatures are incorporated to ensure region-specific accuracy. These operational parameters collectively define the boundary conditions for emissions calculations.

Emissions calculations proceed systematically for each pipeline segment, incorporating local conditions and regional grid emission factors. This geographic granularity enables an accurate assessment of transmission emissions across diverse operational environments. The approach accounts for variations in climate, topography, and electricity generation mix that significantly impact overall CI. Final emissions estimates aggregate segment-level calculations to provide comprehensive system-wide CI metrics.

5 Downstream

5.1 Liquefaction

Liquefaction modeling involves six main processes: gas reception, carbon dioxide removal (sweetening), cryogenic cooling (liquefaction), helium extraction, utilities (power generation), and flaring (routine and non-routine). We assumed utility energy distribution as follows: 10% for sweetening, 80% for liquefaction, and 10% for helium extraction. Energy consumption varies widely across 21 technologies grouped into nine categories (Table 16). Optimized single mixed refrigerant (SMR_opt) systems use the least energy (750 kJ/kg LNG), while certain propane pre-cooled mixed refrigerant (C3MR) configurations reach up to 1300 kJ/kg LNG. Liquefaction ratios mostly range from 92% to 94%, with Technip/Air Liquide technology performing best at 96–97%. Facility size impacts energy efficiency, generally improving with larger capacities (>4 MMtpa). Table 17 presents the technology distribution and performance metrics by country for major LNG exporters.

Table 16: **Specific Energy Consumption and Liquefaction Ratio by Technology Type**

Technology Group	Description	Specific Energy Consumption (kJ/kg LNG)	Liquefaction Ratio (%)	Prevalence (% global capacity)
C3MR	Propane pre-cooled mixed refrigerant	850-1250	92-94	42.3
DMR	Dual mixed refrigerant	1100-1150	92-93	15.7
Cascade	ConocoPhillips Optimized Cascade	950-1100	91-93	14.2
AP-X	Air Products expansion-based technology	850-900	85-90	9.5
SMR	Single mixed refrigerant	950-1050	91-93	7.8
MFC/LIMUM	Mixed fluid cascade	875-925	92-94	5.1
PRICO	Black & Veatch single mixed refrigerant	950-1050	91-92	3.6
Technip/Air Liquide	Air Liquide cascade technology	900-950	96-97	1.2
SMR_opt	Optimized single mixed refrigerant	750-850	92-93	0.6

The global volume-weighted average CI for LNG liquefaction is 2.3 g CO_2eq./MJ, with significant variation across facilities and countries, as illustrated in Figure 35. Approximately 80% of global liquefaction capacity operates below 3.0 g CO_2eq./MJ, while some facilities, particularly

Table 17: **Technology Distribution by Country for Major LNG Exporters**

Country	Dominant Technologies	Average SEC (kJ/kg LNG)	Average Liquefaction Ratio (%)
Qatar	C3MR, AP-X	950	93
Australia	C3MR, Cascade	1000	92
United States	Cascade, SMR	1030	92
Russia	C3MR, DMR	1050	93
Malaysia	DMR	1120	93
Indonesia	C3MR	980	92
Nigeria	C3MR, DMR	1015	93
Algeria	C3MR, MFC	975	93
Oman	C3MR	990	93
Papua New Guinea	SMR_opt	820	92

plants in the Ichthys, Australia, exhibit substantially higher values (10 g CO_2eq./MJ). Country-level analysis reveals that Qatar, Malaysia, Indonesia, and Papua New Guinea demonstrate the lowest CI (1.5-2.0 g CO_2eq./MJ), reflecting both advanced technology deployment and efficient facility design. The United States exhibits the highest average CI (2.9 g CO_2eq./MJ) with substantial facility-to-facility variation (2.0-6.7 g CO_2eq./MJ).

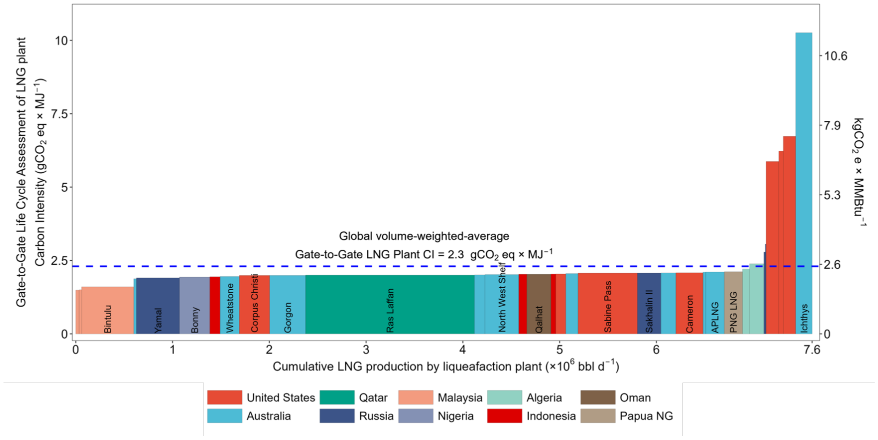

Figure 35: **Carbon intensity distribution across global LNG liquefaction facilities.** Bar chart showing gate-to-gate CI (gCO_2eq/MJ) by facility, organized by cumulative LNG production. The global volume-weighted average of 2.3 gCO_2eq/MJ is indicated by the horizontal dashed line. Most facilities operate below this threshold, with notable exceptions being three U.S. facilities and the Ichthys facility in Australia that exceed 5 gCO_2eq/MJ. Facilities are color-coded by country of origin, showing the geographic distribution of liquefaction capacity.

Figure 36 shows that the liquefaction step itself accounts for approximately 95% of emissions, with the remaining 5% associated with C2-C4 production. This distribution remains consistent across most facilities regardless of technology type or geographic location, indicating the fundamental energy requirements of cryogenic cooling dominate the emissions profile.

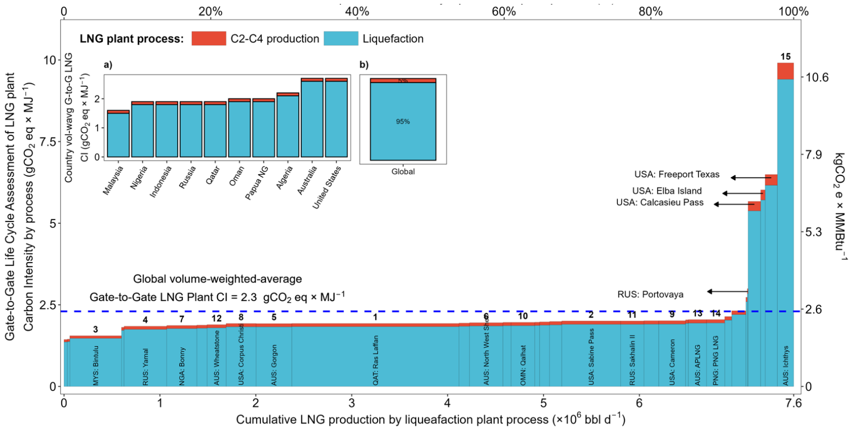

Figure 36: **Carbon intensity contributions by process across global LNG facilities.** Main chart shows the distribution of emissions across facilities, with contributions from liquefaction (blue) and C2-C4 production (red) processes. Inset (a) shows country-level average CI, with liquefaction dominating across all countries. Inset (b) presents the global average distribution, where liquefaction accounts for 95% of total CI. High-intensity U.S. facilities (Freeport Texas, Elba Island, Calcasieu Pass) are labeled, along with the lower-intensity Russian Portovaya facility. The global weighted average (2.3 gCO_2eq/MJ) is indicated by the horizontal dashed line.

As shown in Figure 37, three principal emission sources contribute to liquefaction CI: utility systems (66.3%), flaring operations (33.2%), and venting (0.5%). Facilities employing waste heat recovery systems demonstrate significantly lower utility-related emissions, suggesting a clear pathway for reducing CI in existing operations.

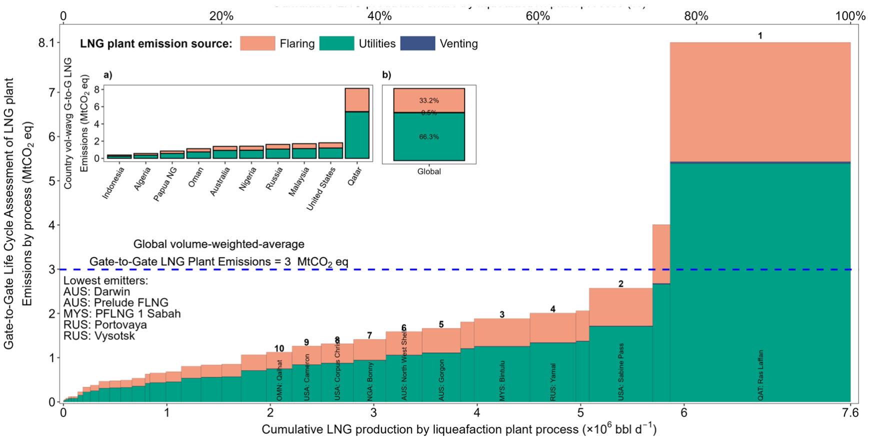

Figure 37: **Distribution of emissions by source across LNG liquefaction facilities.** Bar chart showing the contribution of different emission sources—utilities (green), flaring (salmon), and venting (navy)—to total emissions (MtCO$_2$eq) across facilities. Inset (a) presents country-level emissions by source, while inset (b) shows the global average distribution: utilities (66.3%), flaring (33.2%), and venting (0.5%). The lowest-emitting facilities are identified in the main figure. The horizontal dashed line represents the global volume-weighted average of 3 MtCO$_2$eq.

5.2 Shipping

This study examines LNG shipping emissions across global trade routes based on 5,088 voyages from ten major LNG exporters in 2022. The dataset covers 35 export terminals and 123 import terminals across 36 countries. Each voyage was modeled as a round trip, with the laden voyage (origin to destination) and ballast voyage (return trip). Table 18 lists the voyage count for each exporter. Fuel consumption and emissions were estimated using manufacturer specifications and published literature for different engine types (Table 19). Propulsion system efficiency for each engine type was determined based on literature data (Table 20).

Table 18: **Voyage count and cargo volume for LNG exporters.** Number of voyages, cargo volumes, and export terminals for each country in 2022.

Country	Voyage Count	Cargo (tons)	Export Terminals
Nigeria	213	13,751,787	1
Algeria	209	9,978,089	2
United States	1,018	67,449,546	7
Qatar	1,056	78,315,491	1
Malaysia	508	27,351,755	4
Indonesia	179	10,870,913	4
Oman	171	10,970,798	1
Russia	473	31,142,109	4
Australia	1,152	76,601,893	10
Papua New Guinea	109	8,255,408	1
Total	5,088	334,687,789	35

Installed engine capacity was estimated using vessel gross tonnage (GT), following the method from the EMEP/EEA guidebook (*42*), as shown in Equation 42:

$$P_{\text{installed, ME}} = 14.755 \times (\text{GT})^{0.6082} \tag{42}$$

Auxiliary engine capacity was calculated as a proportion of the main engine capacity (*43, 44*), according to Equation 43:

$$P_{\text{installed, AE}} = (0.211 \text{ to } 0.30) \times P_{\text{installed, ME}} \tag{43}$$

Table 19: **Engine characteristics for different LNG carrier propulsion systems.** Summary of fuel consumption requirements and methane slip data for various marine engine types.

Engine Type	Gas Fuel Requirement (g/kWh)	Liquid Fuel Requirement (g/kWh)	Methane Slip Factor (g CH_4/kWh)
MEGI	141.1	169 (Diesel)	0.2–0.3
XDF	139.3–142.5	180.2–182.2 (Diesel)	2.5–3.2
DFDE/TFDE	156.4–171.8	186.3–203.2 (Fuel Oil)	5.3–5.5
Steam[a]	218.1	263.8 (Fuel Oil)[b]	0.04
SSD	—	170–190	0–0.05
STaGE	140–160	250–280 (Fuel Oil)	0.1–0.2

[a] Estimated using LHV of natural gas (13.1 kWh/kg) and steam engine efficiency (35%) on an LHV basis.

[b] Estimated using LHV of heavy fuel oil (10.83 kWh/kg) and steam engine efficiency (35%) on an LHV basis.

Table 20: **Propulsion system efficiency ranges for marine engines.** Efficiency values for different engine types used in LNG carriers, expressed as fractions.

Engine Type	Low (fraction)	Expected (fraction)	High (fraction)
MEGI	0	0.50	0
XDF	0.4638	0	0.4690
DFDE/TFDE	0.4543	0	0.4955
Steam	0	0.3499	0
SSD	0.4858	0	0.5429
STaGE	0.3297	0	0.3692

5.2.1 Estimation of voyage duration and speed

Voyage duration was estimated by dividing voyage distance by average speed. To address left-skewed speed distribution caused by idling periods, we established a threshold average speed using a triangular distribution (mean: 14.4 knots, 95% CI: 14.3-14.5 knots). Speeds below this threshold were adjusted, and idling duration was calculated as the difference between the original and recalculated cruising durations. Ballast voyages were modeled without idling to avoid overly conservative results.

These calculations used Equations 44-46:

$$\text{Original Voyage Duration (days)} = \frac{D}{v \times 24} \tag{44}$$

$$\text{Cruising Voyage Duration (days)} = \frac{D}{v_{\text{threshold}} \times 24} \tag{45}$$

$$\text{Idling Duration (days)} = T_{\text{orig}} - T_{\text{cruise}} \tag{46}$$

where D represents voyage distance (nautical miles), v is average voyage speed (knots), and $v_{\text{threshold}}$ is the threshold average speed.

The mean voyage speed from 3,777 voyages was 14.4 knots (SE: ±0.055 knots), modeled using a triangular distribution (Table 21).

Table 21: **Statistical parameters for voyage speed modeling.** Triangular distribution values are used to establish threshold voyage speeds.

Parameter	P2.5	Expected	P97.5
Threshold Average Voyage Speed	14.3	14.4	14.5

This threshold assumption was validated against literature values for tanker service speeds (Table 22).

Table 22: **Historical service speed data for tanker vessels.** Average speeds reported by different sources.

Source	Speed (knots)
ICF International (2009)	14.8
U.S. EPA (2009)	13.2
Brown and Aldridge (2019)[a]	14.86 ± 3.86
Aframax[b]	15.33 ± 1.72

[a] Values for Panamax vessels (55,000–80,000 DWT)
[b] Values for Aframax vessels (80,000–120,000 DWT)

Literature-based load factors for main and auxiliary engines were used to estimate power consumption during service and idling cycles (Table 23).

Table 23: **Load factors for ship engine operations.** Load factors during different vessel activities.

Engine Type	Service Cycle	Maneuvering & Hoteling
Main	0.80–0.85	0.2
Auxiliary	0.13–0.30	0.5–0.6

5.2.2 Fuel consumption and emissions estimation

During each voyage, a portion of the LNG vaporizes as boil-off gas (BOG), which was used to meet vessel power requirements (*45*). The boil-off rate (BOR) was modeled based on Kpler data for laden voyages, while ballast BOR was taken from literature (*46*). When BOG was insufficient, a mix of diesel oil and residual fuel oil was used. The fuel consumption modeling decision process is summarized in Algorithm 1. The emission factors for marine fuel combustion were obtained from NETL (*47*), and the CI for each voyage was calculated by normalizing the total GHG emissions by the LNG delivered quantity.

Algorithm 1 Fuel consumption modeling for LNG carriers. Decision process for allocating boil-off gas (BOG) and supplementary fuels.

```
Require: BOG Generation Rate, Total Power Requirement, ME Power Requirement
Ensure: Fuel Allocation Strategy
if BOG Generated $>$ Total Power Requirement then
    BOG fuels the entire voyage
    Excess BOG combusted in the gas combustion unit
else
    if BOG Generated $\geq$ ME Power Requirement then
        BOG fuels ME and part of AE
        Remaining power requirement met by FO/DO mix
    else
        BOG fuels part of ME
        Remaining ME + AE power requirement met by FO/DO mix
    end if
end if
```

The quantity of LNG loaded was calculated using Equation 47:

$$LNG_{\text{loaded}} = 0.98 \times C \times \rho \tag{47}$$

where C represents vessel capacity (m^3) and ρ is LNG density (kg/m^3). The ballast heel requirement was determined using Equation 48:

$$H_{\text{required}} = 0.025 \times C \times \rho \tag{48}$$

BOG generated during the laden voyage was calculated according to Equation 49:

$$BOG_{\text{generated, laden}} = BOR_{\text{laden}} \times C \times T \times \rho \tag{49}$$

where T is voyage duration (days). The LNG delivered quantity was then estimated using Equation 50:

$$LNG_{\text{delivered}} = LNG_{\text{loaded}} - BOG_{\text{generated, laden}} - H_{\text{required}} \tag{50}$$

The terminal-level analysis reveals significant variations in LNG consumption during shipping. LNG used as shipping fuel ranges from nearly 0% to 3.7% of exported volumes (Table 24). U.S. terminals generally show higher consumption rates, with Sabine Pass (3.3%), Cove Point (2.8%), and Corpus Christi (2.0%) demonstrating notably elevated values. Australia's QCLNG terminal exhibits the highest overall percentage (3.7%), contrasting sharply with other Australian facilities like Darwin (0.1%) and Ichthys (0.1%). These variations reflect differences in shipping distances, vessel types deployed from each terminal, and trade patterns established with importing markets.

This study shows significant variations in shipping CI across different exporters. Figure 38 shows the volume-weighted average shipping CI for major LNG exporters. The United States has the highest average CI (0.117 g CO_2eq./g LNG), followed by Nigeria (0.106 g CO_2eq./g LNG), while Algeria demonstrates the lowest (0.035 g CO_2eq./g LNG). These differences reflect variations in shipping distances, vessel types, and trade patterns. Importers also show distinct CI patterns (Figure 39). Asian countries demonstrate higher CI values due to longer shipping distances. The variation in CI for each country, shown by error bars, indicates the diversity of their supply sources. These results demonstrate that while shipping distance is a major factor in determining CI, vessel type and operational efficiency also play important roles. Countries with newer vessel fleets or more efficient routing generally show lower CI values than their shipping distances would suggest.

Table 24: **LNG consumption during shipping by export terminal.** Consumption is presented as both absolute values and as a percentage of total exported LNG. Higher percentages generally correspond to longer shipping distances and older vessel fleets.

Terminal	**LNG Shipping Consumption (t/y)**	**Exported LNG (t/y)**	**Consumption Percentage**
QCLNG (Australia)	278,965	7,453,676	3.7%
Sabine Pass (USA)	915,017	27,415,970	3.3%
Cove Point (USA)	125,049	4,462,188	2.8%
Corpus Christi (USA)	261,628	13,248,875	2.0%
Calcasieu Pass (USA)	98,714	5,607,665	1.8%
Freeport Texas (USA)	77,980	5,339,899	1.5%
Tangguh (Indonesia)	66,443	4,791,832	1.4%
Gorgon (Australia)	187,011	16,140,097	1.2%
Wheatstone (Australia)	94,631	9,009,037	1.1%
Cameron (USA)	123,794	10,904,920	1.1%
North West Shelf (Australia)	134,223	15,103,704	0.9%
Portovaya (Russia)	3,341	365,046	0.9%
Prelude FLNG (Australia)	10,093	1,287,219	0.8%
Yamal (Russia)	164,056	20,024,850	0.8%
APLNG (Australia)	61,209	8,906,422	0.7%
Skikda (Algeria)	22,313	3,296,943	0.7%
Elba Island (USA)	15,189	2,087,400	0.7%
Ras Laffan (Qatar)	524,833	78,840,324	0.7%
Bintulu (Malaysia)	153,298	24,556,216	0.6%
Arzew-Bethioua (Algeria)	39,712	6,743,171	0.6%
Qalhat (Oman)	58,053	11,028,851	0.5%
Bonny (Nigeria)	58,752	13,810,539	0.4%
PNG LNG (Papua New Guinea)	36,066	8,291,474	0.4%
Gladstone (Australia)	20,459	5,811,894	0.4%
Pluto (Australia)	19,144	4,944,884	0.4%
Bontang (Indonesia)	12,075	3,421,338	0.4%
PFLNG 2 (Malaysia)	3,127	1,618,980	0.2%
Sakhalin II (Russia)	24,180	10,848,456	0.2%
PFLNG 1 Sabah (Malaysia)	651	1,139,763	0.1%
Ichthys (Australia)	11,106	7,453,233	0.1%
Darwin (Australia)	1,543	1,310,110	0.1%
DSLNG (Indonesia)	673	2,211,246	0.0%
Vysotsk (Russia)	0	95,334	0.0%

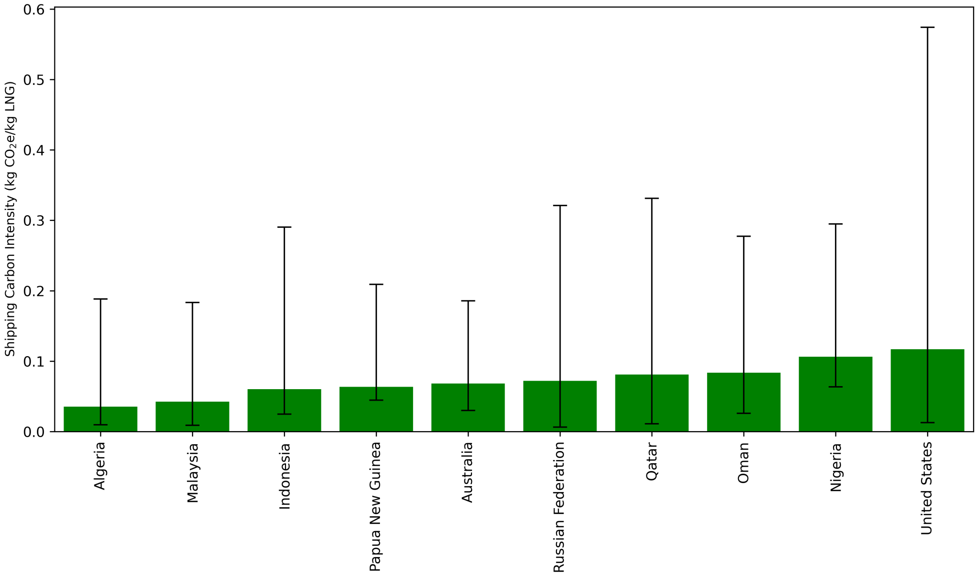

Figure 38: **Shipping carbon intensity varies significantly among LNG exporters.** Volume-weighted average shipping CI ranges from 0.035 to 0.117 g CO_2eq./g LNG. Error bars show each country's minimum and maximum CI values, reflecting route and vessel type variations.

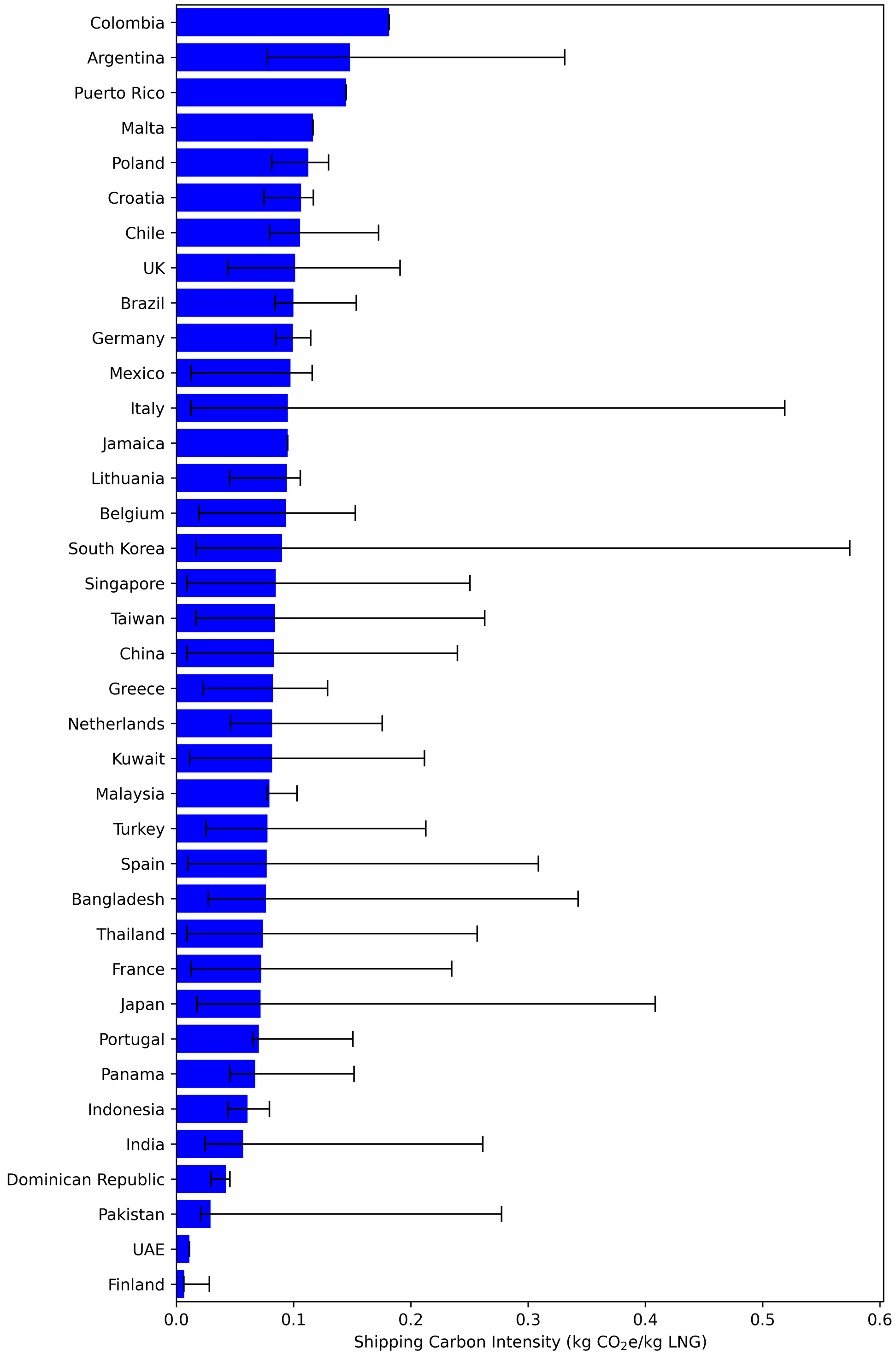

Figure 39: **Importers show systematic differences in shipping carbon intensity.** The variation in CI reflects the geographical location and diversity of supply sources. Asian importers generally show higher CI values due to longer transportation distances.

5.3 Regasification

This study covers 155 LNG regasification terminals across 36 importers in 2022. These terminals have a total production capacity of 394 million tonnes per annum (MTPA) with an average utilization factor of 0.48.

5.3.1 Terminal classification

We classify terminals into three categories based on capacity (*48–50*): small-scale (≤ 0.45 MTPA), medium-scale (0.45–3 MTPA), and large-scale (≥ 3 MTPA). The specific electricity consumption (SEC) varies by terminal size according to Equation 51:

$$SEC = \begin{cases} 0.97\ \mathrm{MJ}_e/\mathrm{GJ}_{\mathrm{LNG}} & \text{for small-scale} \\ 0.93\ \mathrm{MJ}_e/\mathrm{GJ}_{\mathrm{LNG}} & \text{for medium-scale} \\ 0.89\ \mathrm{MJ}_e/\mathrm{GJ}_{\mathrm{LNG}} & \text{for large-scale} \end{cases} \tag{51}$$

Table 25 summarizes the key operational parameters and emissions data for global LNG regasification facilities.

Table 25: **Global regasification terminal characteristics for 2022.** Summary of key operational parameters and emissions data for global LNG regasification facilities.

Parameter	Value
Number of terminals	155
Total production (MTPA)	394
Total capacity (MTPA)	822
Average utilization factor	0.48
Total electricity consumption (GWh/y)	4,509.8
Total emissions (kt CO_2eq./y)	3,036.4
Grid CI range (g CO_2eq./MJ electricity)	1.75–386.8
Regasification CI range (g CO_2eq./MJ LNG)	0.018–0.34

5.3.2 Emissions calculation

The CI of regasification operations primarily depends on terminal efficiency and local grid emission factors. Terminal-specific emissions are calculated using Equation 52:

$$E = P \times SEC \times GEF \tag{52}$$

where E represents total emissions, P is production volume, and GEF is the grid emission factor. The CI for each terminal is then determined by Equation 53:

$$CI = \frac{E}{P} \tag{53}$$

Total emissions from regasification terminals reached 3,036.4 kt CO_2eq. in 2022. The significant variation in grid emission factors across countries (1.75–386.8 g CO_2eq./MJ electricity) leads to a wide range in CI (0.018–0.34 g CO_2eq./MJ LNG). The most common regasification method is the Open Rack Vaporizer (ORV), which uses seawater as a heat source for LNG vaporization (*49*).

This study shows distinct patterns across terminal scales as illustrated in Figure 40. Large-scale terminals dominate total emissions, with Asia Pacific facilities showing the highest CI values. Medium-scale terminals demonstrate moderate CI values, typically ranging from 0.1 to 0.2 g CO_2eq./MJ LNG. Small-scale terminals show varied performance but generally contribute less to total emissions due to their lower throughput volumes despite having slightly higher specific electricity consumption.

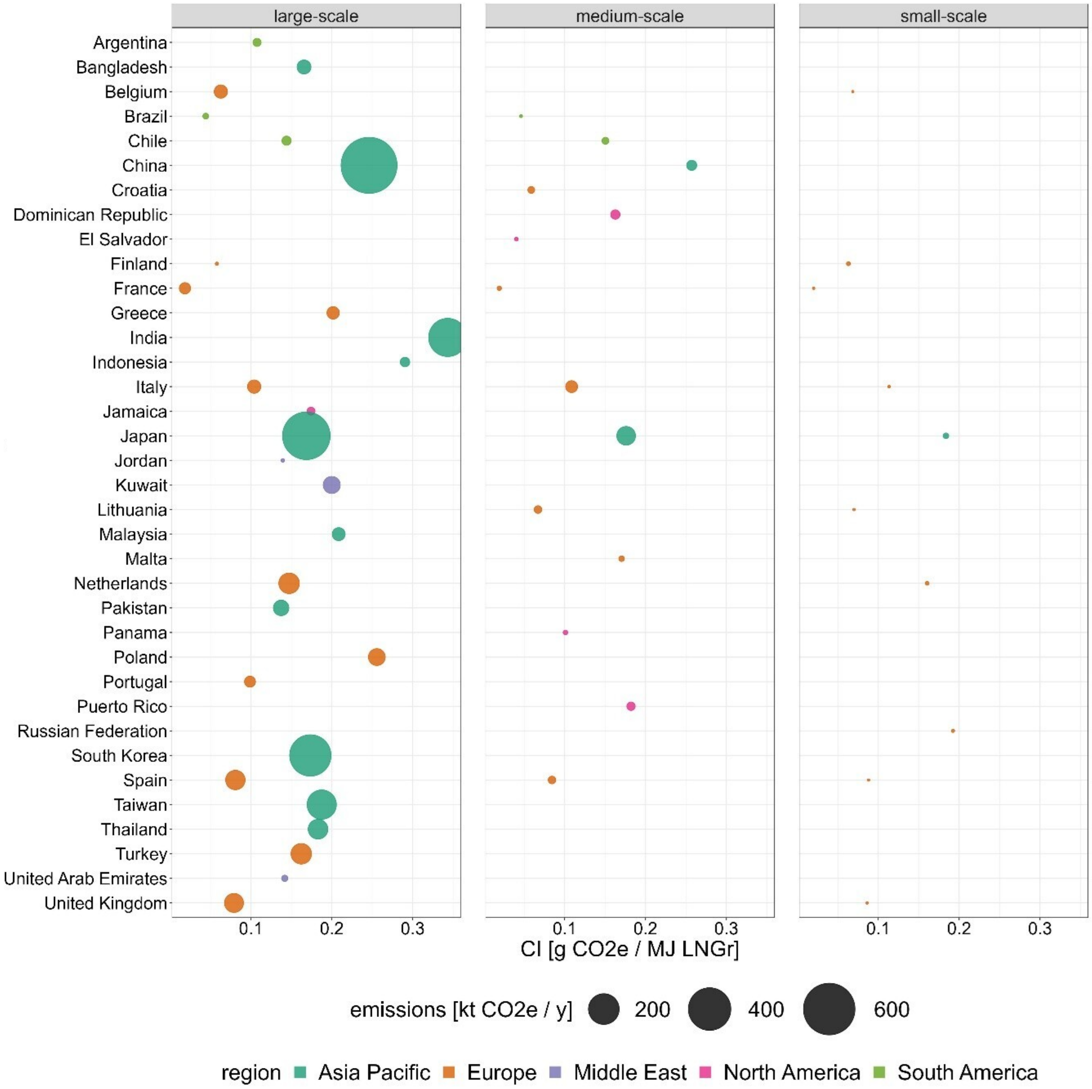

Figure 40: **Global distribution of regasification carbon intensity by terminal scale.** CI (g CO_2eq./MJ LNG) are shown for all terminals, categorized by scale (large: ≥3 MTPA, medium: 0.45–3 MTPA, small: ≤0.45 MTPA). Circle sizes represent annual emissions (kt CO_2eq./y), reaching up to 600 kt CO_2eq./y for large facilities. Colors indicate regions: Asia Pacific (green), Europe (orange), Middle East (purple), North America (pink), and South America (light green). Large-scale terminals in Asia Pacific, particularly in China, India, and Japan, show the highest emissions due to carbon-intensive grids and high throughput volumes.

Additional Results

6 Field-level results

6.1 Field-level CI

Figure 41 presents the distribution of CI across LNG fields by value chain, as modeled in OPGEE (Section 1.1, Figure 4). Methane emissions account for the largest portion of total emissions. Surface processing represents the second largest contribution across the majority of fields examined. Production emissions, grid electricity upstream emissions, and transport emissions contribute comparatively smaller portions, though their relative significance varies by geographic location and production characteristics.

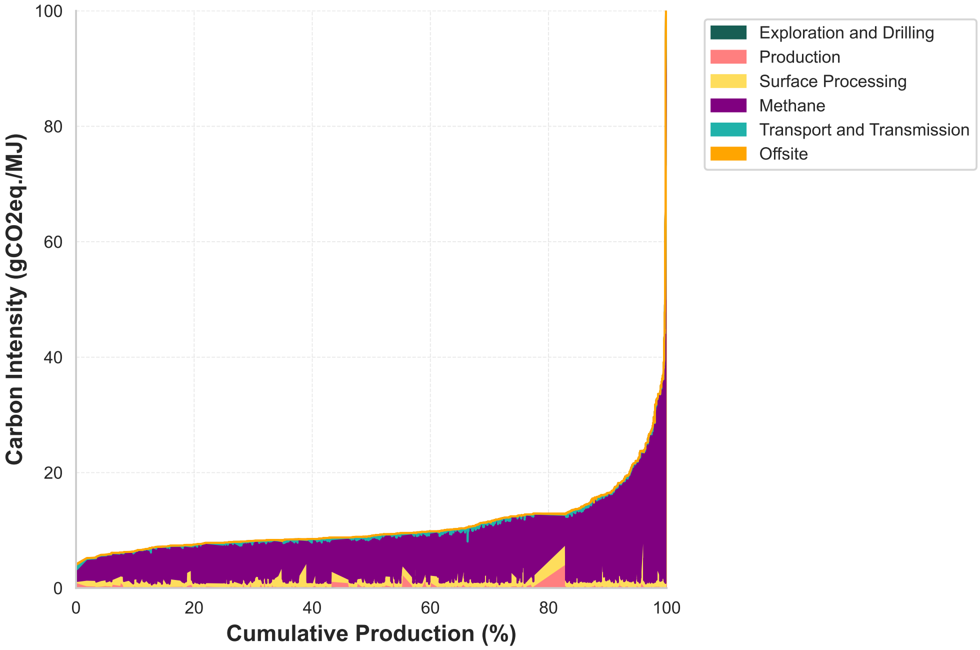

Figure 41: **Field-level CI distribution.** Fields are ranked by total CI and plotted against cumulative energy content. Colors show contributions from different life cycle stages. Methane emissions (purple) dominate most fields' CI. Surface processing (yellow) is the second largest contributor.

6.2 Field-level methane loss rate

Field-level MI varies dramatically across global LNG production, with pronounced disparities between superemitters and non-superemitters. As shown in Figure 42, fields ranked by MLR demonstrate that approximately 80% of cumulative methane production maintains relatively stable MI values below 2%, predominantly comprised of non-superemitter sources. However, a steep gradient emerges in the final 20% of production, with MI values escalating dramatically.

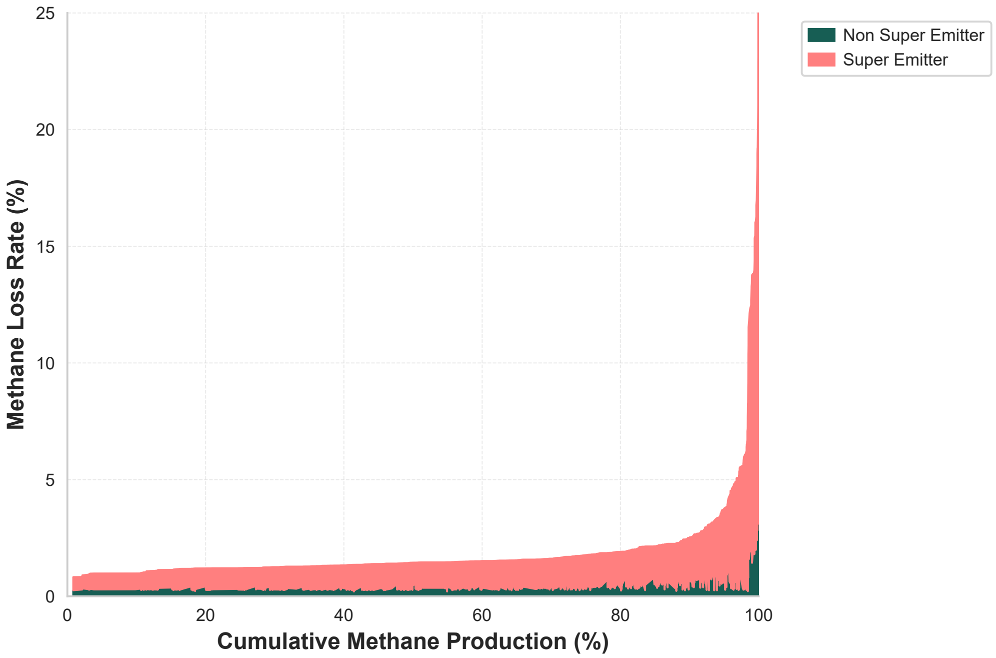

Figure 42: **Field-level methane loss rate distribution.** Fields are ranked by MLR and plotted against cumulative methane production, showing the contributions from superemitters (red) and non-superemitters (dark green). Super-emitters dominate the overall MLR, accounting for approximately 75% of total emissions. The dramatic spike at the highest percentiles (approaching 100% of cumulative production) reveals extreme methane intensities reaching up to 25% in the most emissions-intensive fields, primarily driven by superemitter contributions.

7 US CI and MRL results

Analysis of 2,252 natural gas fields across 19 US basins reveals substantial regional variation in both carbon intensity (CI) and methane loss rate (MLR) (Figure 43). Significant regional heterogeneity is evident, with CI ranging from 5.4 to 250 g CO_2eq./MJ and MLR varying between 0.71% and 7.7% at the field level. Notably, shale gas basins in the Appalachian region (Marcellus, Utica, and broader Appalachian) exhibit consistently lower emissions intensities. Conversely, conventional basins predominantly located in the western U.S. display higher and more variable emissions profiles.

At the basin-level, production-weighted average CI demonstrates a threefold variation, ranging from 7.4 g CO_2eq./MJ in the Denver-Julesburg Basin to 22 g CO_2eq./MJ in minor conventional basins classified collectively as *Other* (Table 26). The three largest shale gas basins (Marcellus, Haynesville, and Appalachian) show notably divergent emissions profiles despite comparable geological contexts. The Marcellus and Appalachian basins maintain relatively low CI values of 9.1 and 8.5 g CO_2eq./MJ, respectively, whereas the Haynesville basin exhibits higher CI (14 g CO_2eq./MJ), largely due to increased methane emissions and intensive processing. Conventional basins consistently report higher CI values, including Powder River (21 g CO_2eq./MJ), Piceance (15 g CO_2eq./MJ), and San Juan (13 g CO_2eq./MJ). Remarkably, the Woodford Basin presents extreme field-level variability, with some fields surpassing 2,000 g CO_2eq./MJ due to elevated acid gas concentrations, though its production-weighted average remains at 12 g CO_2eq./MJ.

Methane loss rates exhibit a similar basin-level pattern, with production-weighted MLR ranging from 1.2% to 2.4%. Unconventional shale basins consistently achieve the lowest methane loss rates, notably Denver-Julesburg (1.2%), Niobrara (1.3%), and Marcellus (1.4%). The Haynesville basin demonstrates a higher MLR (2.2%) compared to other shale basins, attributable to elevated superemitter occurrences in Louisiana. Conventional basins have the highest methane loss rates, notably Powder River (2.4%), Uinta (2.1%), and San Juan (2.1%). Relative uncertainty in MLR estimates spans 48% to 100%.

Table 26: **Production-weighted emissions metrics for major US natural gas basins.** Values show carbon intensity and methane loss rate with 95% confidence intervals based on methane emissions uncertainty.

Basin	**Fields**	**Carbon Intensity (g CO_2eq./MJ)**		**Methane Loss Rate (%)**	
		Average	**Range**	**Average**	**Range**
Marcellus	84	9.1	6.6-12	1.4	0.91-1.9
Appalachian	102	8.5	6.0-11	1.6	1.0-2.2
Utica	59	8.7	6.5-12	1.4	0.97-2.0
Eagle Ford	66	9.5	6.8-12	1.4	0.85-2.0
Haynesville	86	14	9.2-19	2.2	1.4-3.2
Permian	131	11	7.5-15	1.7	1.0-2.6
Bakken	19	10	7.6-13	1.7	0.97-2.3
San Juan	13	13	10-16	2.1	1.5-2.7
Uinta	9	13	9.5-16	2.1	1.5-2.8
Powder River	14	21	16-26	2.4	1.6-3.3
Denver-Julesburg	1	7.4	5.4-10	1.2	0.71-1.9

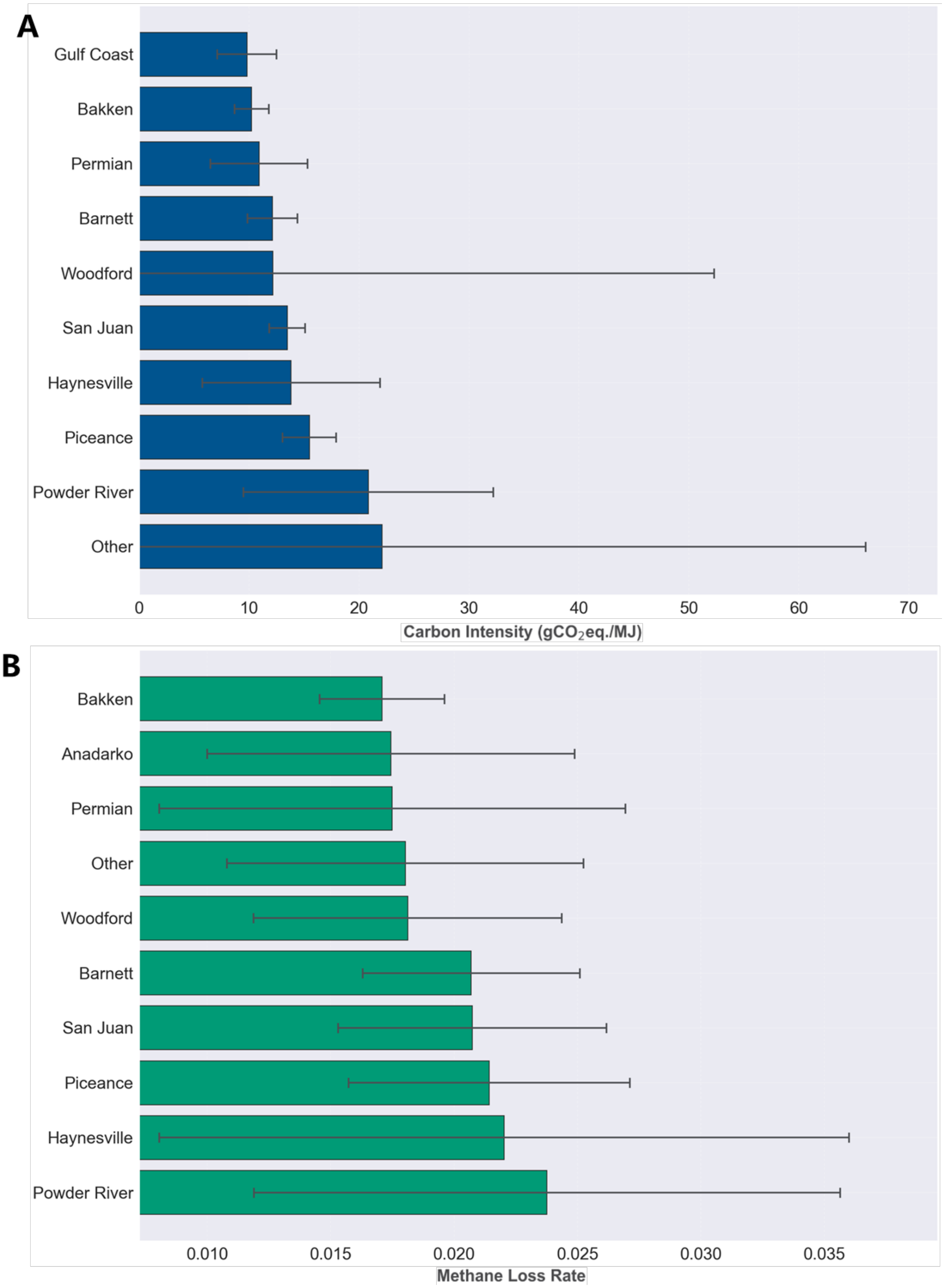

Figure 43: **Basin-level carbon intensity and methane loss rate for US natural gas production (2022). (A)** Production-weighted carbon intensity (g CO$_2$eq./MJ) and **(B)** methane loss rate (%). Bars represent basin-level production-weighted averages, with error bars showing the range of field-level values within each basin. The "Other" category aggregates basins containing fewer than 10 fields. Data encompasses 2,252 fields across 19 basins.

8 Terminal-level results

8.1 Terminal-level CI

Export terminals exhibit significant CI variations within countries, as illustrated in Figure 44. Algeria's terminals differ by 12.7 g CO_2eq./MJ (range: 9.2-21.9 g CO_2eq./MJ), while Russia's four facilities span 9.0 g CO_2eq./MJ (range: 8.4-17.4 g CO_2eq./MJ). The United States shows a large intra-country variation, with a 17.7 g CO_2eq./MJ spread across seven terminals (range: 8.2-25.9 g CO_2eq./MJ). Australia demonstrates the largest variation with a 18.8 g CO_2eq./MJ range (8.1-26.9 g CO_2eq./MJ) across its twelve terminals.

Import terminals display similarly distinct CI patterns (Figure 45). Japan's 31 terminals span 10.2 g CO_2eq./MJ (range: 12.1-22.3 g CO_2eq./MJ), while China's 21 terminals exhibit the largest variation of 13.1 g CO_2eq./MJ (range: 11.8-24.9 g CO_2eq./MJ). European countries reveal varying CI distributions: Italy's three terminals span 15.1 g CO_2eq./MJ (range: 12.7-27.8 g CO_2eq./MJ), France's four terminals differ by 8.1 g CO_2eq./MJ (range: 19.6-27.7 g CO_2eq./MJ), and Spain's six terminals show a more uniform 3.7 g CO_2eq./MJ difference (range: 20.7-24.4 g CO_2eq./MJ).

8.2 Terminal-level methane loss rate

Export terminals demonstrate varied MLR within countries (Figure 46). Algeria's terminals show a difference of about 2.1%, ranging from 0.86% to 2.96%. The United States has consistent performance across terminals, with intensities ranging from 0.83% to 3.25%. Malaysia's terminals display the highest variation, with intensities spanning from 2.51% to 5.74%. Australia maintains relatively uniform performance across its twelve terminals, with methane intensities ranging from 0.64% to 4.23%, though most remain below 2%. Nigeria stands out with the highest MLR among all export terminals at 11.85%-20.45%.

Import terminals reveal distinct MLR patterns (Figure 47). Japan, with 31 terminals, shows performance ranging from 0.68% to 5.74%, with most terminals below 3%. China's 21 terminals demonstrate a similar range from 0.95% to 5.74%, though several terminals exceed 3%. European facilities present varying results: Spain's six terminals range from 2.05% to 9.44%, France's terminals span from 0.90% to 4.19%, and Italy's terminals range from 0.91% to 3.26%. India

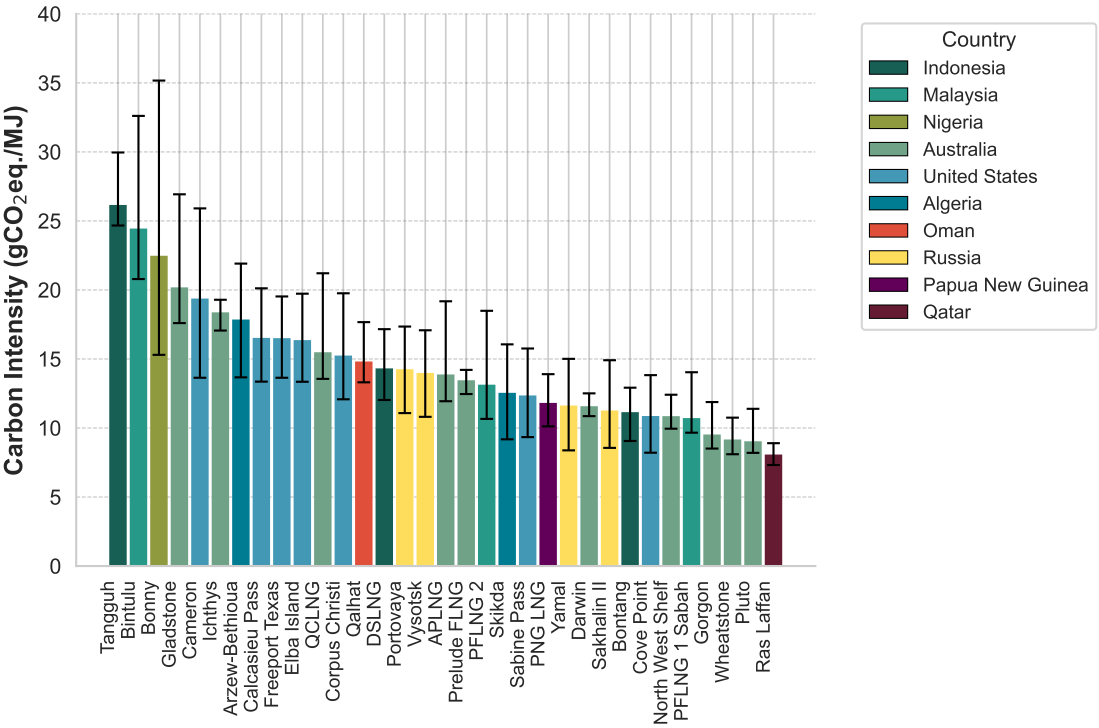

Figure 44: **Carbon intensity across LNG export terminals.** Values shown by country. The United States shows a wide range (8.2-25.9 g CO_2eq./MJ) across its seven terminals. Australia spans from 8.1-26.9 g CO_2eq./MJ across twelve terminals. Algeria ranges from 9.2-21.9 g CO_2eq./MJ, while Russia spans 8.4-17.4 g CO_2eq./MJ.

shows notable variation across its terminals, with intensities ranging from 1.09% to 9.19%, with Mundra having the highest value.

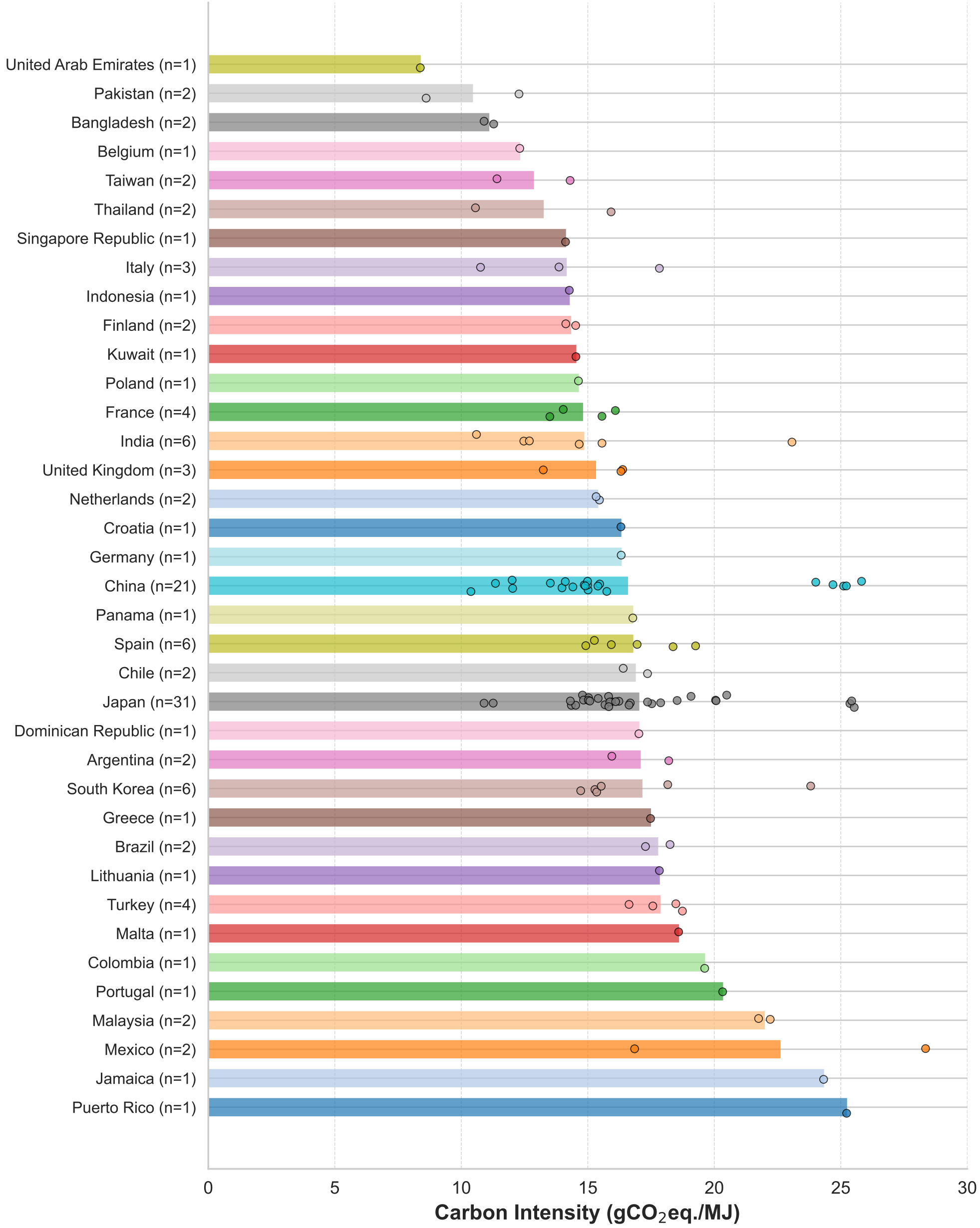

Figure 45: **Carbon intensity at LNG import terminals.** Colored horizontal bars represent country-level average CI, while dots show individual terminal-level CI values. Numbers in parentheses indicate the count of terminals per country. Significant variation exists within countries: China shows wide terminal variation (9.6-34.0 g CO$_2$eq./MJ) across 21 terminals; Japan spans from 9.9-33.7 g CO$_2$eq./MJ across 31 terminals. European countries show varying ranges: Italy (9.7-22.2 g CO$_2$eq./MJ), France (10.1-20.2 g CO$_2$eq./MJ), and Spain (11.2-26.8 g CO$_2$eq./MJ). Countries are sorted by average CI, with the United Arab Emirates showing the lowest average CI (8.4 g CO$_2$eq./MJ) and Puerto Rico the highest (26.8 g CO$_2$eq./MJ).

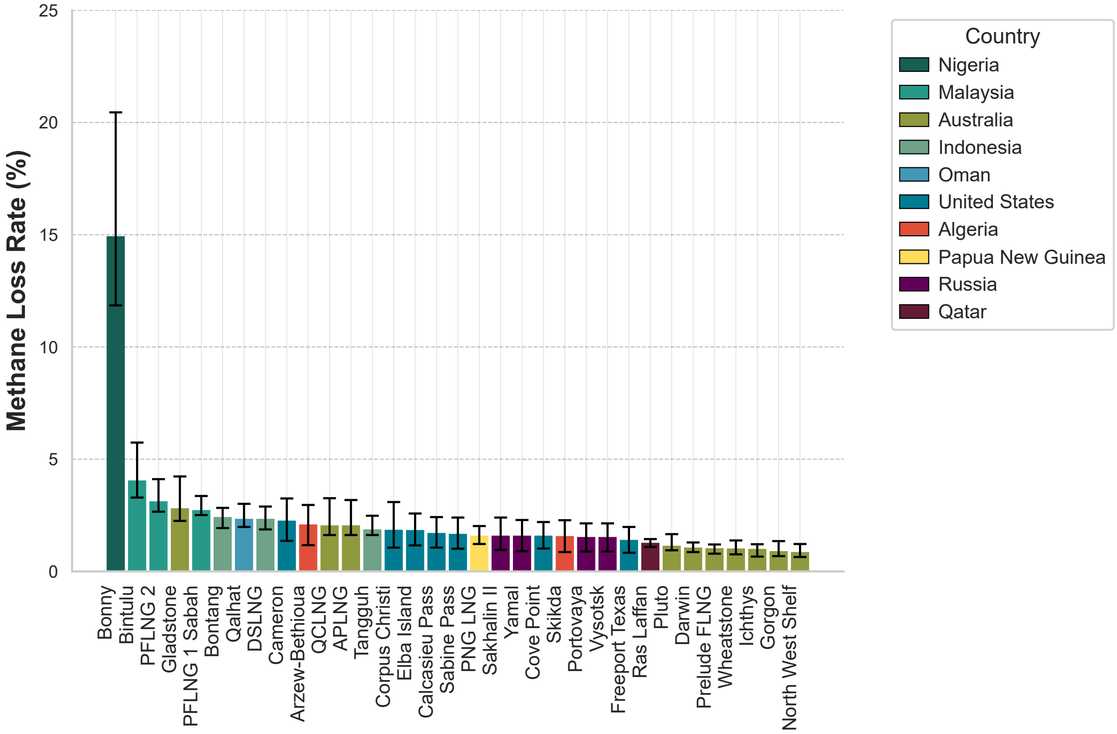

Figure 46: **Methane loss rate across LNG export terminals.** Values are shown by country. Malaysia shows the highest single-terminal intensity at 5.74%. Australia demonstrates mostly consistent performance below 2% across twelve terminals, ranging from 0.64% to 4.23%. The United States maintains a moderate variation between 0.83-3.25%. Nigeria has the highest overall intensity at 11.85-20.45%.

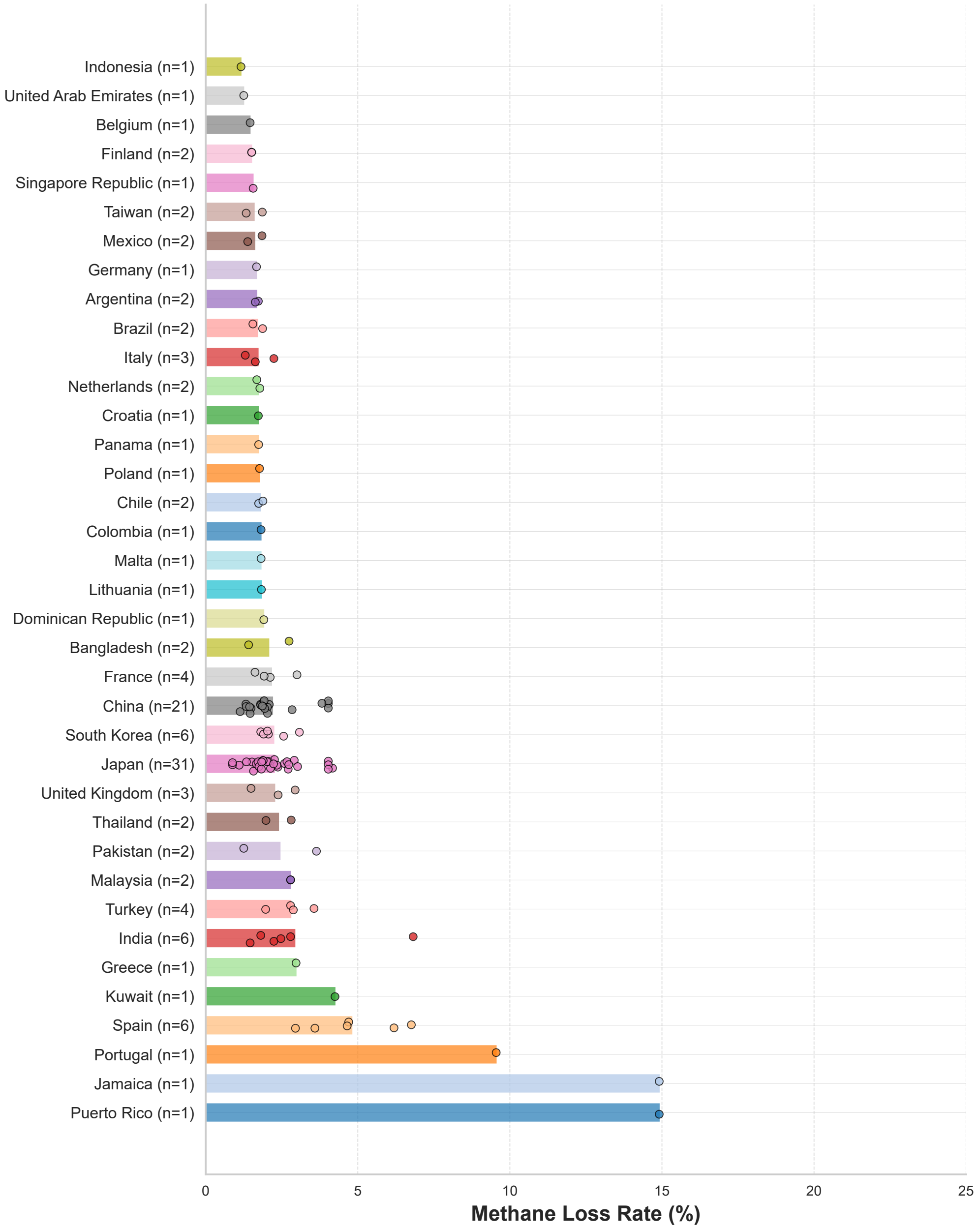

Figure 47: **Methane loss rate at LNG import terminals.** Japan shows performance ranging from 0.68% to 5.74% across 31 terminals. China demonstrates a similar range from 0.95% to 5.74% across 21 terminals. European countries display varying patterns: Spain (2.05-9.44%), France (0.90-4.19%), and Italy (0.91-3.26%).

9 Methane emissions breakdown

As shown in Figure 48, produced natural gas consists mainly of methane (CH_4), with small amounts of carbon dioxide (CO_2) and volatile organic compounds (VOCs). This study in Section 2.3 shows that methane makes up 98% of leaked gas in most LNG exporters, except Nigeria, where it is 94% with VOCs contributing 6%. For simplicity, we express all gas leak quantities in methane-equivalent terms throughout this study.

Super-emitters contribute approximately 75% of total methane emissions, with non-superemitter emissions accounting for 25% (Figure 49). Super-emitter contributions vary significantly across LNG exporting countries. Oman exhibits the highest superemitter fraction at 87.0%, followed by Nigeria (81.9%) and Russia (80.6%), demonstrating particularly concentrated emission sources in these nations. Countries with relatively higher non-superemitter contributions include Qatar (32.8%), Papua New Guinea (32.5%), and Indonesia (32.4%).

At the field level, methane emissions contribute differently to CI across the global LNG supply (Figure 50). About 80% of fields show relatively low methane emissions CI (< 10 g CO_2eq./MJ), mainly from non-superemitter emissions. However, the remaining 20% of fields exhibit substantially higher intensities, reaching up to 50 g CO_2eq./MJ, largely due to superemitters.

9.1 Non-superemitters

Emissions from non-superemitters are calculated using the component-level fugitives model described in Section 3.1. Figure 51 shows the country-level breakdown of these emissions. Gas gathering contributes the largest portion of CI at approximately 1.0 g CO_2eq./MJ. However, emission sources vary significantly by country. For example, Nigeria has the highest contribution from flaring (≈ 1.0 g CO_2eq./MJ), while the United States and Russia have substantial emissions from artificial lift operations. At the field level, Figure 52 reveals that high CI fields are dominated by three main sources: artificial lift, separation, and oil and condensate storage. While gas gathering, modeled using a site-level approach, shows relatively consistent contributions across fields, other process emissions vary more widely. This variation suggests that field-specific operational characteristics significantly influence non-superemitter emissions.

Table 27: **Component counts for oil fields equipment.** This table presents the range of component counts (minimum – maximum) found in the data.

Equipment	TC	Valve	OEL	PEV	CS	Regulator	PC	CIP	TH	Others
Well	61–298	7–23	2–3	1–4	0	0	0	0	0	0
Heater	30–56	3–19	1	1	0	0	0	0	0	0
Separator	62–87	11–28	2–2	1	0	0	0	0	0	0
Meter	14–39	1–3	2–2	1	0	0	0	0	0	0
Tank - Leaks	6–21	2–6	1	0	0	1	0	0	0	0
Tank - Vents	0	0	0	0	0	0	0	0	1	1
Compressor - Reciprocating	52–56	7–9	0	0	0	0	0	0	0	0
Dehydrator	22–27	2–6	0	1	0	0	0	0	0	0
Chemical Injection Pump	0	0	0	0	0	0	0	1	0	0
Pneumatic Controller	0	0	0	0	0	0	1	0	0	0

Table 28: **Component counts for gas fields equipment.** This table presents the range of component counts (minimum – maximum) found in the data.

Equipment	TC	Valve	OEL	PRV	CS	Regulator	PC	CIP	TH	Others
Well	69–298	12–23	1–3	1–4	1	1	0	0	0	0
Header	100–520	16–143	1–5	1	0	1	0	0	0	0
Heater	20–156	2–30	1–3	1	0	2–4	0	0	0	0
Separator	62–180	20–29	1–5	1–2	1	3–3	0	0	0	0
Meter	39–100	3–19	1–2	1–2	0	2–2	0	0	0	0
Tank - Leaks	3–76	15	1–3	1	1	1	0	0	0	0
Tank - Vents	0	0	0	0	0	0	0	0	1	1
Compressor - Reciprocating	117–586	18–35	1–5	1–4	1–4	1–6	0	0	0	0
Dehydrator	27–217	6–29	1–5	1–3	1	6–6	0	0	0	0
Chemical Injection Pump	0	0	0	0	0	0	0	1	0	0
Pneumatic Controller	0	0	0	0	0	0	1	0	0	0

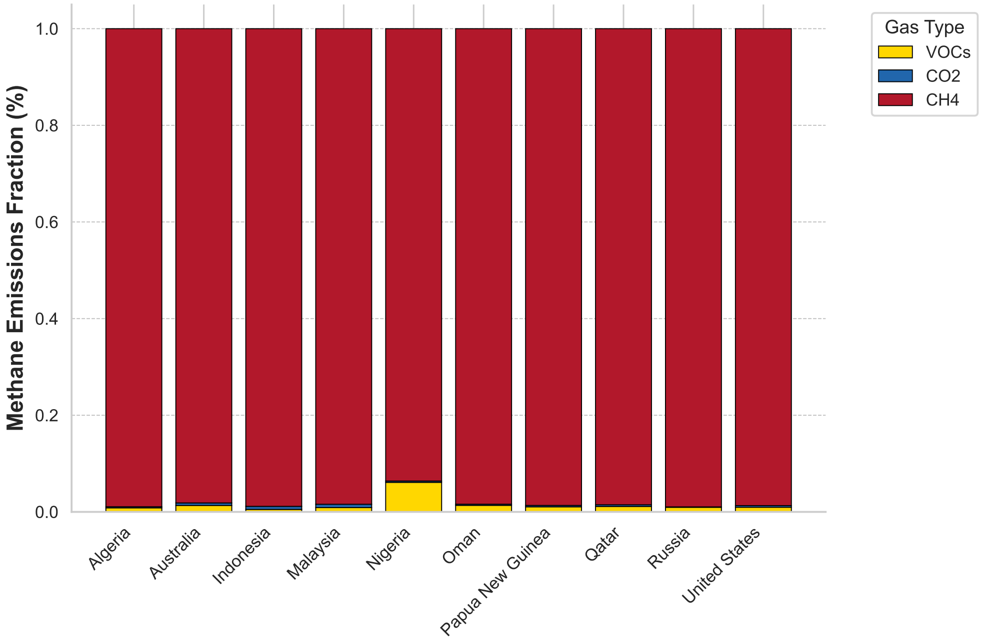

Figure 48: **Gas composition of leaks from LNG operations.** Stacked bars show the components of leaked gas for each country. Methane (CH_4, red) is the main component, making up 98% of leaks in most countries. Nigeria shows a different pattern with 94% methane and 6% volatile organic compounds (VOCs, yellow). CO_2 (blue) levels are very low across all countries.

9.2 Methane emissions uncertainty

Methane emissions constitute the dominant source of carbon intensity in the LNG value chain, accounting for approximately 51% of total importer CI. All uncertainty ranges in this study represent methane emissions uncertainty and are reported as 95% confidence intervals. The uncertainty analysis focuses on two components: superemitter emissions ($\geq$ 100 kg CH_4/hour) and non-superemitter emissions (< 100 kg CH_4/hour), as these represent the primary sources of variability. Other emission sources (production, processing, liquefaction, shipping, and regasification) are treated as deterministic values based on established engineering calculations.

After integrating superemitter data (Section 3.2) with the updated component-level fugitives model (Section 3.1), we analyze the uncertainty in methane emissions across the global LNG supply chain, expressed in both CI and MLR metrics. Our uncertainty analysis reveals distinct patterns between different emission sources. For methane CI (Figure 53), the uncertainty ranges remain relatively narrow for most of the production spectrum, widening significantly only for the highest-emitting fields. Super-emitter contributions show a stepped distribution pattern, with

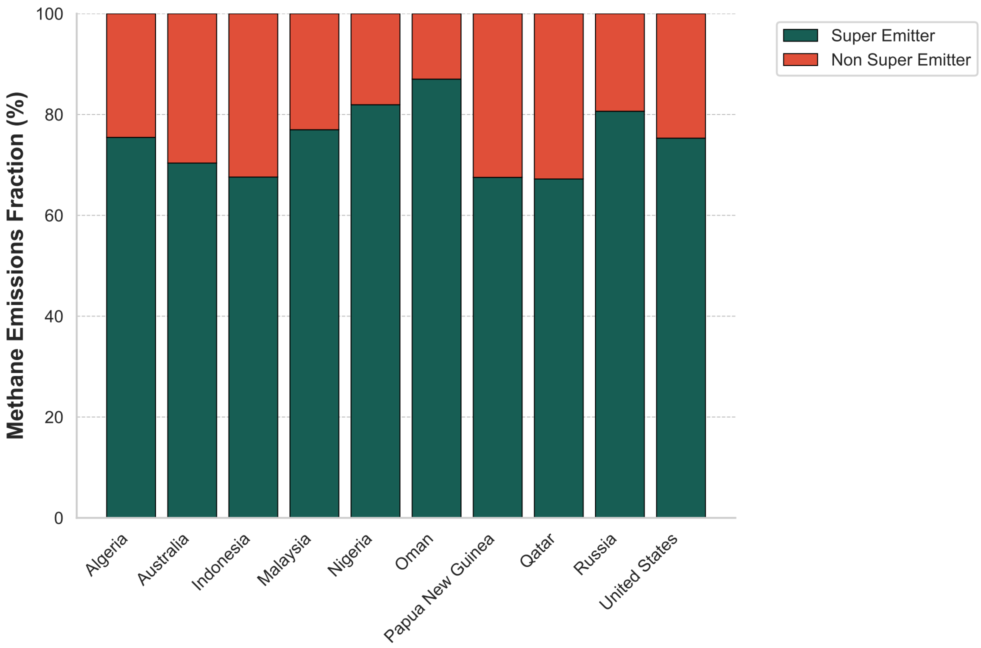

Figure 49: **Methane emissions breakdown by country and source type.** Stacked bars show the relative contributions of superemitters (green) and non-superemitters (red) to total methane emissions for each LNG exporter. Super-emitters constitute the majority of methane emissions across all countries, with contributions ranging from 67.2% (Qatar) to 87.0% (Oman). Countries with the highest superemitter fractions include Oman (87.0%), Nigeria (81.9%), and Russia (80.6%), while those with relatively higher non-superemitter contributions include Qatar (32.8%), Papua New Guinea (32.5%), and Indonesia (32.4%).

most fields having relatively low CI values (below 10 g CO_2eq./MJ) and a sharp increase for the highest-CI fields (reaching up to 30 g CO_2eq./MJ). In contrast, non-superemitter emissions show a more gradual increase across fields, with uncertainty ranges that widen as CI increases. When examining MLR as a percentage of production (Figure 54), we observe that most fields maintain low methane emissions rates. Fields producing approximately 80% of total gas show intensities below 2.5%, with relatively constrained uncertainty ranges. The remaining high-intensity fields represent a small fraction of production but exhibit substantially wider uncertainty ranges, particularly among superemitters.

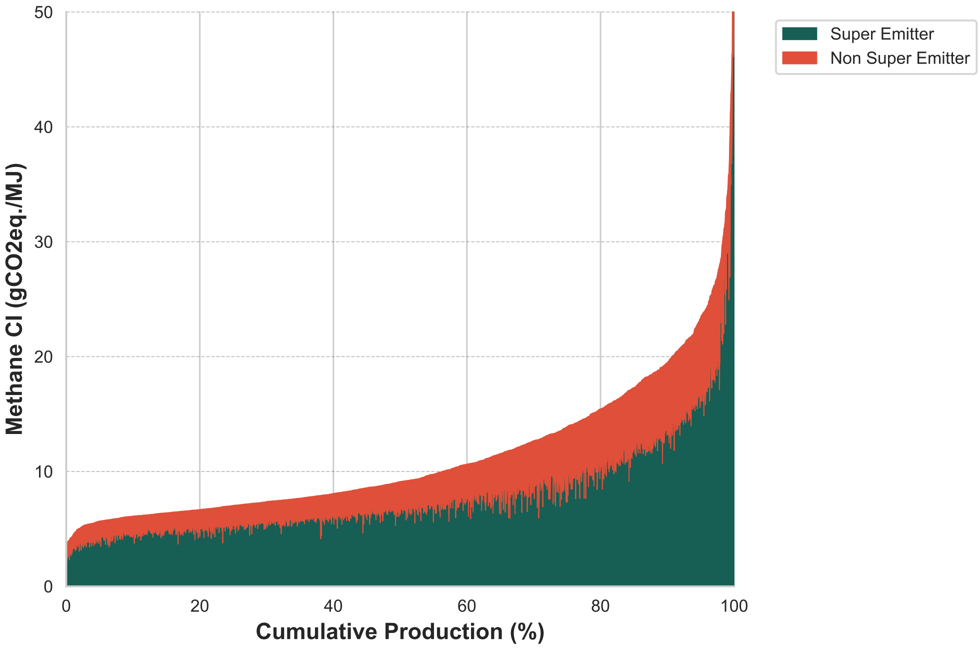

Figure 50: **Field-level methane emissions CI distribution.** Stacked area chart showing the contribution of superemitters (green) and non-superemitters (red) to methane CI (g CO_2eq./MJ) across cumulative production. Fields are ranked by increasing methane CI. Super-emitters constitute the majority of methane emissions across the production spectrum, with their proportion generally increasing in higher-intensity fields. Approximately 60% of production exhibits relatively low methane intensities (<10 g CO_2eq./MJ), while the highest-emitting 10% of production shows a sharp exponential increase. fields.

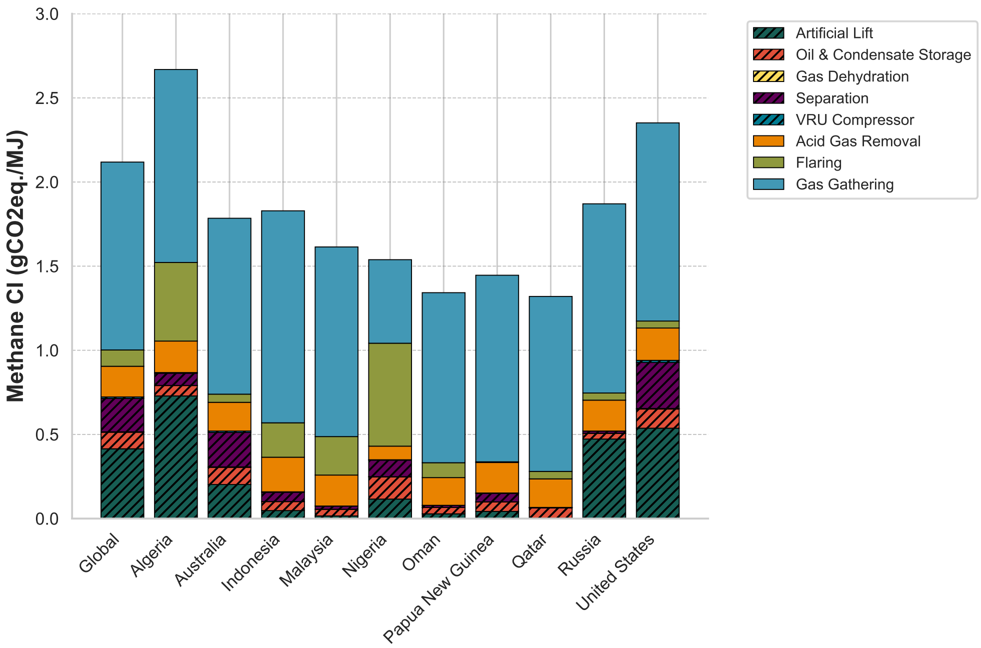

Figure 51: **Country-level non-superemitter emissions by source.** Stacked bars show process-specific contributions to CI for each LNG exporter. Gas gathering dominates global emissions, but source distributions vary significantly by country, with flaring prominent in Nigeria and artificial lift in the US and Russia. Other key contributors include separation, storage, and pneumatic devices, with their relative importance varying by country.

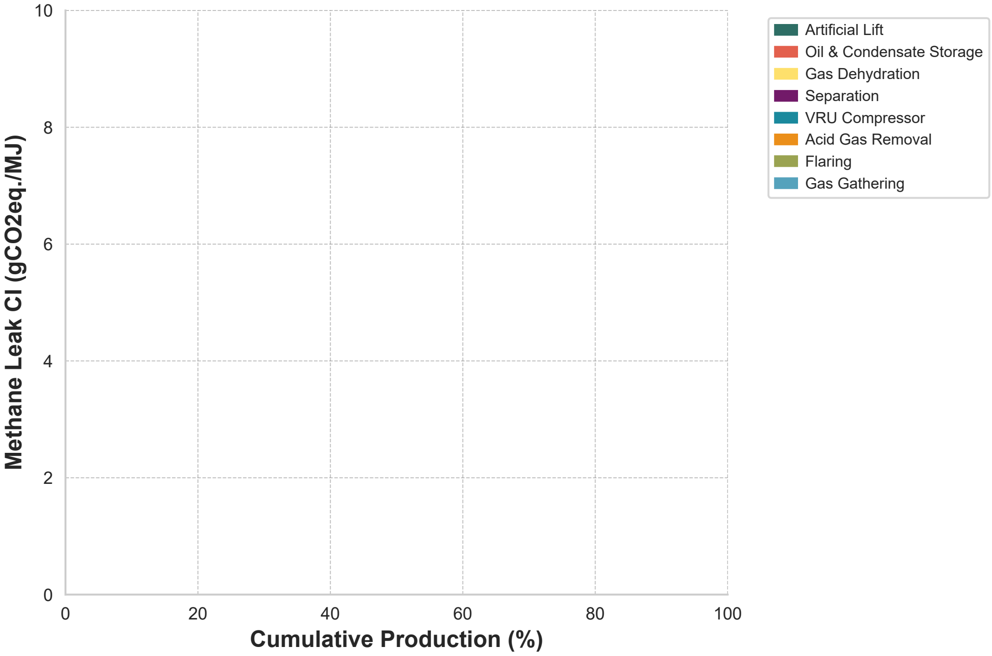

Figure 52: **Field-level distribution of non-superemitter emissions.** Cumulative distribution shows CI contributions from different processes across fields, ordered by increasing methane CI. The x-axis represents cumulative production percentage, while the y-axis shows CI in g CO_2eq./MJ. Fields with higher CI (right side of graph) show larger contributions from artificial lift, separation, and storage operations, while gas gathering contributions remain high across all fields.

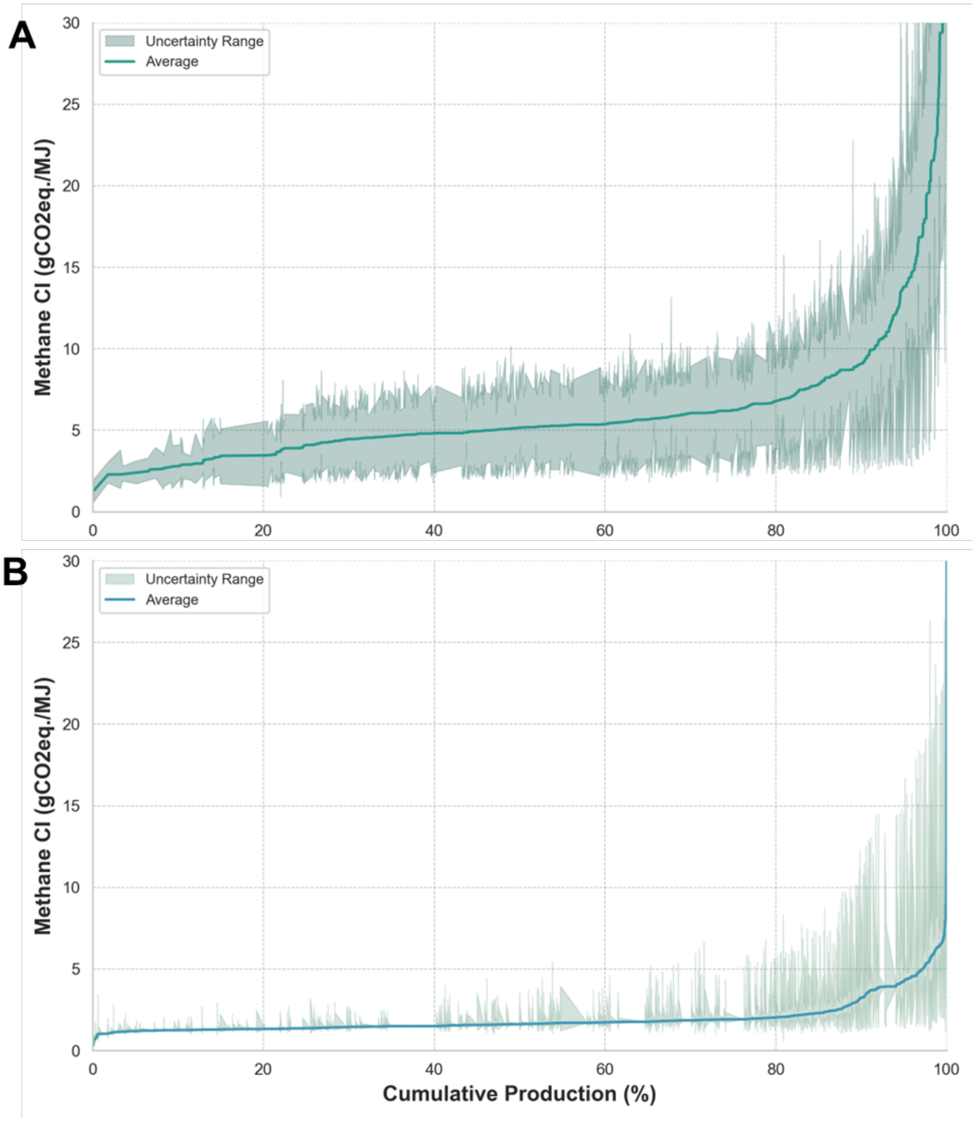

Figure 53: **Methane CI uncertainty.** The figure shows methane CI distributions with uncertainty ranges. (**A**) Super-emitter CI (green line) show distinct steps with relatively narrow uncertainty ranges except for the highest-CI fields. (**B**) Non-superemitter CI (blue line) increase more gradually with consistently wider uncertainty ranges toward higher values. Fields are ranked from lowest to highest CI and plotted against cumulative production percentage. Shaded areas show 95% confidence intervals.

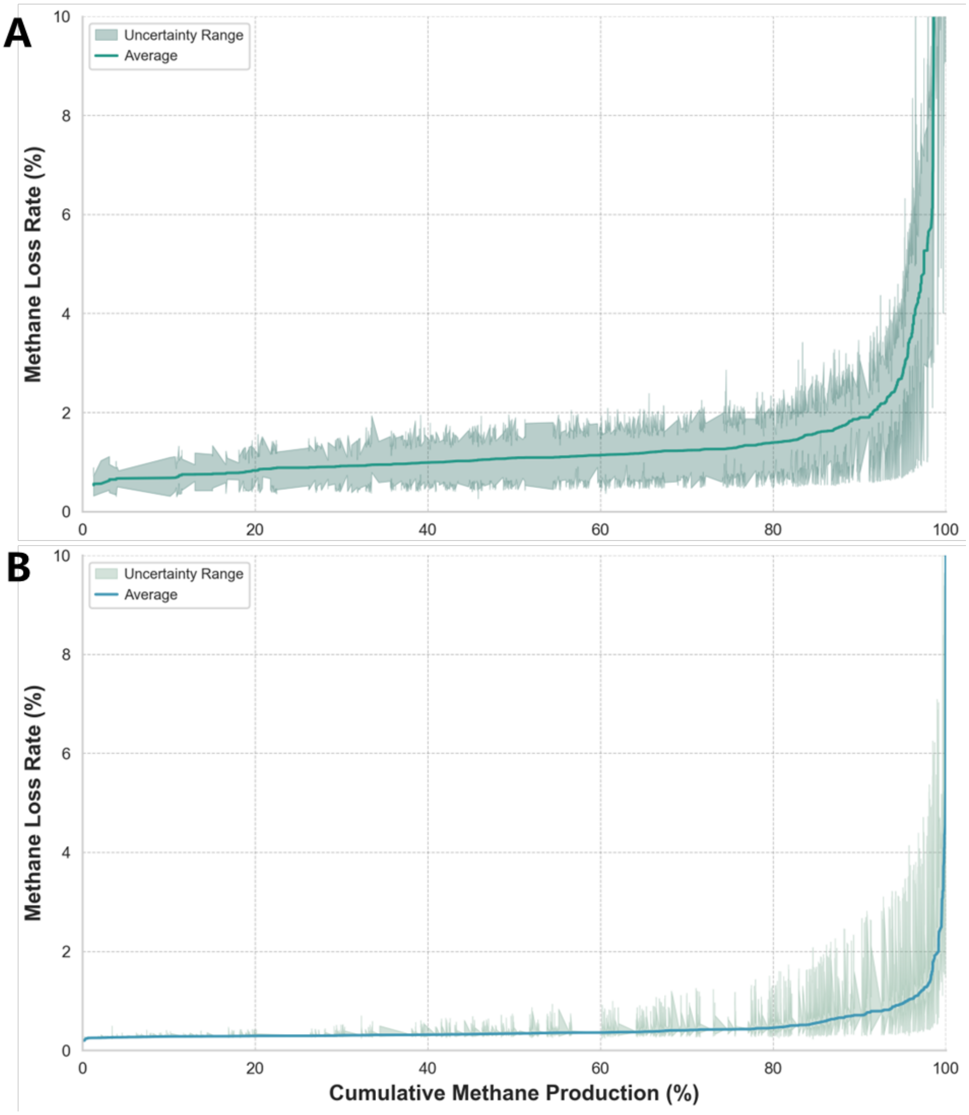

Figure 54: **Methane loss rate uncertainty.** The figure displays MLR (emissions as percentage of production) with uncertainty ranges. (**A**) Super-emitter intensity (green line) shows most production comes from fields with intensities below 2.5%, with uncertainty expanding for high-intensity fields. (**B**) Non-superemitter intensity (blue line) exhibits a more uniform distribution with more constrained uncertainty ranges. Fields are ranked by intensity and plotted against cumulative methane production percentage. Shaded regions show 95% confidence intervals.

10 Surface processing emissions breakdown

Surface processing includes three main operations: acid gas removal (AGR), gas dehydration, and demethanization. In fields where acid gas is captured rather than vented, we account for additional CO_2 compression energy requirements and associated emissions. All processing emissions calculations utilize proxy models developed by Masnadi et al. (*16*).

Figure 55 illustrates the distribution of surface processing emissions by country. AGR operations and CO_2 venting collectively contribute over 80% of global surface processing emissions. CO_2 venting practices vary significantly across countries, with six major producers venting more than 50% of their CO_2: Indonesia, Malaysia, Algeria, Nigeria, Oman, and Papua New Guinea. Qatar exhibits more moderate venting at approximately 10%. Gas dehydration and demethanizer operations contribute comparatively smaller amounts to the overall emissions profile.

At the field level (Figure 56), the majority of operations generate less than 2.5 g CO_2eq./MJ from processing activities. However, a limited number of fields produce substantially higher emissions, reaching up to 20 g CO_2eq./MJ. These elevated emissions primarily result from CO_2 venting in fields processing gas with high acid gas content, highlighting how geological characteristics can significantly impact the CI of natural gas processing.

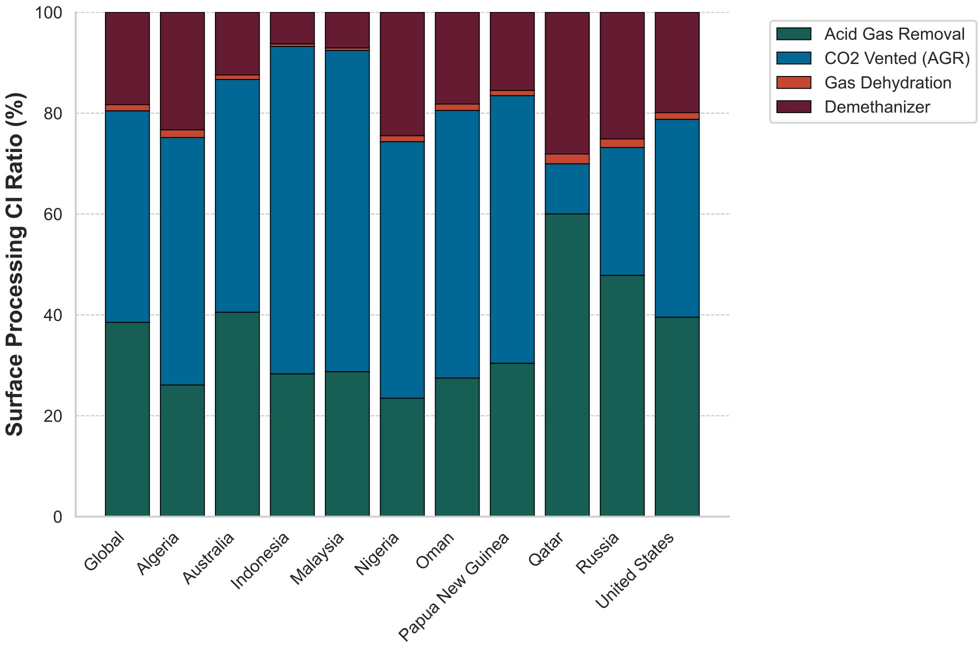

Figure 55: **Surface processing emissions by country and source.** Stacked bars display emissions contributions from each processing operation. AGR (green) and CO_2 venting (blue) constitute the majority of emissions across countries. Six countries (Indonesia, Malaysia, Algeria, Nigeria, Oman, and Papua New Guinea) vent over 50% of their CO_2, while Qatar shows moderate venting levels around 10%. Gas dehydration (red) and demethanizer operations (purple) make smaller contributions to the overall emissions profile.

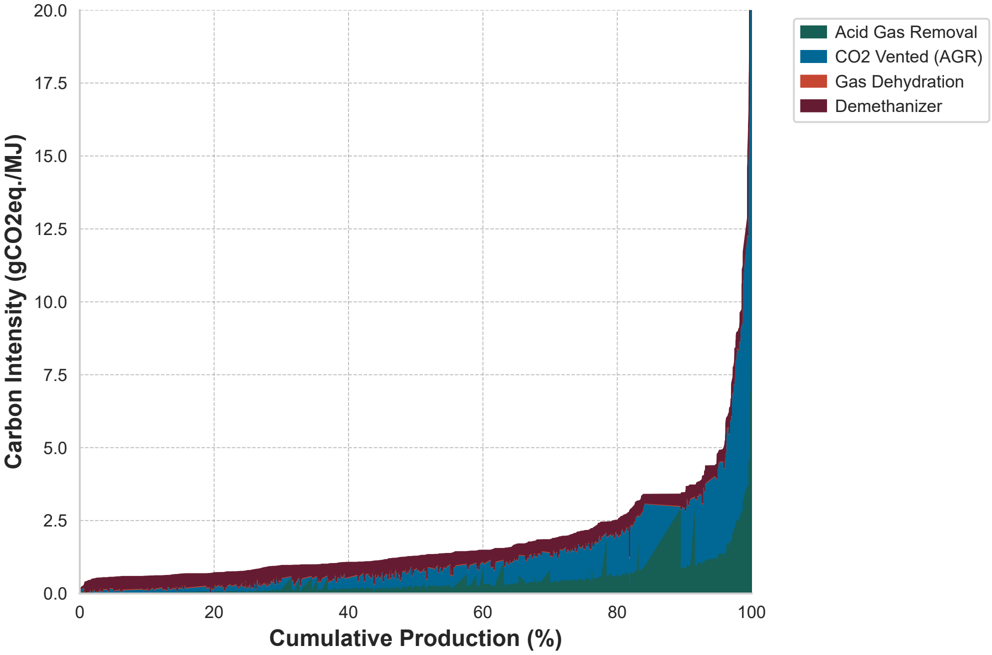

Figure 56: **Field-level surface processing emissions breakdown.** The graph shows fields ranked by CI plotted against cumulative energy output. Most fields maintain processing emissions below 2.5 g CO_2eq./MJ. The relatively few high-emission fields (exceeding 10 g CO_2eq./MJ) primarily show elevated emissions from CO_2 venting (blue), while gas dehydration (red) and demethanizer operations (purple) contribute consistently lower emissions across all fields.

11 Shipping emissions breakdown by engine types

Shipping emissions vary significantly based on the propulsion system employed. This study examines six types of marine engines used in LNG carriers: Steam Turbine; Low-Pressure Two-Stroke Engine (XDF); M-Type Electronically Controlled Gas Injection (MEGI); Dual-Fuel Diesel Electric and Tri-Fuel Diesel Electric (DFDE/TFDE); Slow-Speed Diesel (SSD); and Steam Turbine and Gas Engine (STaGE). Table 29 presents the distribution of engine types across the analyzed fleet, excluding trades below 1,000 tons which typically represent carrier cool-down operations. SSD engines are particularly significant for Qatar's operations, representing 41% of voyages and 50% of cargo (Table 30).

Table 29: **Engine breakdown for top ten LNG exporters for cargos exceeding 1,000 tons, excluding multi-stop trades.** The table shows vessel count, cargo volume, and mileage distribution across different engine types.

Engine Type	Vessel Count	Cargo (tons)	Mileage (nm)	Vessel (%)	Cargo (%)	Mileage (%)
DFDE	522	34,455,541	2,362,088	10.3	10.2	10.1
ME-GI	480	34,116,369	2,810,064	9.5	10.1	12.0
SSD	496	42,711,709	2,430,227	9.8	12.7	10.4
STaGE	47	3,409,834	405,791	0.9	1.0	1.7
Steam	2,170	128,989,632	7,811,997	42.8	38.2	33.3
TFDE	784	54,818,890	4,145,319	15.5	16.2	17.7
X-DF	568	39,053,028	3,512,568	11.2	11.6	15.0
Total	5,067	337,555,003	23,478,054	100.0	100.0	100.0

Our model incorporates vessel-specific data rather than using fixed assumptions. We use actual cargo quantities instead of the standard 98% capacity assumption. Each vessel's specific boil-off rate replaces the traditional 0.0008% daily rate for ballast voyages. The analysis excludes multi-stop trades (Table 31). This study shows distinct patterns in emissions across different engine types. Each engine type shows a unique relationship between shipping distance and CI. Steam turbine engines dominate the global fleet, representing 43% of total voyages (2,107 vessels). These vessels show emissions ranging from 0.015 to 0.314 g CO_2eq./g LNG. The distances covered vary from 265 to 16,348 miles. The average vessel capacity is 139,000 m^3.

Other engine types demonstrate varied market presence and performance characteristics. TFDE/DFDE propulsion systems account for 1,279 voyages (26% of total), while MEGI represents 474 voyages

Table 30: **SSD and STaGE engine distribution by country in 2022.** This table presents the detailed breakdown of SSD and STaGE engine types, showing vessel counts, cargo volumes, and trade percentages.

Engine Type	Country	Vessel Count	Cargo (tons)	Mileage (nm)	Total Export (tons)	Total Mileage	Trade (%)	Cargo (%)
SSD	Qatar	428	38,920,073	2,202,524	80,207,070	4,676,850	40.0	48.5
	Papua New Guinea	25	1,913,793	94,294	8,715,611	504,156	21.0	22.0
	Australia	22	1,589,051	79,196	77,943,209	5,011,998	2.0	2.0
	Malaysia	10	84,150	22,610	27,981,143	1,220,306	1.8	0.3
	Russian Federation	8	66,800	12,379	32,629,315	1,956,072	1.3	0.2
	United States	2	129,300	16,761	75,942,397	9,174,723	0.2	0.2
	Indonesia	1	8,542	2,463	11,679,547	698,863	0.5	0.1
STaGE	United States	34	2,406,162	321,723	75,942,397	9,174,723	2.8	3.2
	Oman	8	605,401	47,143	11,560,601	1,079,960	4.3	5.2
	Australia	4	316,209	28,670	77,943,209	5,011,998	0.3	0.4
	Papua New Guinea	1	82,062	8,255	8,715,611	504,156	0.8	0.9
Total		543	46,121,543	2,836,018				

(10% of total). XDF engines are used in 565 voyages (11% of total), and SSD propulsion powers 479 voyages (10% of total). Each engine type exhibits different emissions characteristics. XDF engines show the strongest correlation between distance and emissions ($R^2 = 0.8994$). SSD vessels demonstrate the most consistent emissions pattern, with limited variability despite changing distances. The linear relationships between distance and emissions suggest systematic differences in engine efficiency and fuel consumption patterns.

Table 31: **Percentage of multi-stop trades for top ten LNG exporters for cargos exceeding 1,000 tons.** Countries are ranked by their contribution of multi-stop trades to total trade volume.

Country	Single Trade (tons)	Multi-Stop Trade (tons)	Total Trade (tons)	Multi-Stop (%)
United States	69,056,283	6,886,114	75,942,397	8.59
Australia	75,503,575	2,439,634	77,943,209	3.04
Qatar	78,985,428	1,221,642	80,207,070	1.52
Indonesia	11,001,388	678,159	11,679,547	0.85
Russian Federation	31,964,932	664,383	32,629,315	0.83
Nigeria	14,156,921	420,584	14,577,505	0.52
Papua New Guinea	8,345,422	370,189	8,715,611	0.46
Malaysia	27,631,495	349,648	27,981,143	0.44
Oman	11,219,539	341,062	11,560,601	0.43
Algeria	10,114,096	32,277	10,146,373	0.04
Total	337,979,079	13,403,692	351,382,771	

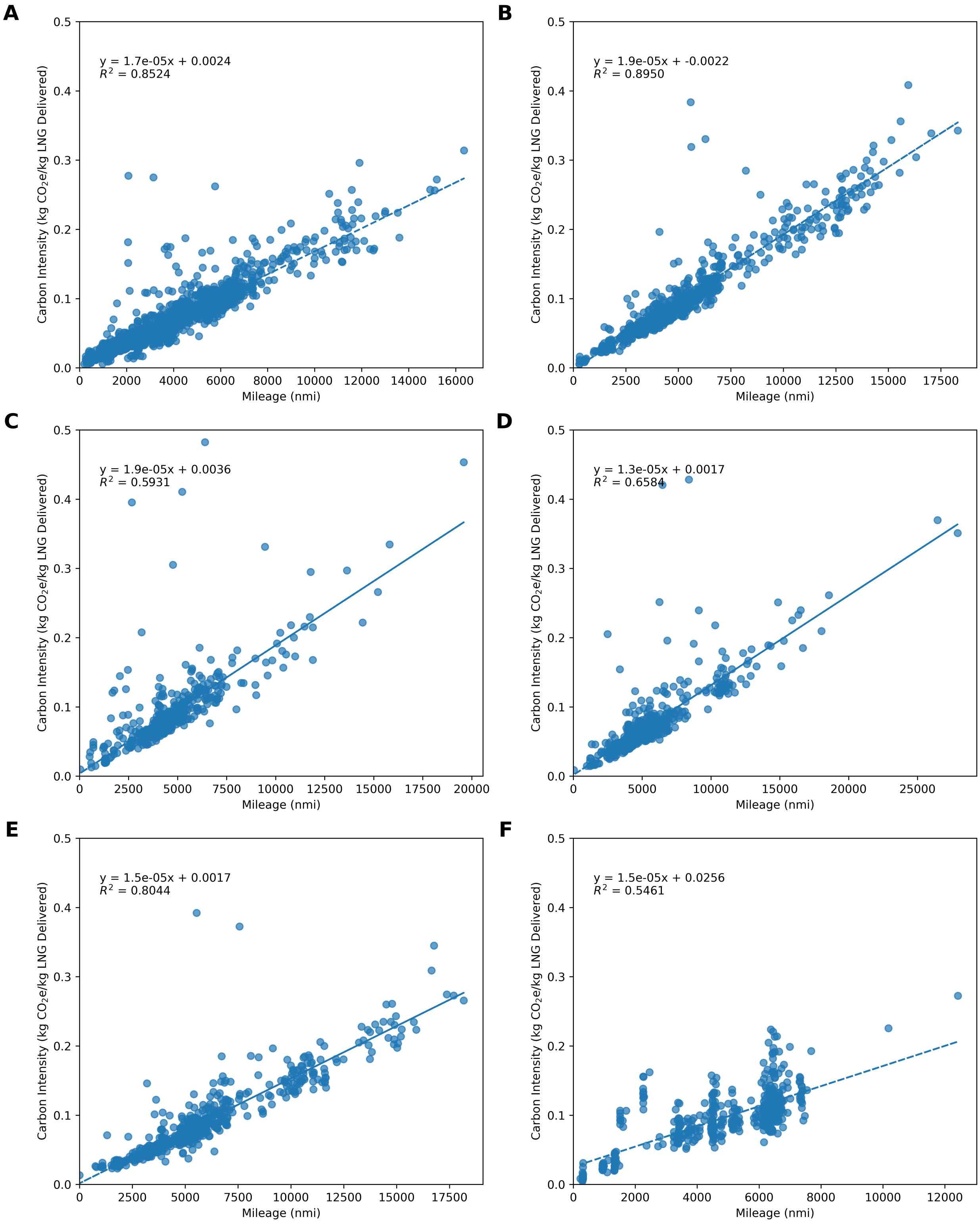

Figure 57: **Carbon intensity varies systematically with distance for different engine types.** Carbon intensity (CI) as a function of shipping distance for six liquefied natural gas (LNG) engine technologies: (A) Steam turbine (R^2 = 0.85), (B) Tri-fuel diesel electric (TFDE; R^2 = 0.90), (C) Dual-fuel diesel electric (DFDE; R^2 = 0.59), (D) M-type, electronically controlled gas injection (MEGI; R^2 = 0.66), (E) X-dual fuel (XDF; R^2 = 0.80), and (F) Slow-speed diesel (SSD; R^2 = 0.55). All values in g CO_2-equivalent per g LNG.

12 Regasification emissions breakdown

LNG regasification CI varies significantly across terminals and regions (Figure 58). Among major terminals, India's Dahej shows the highest CI (0.34 g CO_2eq./MJ), while Chinese facilities cluster between 0.20–0.25 g CO_2eq./MJ. Japanese terminals exhibit moderate values, and European facilities (Dunkerque, Zeebrugge) consistently demonstrate lower emissions ($\approx$0.10 g CO_2eq./MJ).

Regional analysis reveals systematic patterns. The Asia-Pacific region displays the widest CI range in large-scale facilities (0.15–0.34 g CO_2eq./MJ), reflecting diverse electricity grid emissions factors. European terminals maintain lower emissions across all scales due to cleaner electricity grids. Middle Eastern facilities show relatively consistent emissions ($\approx$0.15 g CO_2eq./MJ), while North American terminals demonstrate moderate variability in medium-scale operations. South American facilities generally maintain comparatively low CI values.

Total emissions by country (Figure 59) show China leading large-scale facility emissions ($\approx$600 kt CO_2eq. annually), followed by other Asian nations (India, Japan, South Korea). European countries, despite numerous terminals, exhibit substantially lower total emissions (<200 kt CO_2eq. annually per country). This pattern persists across all terminal scales, with medium-scale facilities emitting <60 kt CO_2eq. annually and small-scale terminals generally <2 kt CO_2eq. annually. These variations primarily reflect differences in regional electricity grid emissions factors, operational efficiencies, and scale-specific technologies.

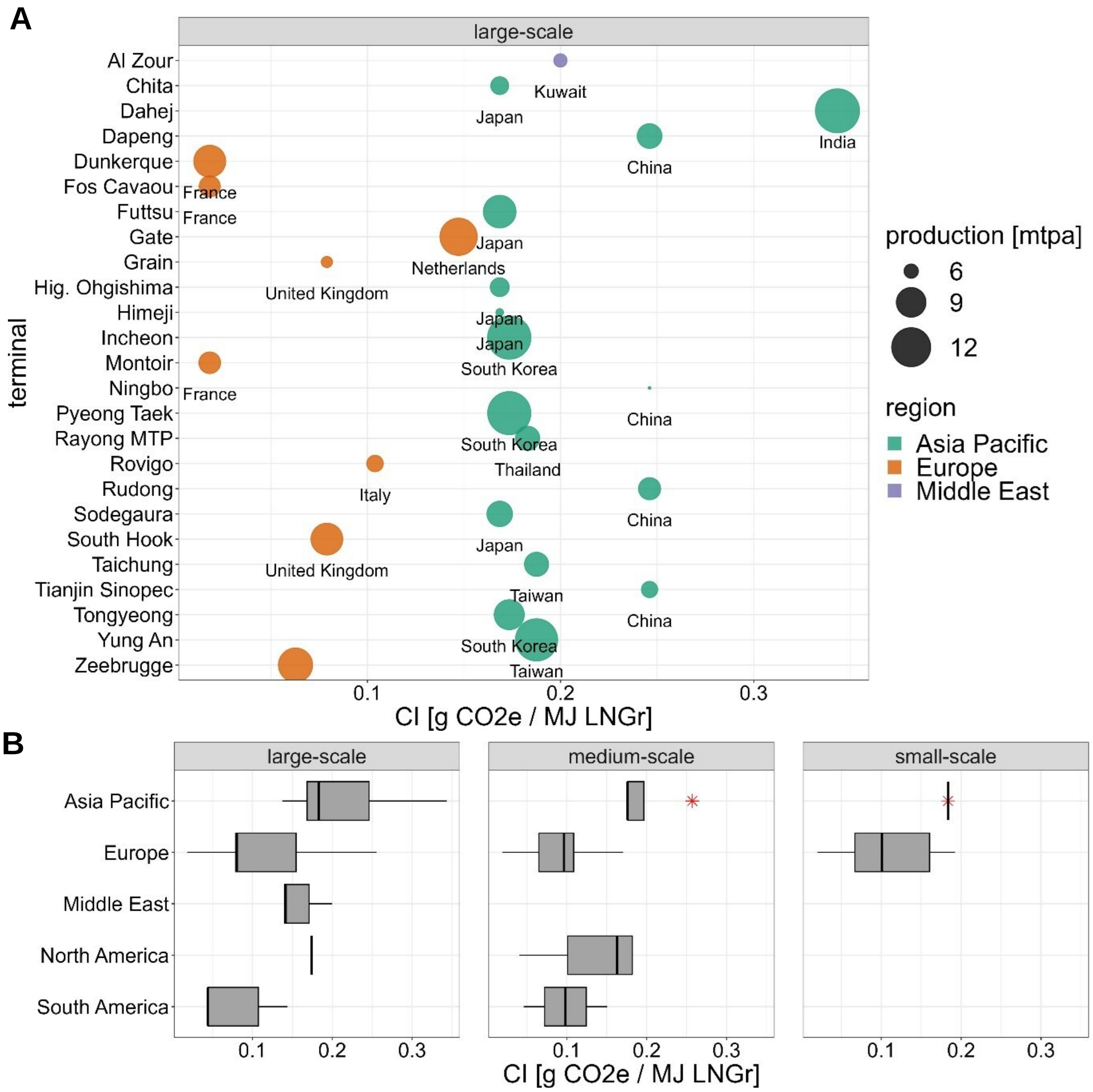

Figure 58: **Carbon intensity distribution across major LNG regasification terminals and regions.** (A) Individual terminal CI for the top 25 terminals by production capacity. Circle sizes represent production capacity in MTPA. Colors indicate regions: Asia Pacific (green), Europe (orange), and Middle East (purple). (B) Box plots showing CI distributions by region and terminal scale. Boxes indicate 25th-75th percentiles, with whiskers extending to minimum and maximum values excluding outliers. Red asterisks indicate statistical outliers.

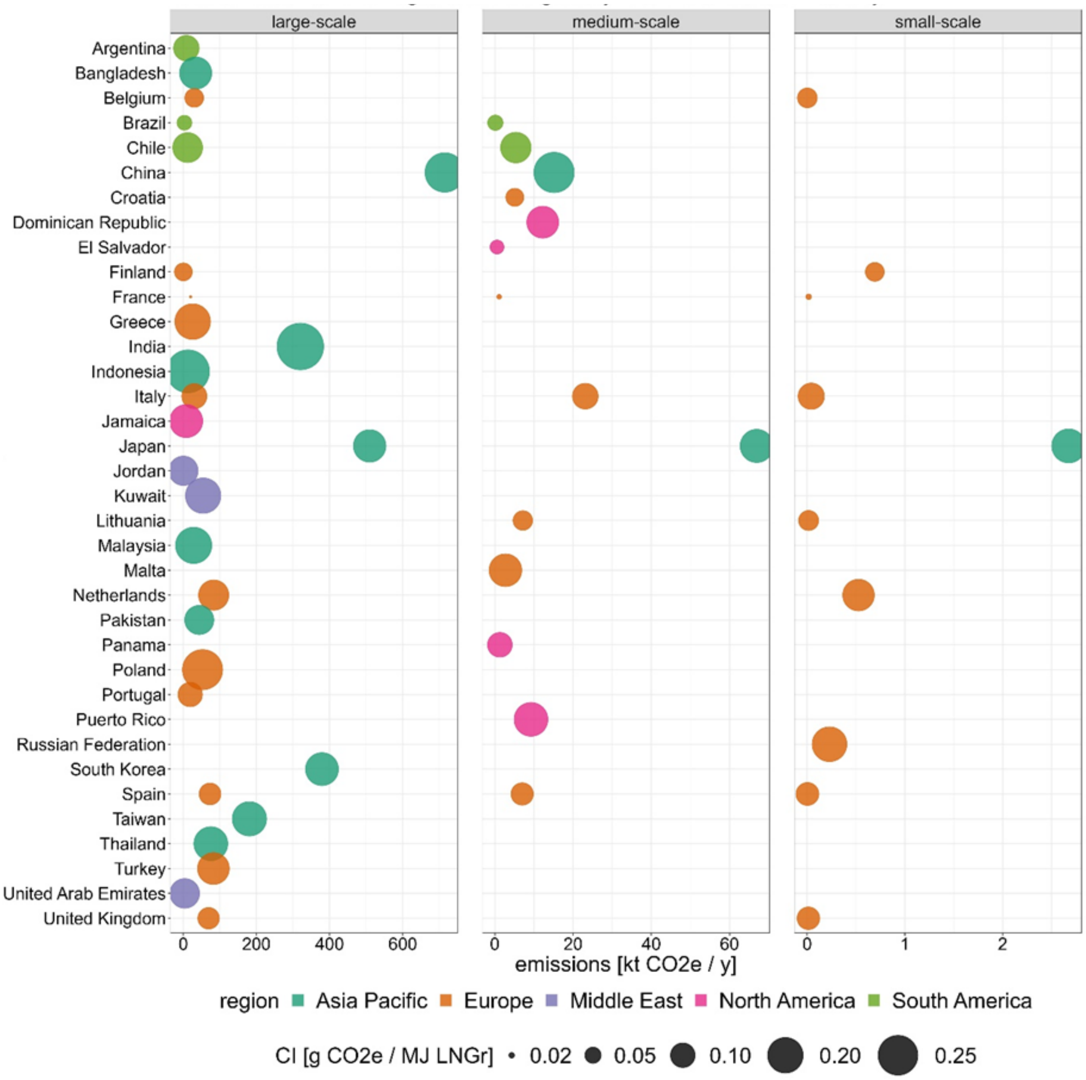

Figure 59: **Total emissions from global LNG regasification terminals.** Emissions shown by country and terminal scale (large: ≥3 MTPA, medium: 0.45–3 MTPA, small: ≤0.45 MTPA). Circle sizes represent CI (0.02–0.25 g CO_2eq./MJ LNG). Colors indicate regions: Asia Pacific (green), Europe (orange), Middle East (purple), North America (pink), and South America (light green). China shows the highest emissions in large-scale facilities, while European countries demonstrate lower emissions across all scales.

13 Scenario analysis

13.1 Capture acid gas

Figure 60 shows the impact of implementing 100% CO_2 capture at these facilities. This strategy reduces upstream CI from 11.13 to 10.24 g CO_2eq./MJ, an 8.7% decrease. The reduction represents approximately 59 million tonnes of CO_2 captured per year. The reduction appears primarily in surface processing emissions (yellow), while other sources remain unchanged. At the terminal level, the implementation of acid gas capture shows varying degrees of effectiveness across different regions. As illustrated in Figure 61, terminals in Indonesia experience the most substantial reductions, with CI decreasing from approximately 26.1 g CO_2eq./MJ to 17.4 g CO_2eq./MJ at the Tangguh terminal (a reduction of about 8.7 g CO_2eq./MJ). Significant improvements are also observed in Malaysian terminals, where the Bintulu facility shows a CI drop from about 24.4 g CO_2eq./MJ to 20.0 g CO_2eq./MJ (a 4.4 g CO_2eq./MJ reduction). Several Australian terminals demonstrate substantial benefits as well, with Prelude FLNG experiencing a 4.1 g CO_2eq./MJ decrease, North West Shelf showing a 2.8 g CO_2eq./MJ reduction, and Gladstone decreasing by 2.6 g CO_2eq./MJ. These larger reductions likely reflect higher baseline acid gas content and processing requirements. In contrast, terminals in regions such as Qatar and some facilities in the United States show more modest improvements, typically ranging from 0.1 to 1.0 g CO_2eq./MJ reduction.

13.2 Methane loss rate mitigation target

In 2018, the Oil and Gas Climate Initiative (OGCI) set a 0.2% MLR target for upstream operations. This target was based on a 2017 global average baseline of 0.3% (*51*). We find a current global average MLR of 2.2% across the complete value chain. Given this broader scope, we analyze three reduction targets: 0.2%, 0.5%, and 1.0%. In this study, MLR is defined as the ratio of methane loss rate to processed methane production shown in Equation 54.

$$MLR = \frac{L}{P_{out}} = \frac{L}{P_{in} - L} \tag{54}$$

where MLR is MLR, L is methane loss rate (tonne per year), P_{out} is processed methane production rate (tonne per year), and P_{in} is wellhead methane production rate (tonne per year).

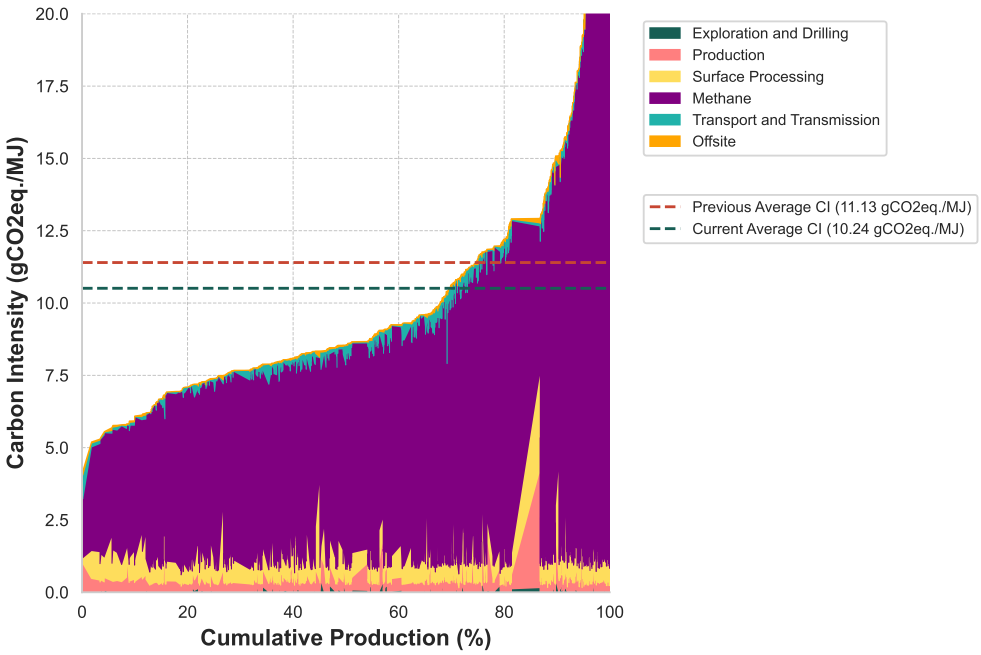

Figure 60: **Impact of acid gas capture on LNG fields upstream carbon intensity.** Fields ranked by CI versus cumulative energy output. Implementing 100% CO_2 capture reduces global upstream CI by 8.7%. Surface processing emissions (yellow) decrease significantly while other sources remain constant. Dashed lines show original (11.13 g CO_2eq./MJ) and new (10.24 g CO_2eq./MJ) global average CI.

Since total methane production depends mainly on reservoir conditions and production methods, we assume P_{in} varies by country but is independent of loss rates.

For each reduction scenario, we calculate future MLR (MLR_f) after reducing methane losses by fraction f, using current MLR (MLR_c):

$$MLR_f = \frac{(1-f)L}{P_{in} - (1-f)L} = \frac{(1-f)MLR_c}{1 + fMLR_c} \tag{55}$$

Figure 62 shows how MLR changes under different reduction scenarios for each LNG exporter. Each solid line represents a country's MLR trajectory, starting from its current value (shown in parentheses) and decreasing as emission reductions increase. Three horizontal dashed lines indicate potential MLR targets of 0.2%, 0.5%, and 1.0%. The reduction requirements vary significantly across countries. At the 0.2% target (bottom dashed line), Nigeria must reduce its emissions by 98.5% from its current 14.9% intensity. Malaysia and Oman need reductions of 94.7% and 91.2% respectively. Even countries with moderate intensities like the United States (1.6%) and

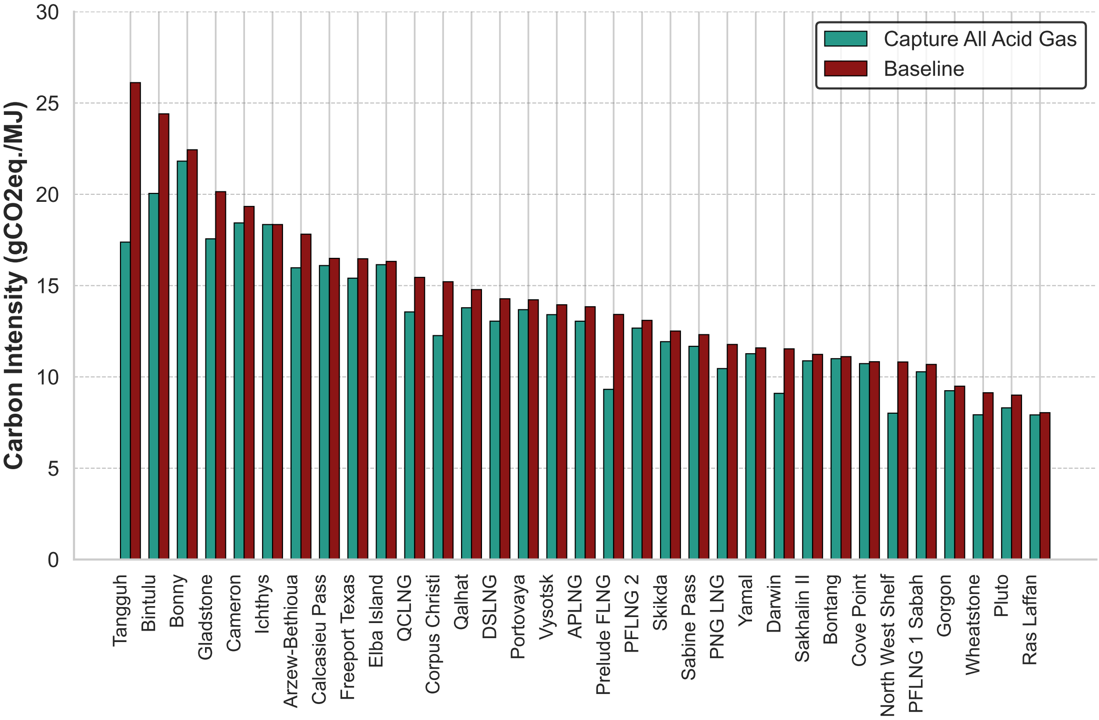

Figure 61: **Terminal-level carbon intensity changes after implementing acid gas capture.** Comparison of CI before and after implementing acid gas capture technology across global LNG terminals. Red bars show the previous CI values while teal bars represent CI after acid gas capture implementation. The greatest reductions are observed in terminals from Indonesia (Tangguh, ≈ 8.7 g CO_2eq./MJ decrease), Malaysia (Bintulu, ≈ 4.4 g CO_2eq./MJ decrease), and Australia (Prelude FLNG, ≈ 4.1 g CO_2eq./MJ decrease). Other terminals showing significant improvements include Australia's North West Shelf (≈ 2.8 g CO_2eq./MJ) and United States' Corpus Christi (≈ 2.9 g CO_2eq./MJ), while terminals in Qatar and some U.S. facilities show more modest improvements of 0.1-1.0 g CO_2eq./MJ.

Russia (1.6%) require substantial reductions of 87.4% and 87.0%. For the 0.5% target (middle dashed line), all countries need reductions, though less severe. Nigeria requires a 96.2% reduction, while Qatar needs only 59.6%. For the 1.0% target (top dashed line), all countries still require reductions, with Nigeria and Malaysia needing significant cuts of 92.4% and 73.9%. The steeper slopes for high-intensity countries (e.g., Nigeria, Malaysia) indicate that their MLR decreases more rapidly with each reduction percentage than low-intensity countries (e.g., Qatar, Australia). This relationship shows countries with higher current intensities have greater potential for absolute emission reductions.

Figure 63 shows how terminal CI would change under different MLR targets (0.2%, 0.5%, and 1.0%). The current terminal CI (shown in red bars) varies significantly, reaching up to 26.12 g

CO_2eq./MJ for terminals in Indonesia (Tangguh) and 24.41 g CO_2eq./MJ in Malaysia (Bintulu). Under the 1.0% MLR rule (orange bars), terminals would see moderate reductions in CI, particularly in high-emission facilities. The 0.5% target (green bars) would drive further reductions, bringing most terminals below 15 g CO_2eq./MJ. The most stringent 0.2% target (purple bars) would achieve the largest reductions, with most terminals reaching CI between 4-10 g CO_2eq./MJ. The dashed lines indicate the global average CI under each scenario: current (15 g CO_2eq./MJ), 1.0% rule (12 g CO_2eq./MJ), 0.5% rule (11 g CO_2eq./MJ), and 0.2% rule (9 g CO_2eq./MJ). Terminals in countries like Australia (Gorgon, Ichthys, North West Shelf) show smaller reductions due to their already low methane intensities, while terminals in Nigeria (Bonny), Malaysia (Bintulu), and Indonesia (Tangguh) demonstrate the largest potential for CI improvement under stricter methane rules.

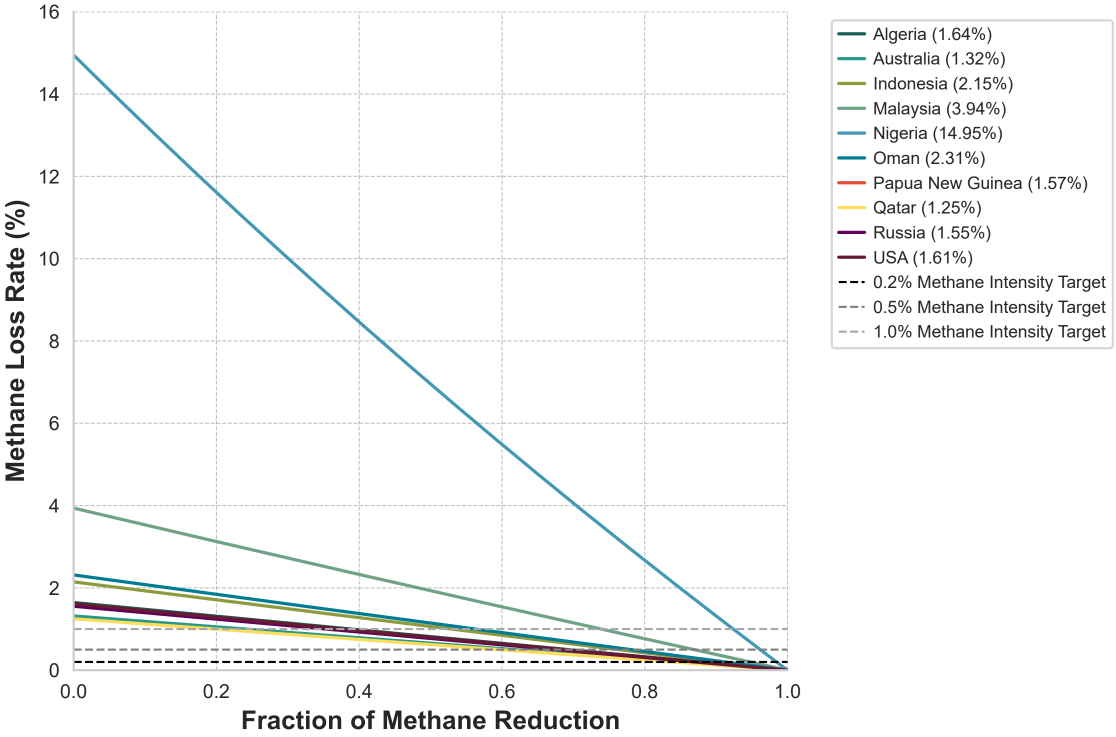

Figure 62: **Required methane reductions to meet market standards.** Lines show future methane intensities versus reduction fraction for each country. Starting intensities appear in parentheses. Dashed lines show potential MLR targets (0.2%, 0.5%, and 1.0%). Higher-intensity countries need larger reductions to meet these targets.

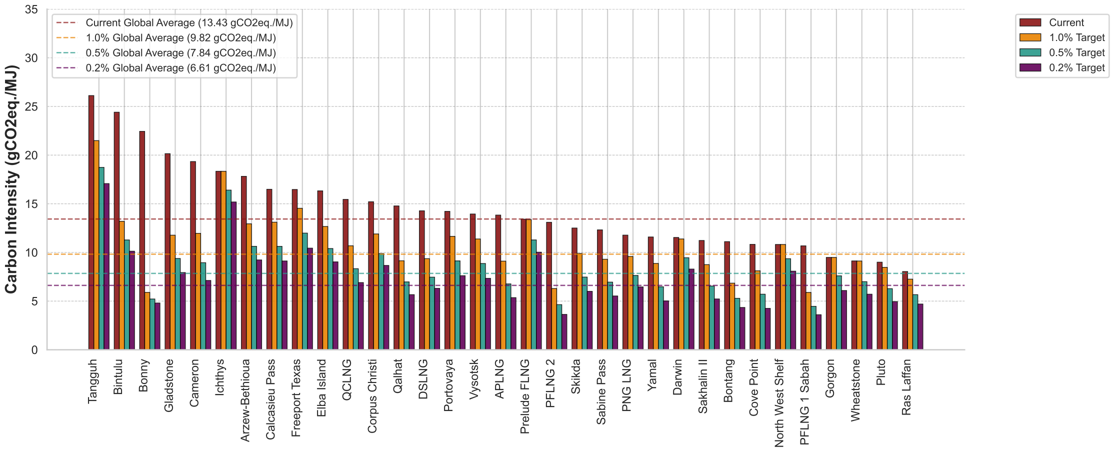

Figure 63: **Impact of methane loss rate rules on liquefaction terminal CI.** Red bars show the current CI of LNG terminals. Orange, green, and purple bars demonstrate potential CI under 1.0%, 0.5%, and 0.2% MLR rules, respectively. Dashed lines indicate the global average CI for each scenario. Higher-emission terminals, particularly in Indonesia (Tangguh), Malaysia (Bintulu), and Nigeria (Bonny), show the greatest reduction potential.

Table 32: **Methane loss rate reduction ratios across countries.** Required reduction fractions to achieve MLR targets of 0.2%, 0.5%, and 1.0%. Values show the fraction of methane that must be reduced.

Country	**0.2%**	**0.5%**	**1.0%**
Nigeria	0.985	0.962	0.924
Malaysia	0.947	0.869	0.739
Oman	0.912	0.780	0.562
Indonesia	0.905	0.763	0.529
Algeria	0.877	0.692	0.388
United States	0.874	0.687	0.377
Papua New Guinea	0.871	0.678	0.359
Russia	0.870	0.675	0.353
Australia	0.847	0.618	0.239
Qatar	0.838	0.596	0.197

13.3 Electrify the upstream compressor and pumps

We examined a scenario that replaces natural gas as the prime fuel in upstream operations (compressors, pumps, boilers, and other equipment) with electricity from the grid. Each process that originally burned on-site natural gas now consumes grid electricity. We also consider using zero emissions electricity (assuming 0 g CO_2eq./MJ and ignoring manufacturing or infrastructure emissions).

Figure 64 shows how emissions sources contribute to CI across the LNG value chain under different electrification scenarios. Methane emissions (purple) represent the largest contribution across most of the production spectrum, with surface processing (yellow) and production (red) also contributing significantly in some fields. The current global average CI (red dashed line) is 11.13 g CO_2eq./MJ. When upstream operations are electrified with grid electricity (dark green dashed line), the global average remains nearly unchanged at 11.27 g CO_2eq./MJ because grid emissions generally offset on-site reductions. Using renewable electricity (teal dashed line) reduces the average to 10.05 g CO_2eq./MJ, representing approximately a 10% reduction in overall CI.

Figure 65 compares terminal-level emissions under different electrification scenarios. Grid electrification of upstream operations (orange bars) produces varied outcomes depending on local grid CI. Some terminals show slight decreases in CI (Nigeria, Bonny, and PNG LNG), while others experience modest increases (terminals in Australia, Indonesia), reflecting differences in country-level grid emissions factors. Zero emissions electricity (green bars) consistently reduces emissions across all terminals, with an average reduction of about 1.1 g CO_2eq./MJ (approximately 8%). The global average decreases from 13.43 g CO_2eq./MJ in the current scenario to 13.60 g CO_2eq./MJ with grid electrification and 12.60 g CO_2eq./MJ with zero emissions electricity.

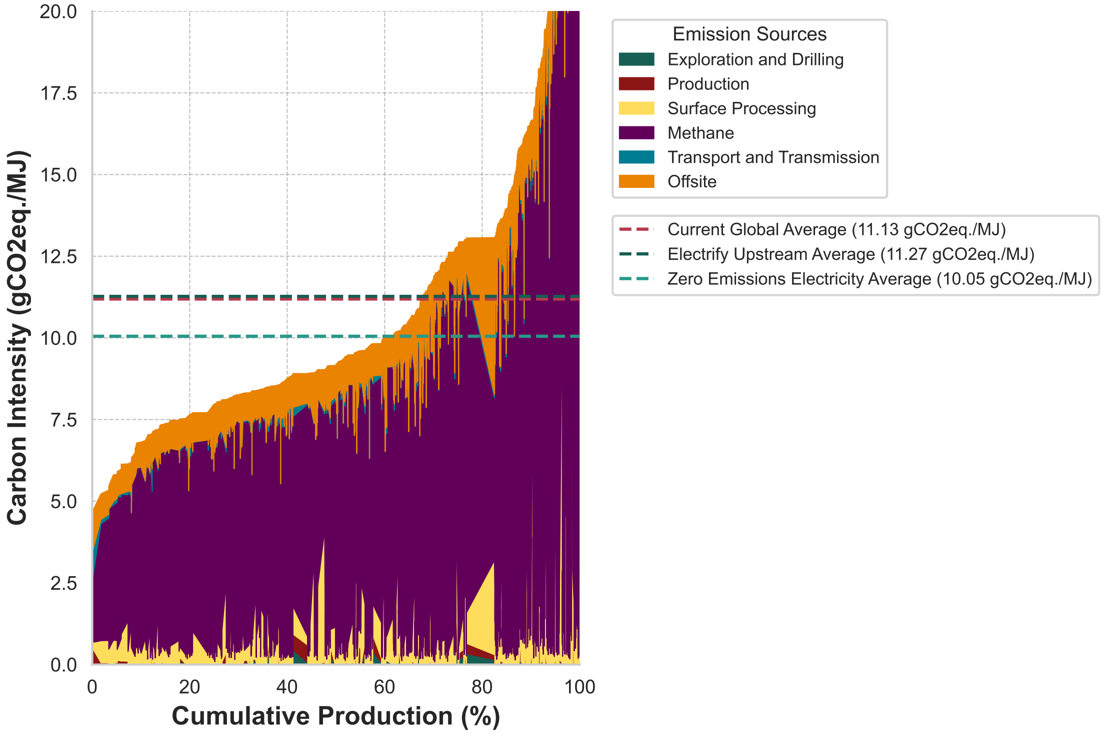

Figure 64: **Upstream CI under different electrification scenarios.** Fields are sorted by CI and plotted against cumulative energy content, with colored areas showing contributions from different emission sources. The red dashed line (11.13 g CO_2eq./MJ) is the current global average. The dark green dashed line (11.27 g CO_2eq./MJ) shows that relying on grid electricity for upstream operations slightly increases the average CI as grid emissions offset on-site natural gas combustion reductions. The teal dashed line (10.05 g CO_2eq./MJ) indicates the reduction achieved by using renewable electricity for upstream operations.

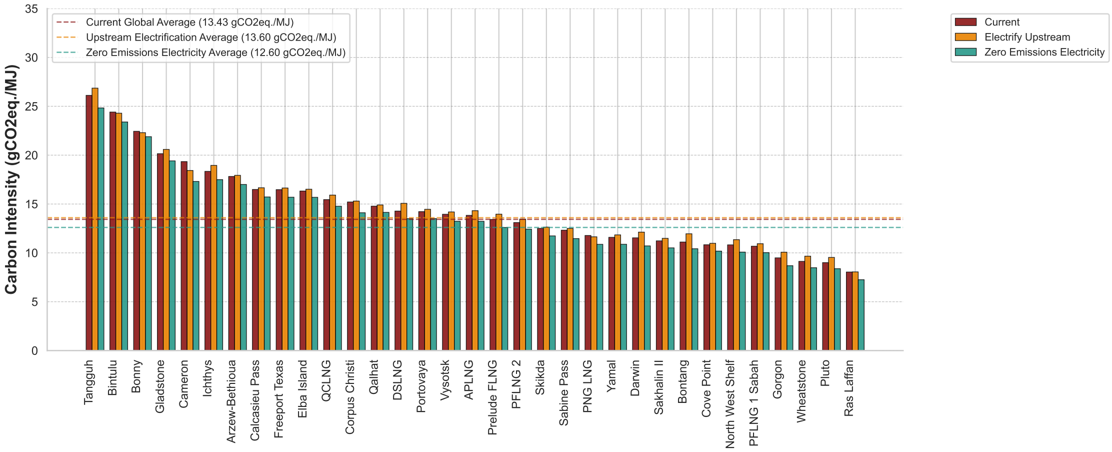

Figure 65: **Impact of upstream electrification on terminal carbon intensity.** Bars show terminal-level CI under three conditions: current operations (Current), upstream electrification with grid electricity (Electrify Upstream), and upstream electrification with renewable electricity (Zero Emissions Electricity). Dotted lines indicate global averages for each scenario: current (13.43 g CO_2eq./MJ), grid electrification (13.60 g CO_2eq./MJ), and renewable electricity (12.60 g CO_2eq./MJ).

14 Sensitivity analysis

This section examines how key variables affect field CI. To capture different operational patterns, we analyze three representative fields: an oilfield that produces associated gas, a rich gas field with high oil and condensate volumes, and a dry gas field with minimal liquid production.

For each field, we analyze sensitivity to acid gas (CO_2), sour gas (H_2S), and methane (CH_4) content. When varying one component's concentration, we adjust other components proportionally using Equation 56:

$$X_{i,new} = X_{i,base} \times \frac{100 - X_{target}}{100 - X_{target,base}} \tag{56}$$

where $X_{i,new}$ is the adjusted concentration of component i, $X_{i,base}$ is its original concentration, X_{target} is the target concentration of the varied component, and $X_{target,base}$ is its original concentration. This maintains relative ratios between non-target components while ensuring total composition remains 100%. We also examine wellhead pressure effects through direct parameter variation.

14.1 Acid and sour gas

We analyze how CO_2 and H_2S concentrations affect field CI (Figure 66). Sub-figure A tests CO_2 levels from 0% to 70%. This range matches all CO_2 concentrations in current LNG fields. At low CO_2 levels, gas fields maintain stable CI. Above 30% CO_2, their CI rises sharply. Dry gas fields show the strongest response to CO_2 increases. Rich gas fields follow a similar but less steep pattern. Oil fields show the smallest changes with rising CO_2. Sub-figure B shows responses to H_2S content up to 40%. Rich gas fields and oil fields react more strongly than dry gas fields. Oil fields show the highest increase in CI per unit of H_2S added. The model shows an artificial drop at 15% H_2S. It reflects a current limit in OPGEE's processing calculations that requires updates in future versions.

14.2 Methane

We analyze how methane (CH_4) content affects field CI from 1% to 100% methane (Figure 67). Rich gas fields show minimal changes in CI across all methane levels. This stability comes from their

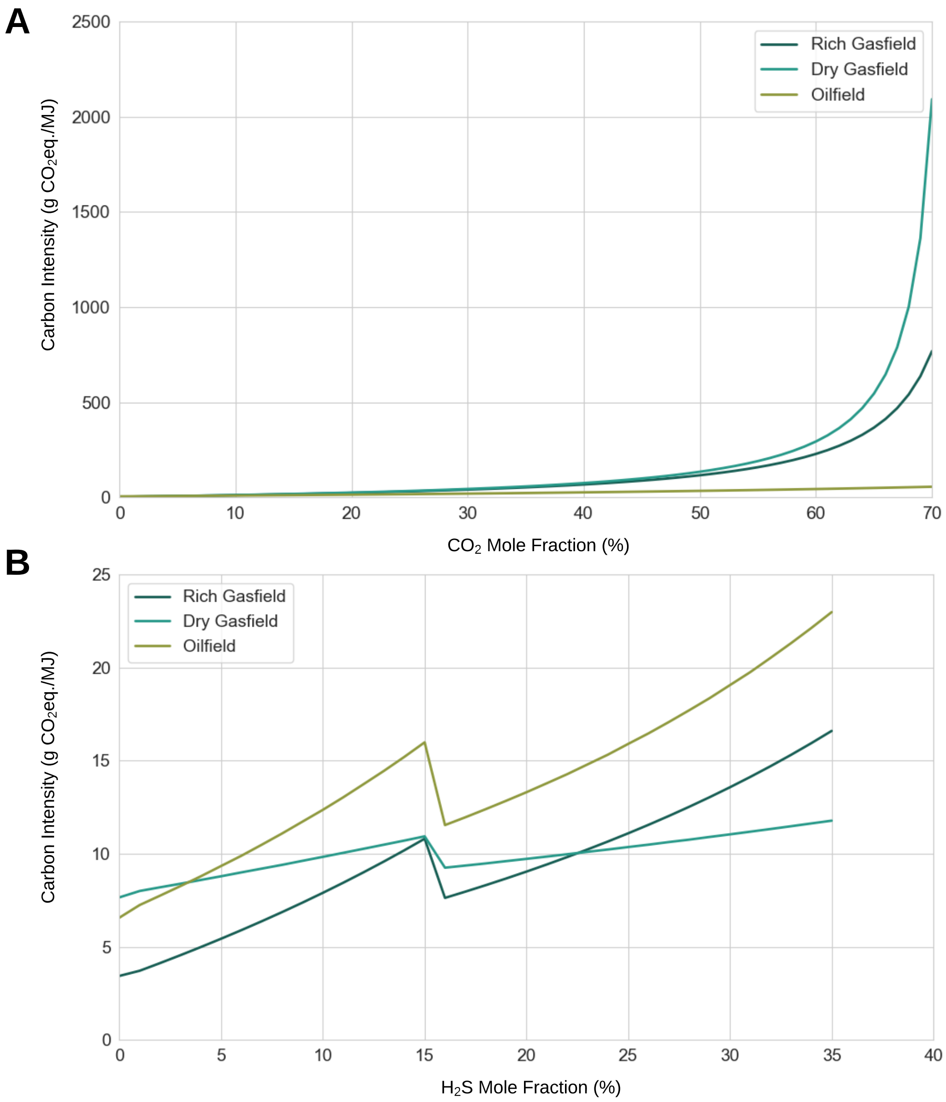

Figure 66: **Field carbon intensity changes with acid and sour gas content.** (**A**) CI rises sharply above 30% CO_2 in gas fields. Dry gas fields (light blue) show the largest increases. (**B**) Rich gas fields and oil fields show rapid increases with H_2S content. Model cannot process H_2S levels above 15%.

large production of other hydrocarbons and oil. Dry gas fields and oil fields show strong responses to methane content. Below 10% CH_4, their CI rises sharply. Above 10%, both field types show linear increases as methane content drops. Most LNG fields contain over 80% methane. However, some fields with very low methane content (<10%) can have very high CI. Notably, current satellites can only detect methane emissions. They cannot measure other hydrocarbon components leaks. This means we might underestimate emissions from fields with low methane content only using the measurement-based approach.

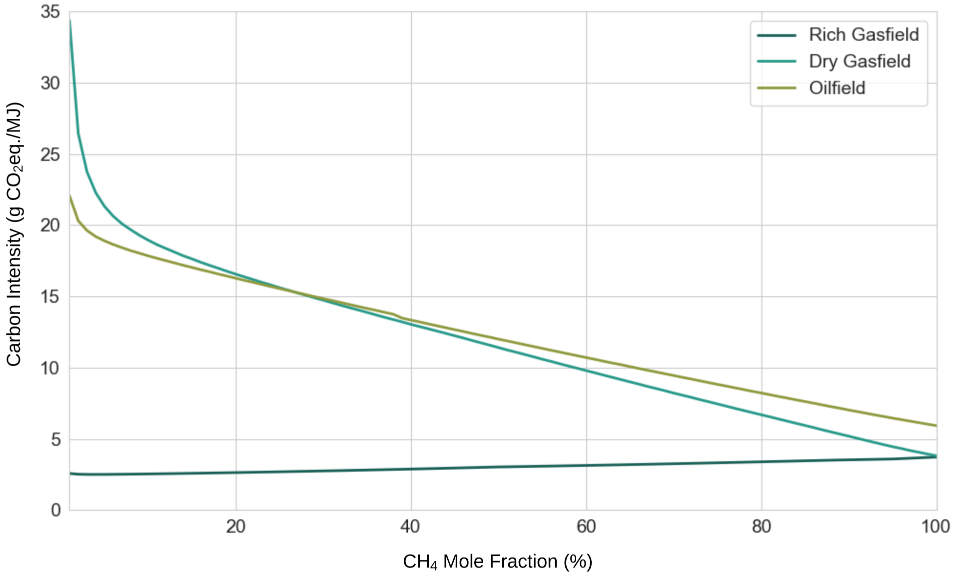

Figure 67: **Field carbon intensity response to methane content.** CI versus methane mole fraction for three field types. Rich gas fields (dark blue) show minimal changes. Dry gas fields (light blue) and oil fields (green) show exponential increases below 10% methane and linear changes above. Most active fields contain over 80% methane.

14.3 Wellhead pressure

We analyze how wellhead pressure affects field CI (Figure 68). Gas fields require higher pressures to meet pipeline specifications. We test pressures from 20 to 800 psi, where 800 psi is assumed to be the pipeline inlet pressure in this study. For oil fields processing associated gas, we examine pressures from 10 to 500 psi. Gas fields show rapid CI drops up to 500 psi. Beyond this point, additional pressure increases yield smaller benefits. Rich and dry gas fields show parallel decreases, suggesting similar compression energy requirements despite different production profiles. Oil fields display steepest CI reductions below 300 psi, with minimal improvements at higher pressures.

14.4 Gas transmission

Gas transmission is a key factor in capturing high-resolution CI differences across the LNG value chain. As discussed in Section 4, gas transmission contributes to the total well-to-liquefaction CI

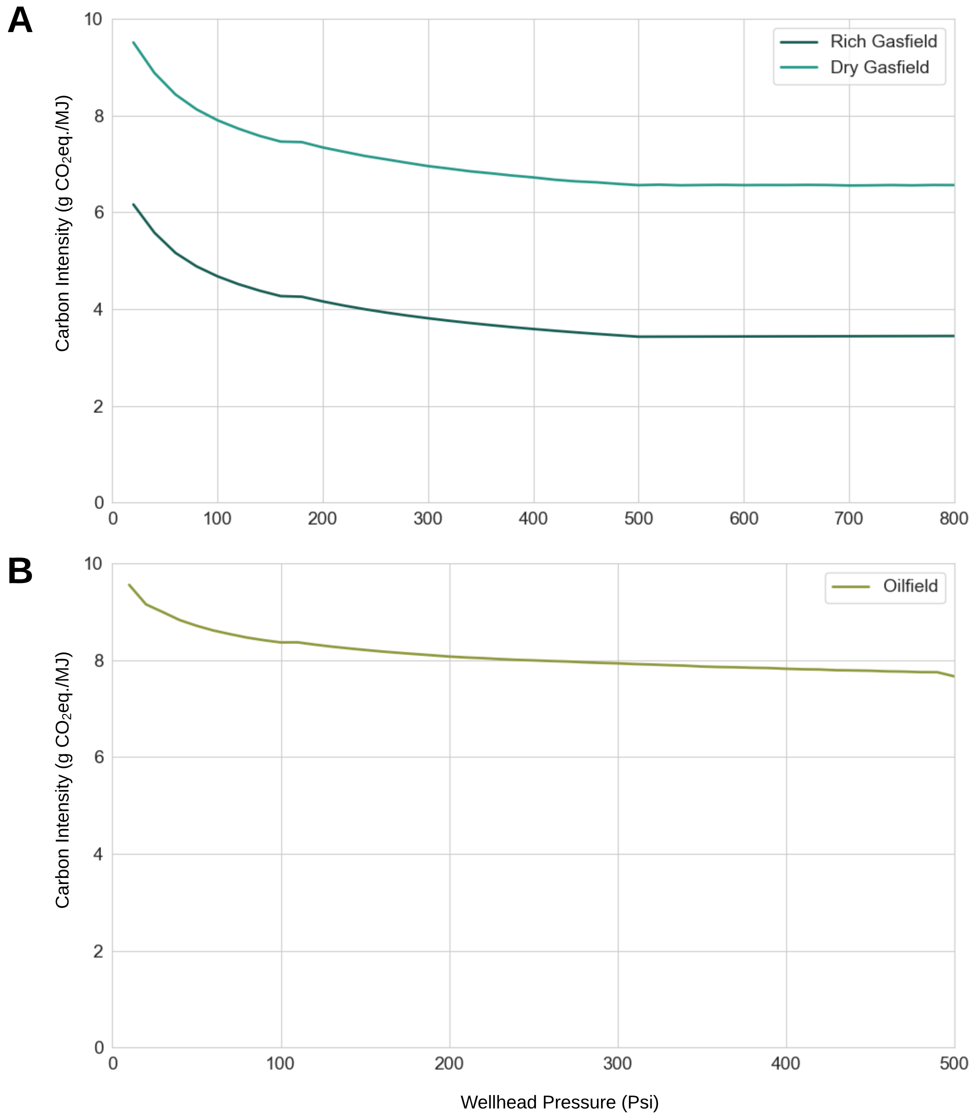

Figure 68: **Field carbon intensity changes with wellhead pressure.** (**A**) Gas field CI versus wellhead pressure (20-800 psi). Both rich (dark blue) and dry (light blue) gas fields show rapid decreases below 500 psi. (**B**) Oilfield response to pressure changes (10-500 psi). Steepest reductions occur below 300 psi.

in a very limited fraction, but its tractability is critical. This section explores a scenario in which we do not model gas transmission details, and we examine how that assumption affects liquefaction terminal CI estimates.

Without transmission modeling, all terminals within each country would be assigned the same country-average CI. Figure 69 shows a comparison of terminal CI with and without gas transmission modeling. When transmission is excluded (teal bars), all terminals within each country have identical

CI values, eliminating the natural variability that exists between facilities. Including transmission (red bars) reveals significant differences among terminals within the same country.

The importance of modeling transmission becomes particularly evident in countries with multiple terminals. In Australia, transmission modeling shows CI values ranging from 9.0 g CO_2eq./MJ (Pluto) to 20.1 g CO_2eq./MJ (Gladstone), compared to a uniform 12.5 g CO_2eq./MJ without transmission. Similarly dramatic differences appear in Indonesia, where Tangguh shows 26.1 g CO_2eq./MJ with transmission modeling versus the country average of 18.7 g CO_2eq./MJ, while Bontang drops to 11.1 g CO_2eq./MJ. Even in Algeria, Skikda's CI decreases from 16.1 g CO_2eq./MJ to 12.5 g CO_2eq./MJ when transmission is properly modeled.

Our findings demonstrate that excluding gas transmission details obscures terminal-level variability in emissions. Accurate modeling of gas transmission pipelines is essential for stakeholders who need site-specific emission intensities and for properly differentiating between terminals within the same country.

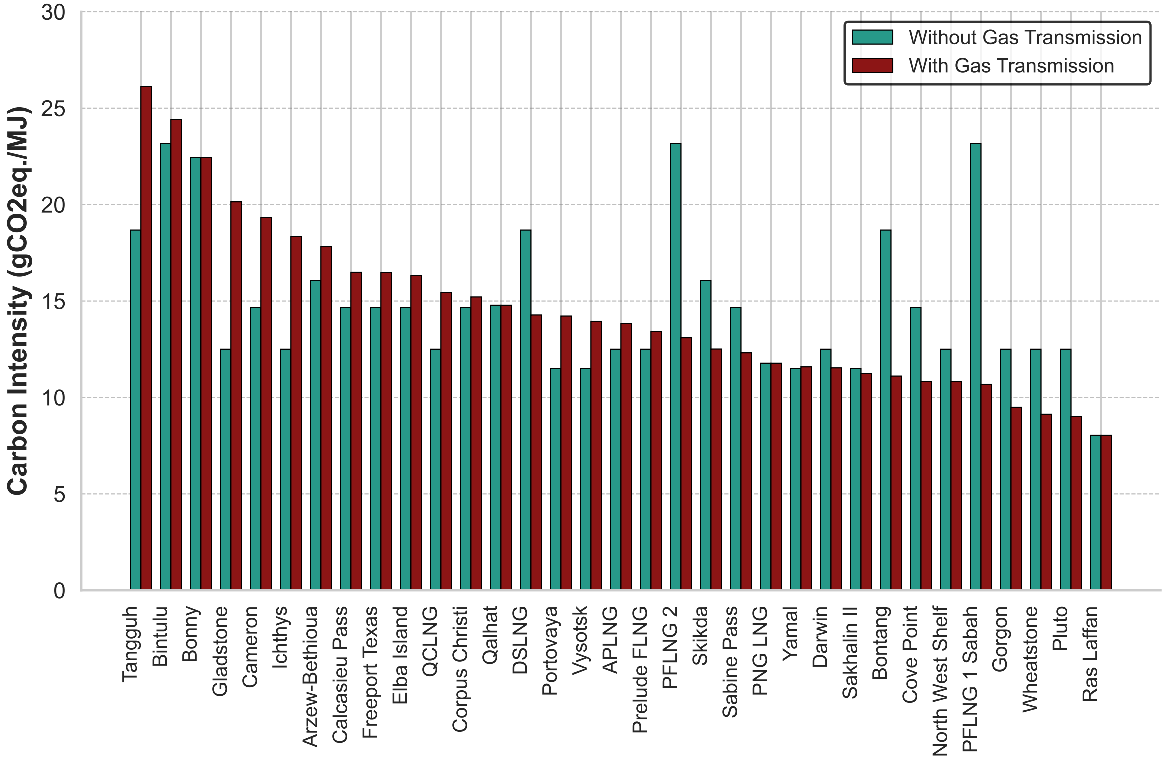

Figure 69: **Comparison of terminal-level CI with and without transmission modeling.** Teal bars represent CI without transmission modeling (using country averages), while red bars include terminal-specific transmission effects. Without transmission modeling, all terminals within each country have identical CI values (e.g., all Australian terminals at 12.5 g CO_2eq./MJ). Including transmission reveals significant differences among terminals, such as Australia's range from 9.0 to 20.1 g CO_2eq./MJ and Indonesia's range from 11.1 to 26.1 g CO_2eq./MJ.

15 Economic analysis

We conducted an economic analysis to understand how different carbon prices could affect LNG export terminal prices. The base LNG price data comes from different sources: WoodMac provides terminal-level prices for non-US exporters, while EIA Henry Hub prices (which are country-level) are used for US terminals. Both reflect yearly averages from 2022. We tested three carbon price levels: \$40, \$80, and \$120 per tonne of CO_2, which represent low, medium, and high ends of possible carbon policies. By comparison, current carbon costs for steel and cement under the EU Carbon Border Adjustment Mechanism (CBAM) are in a similar range of \$40–\$80 per tonne, with discussions of increasing these further (*52*).

Figure 70 illustrates the impact of carbon pricing on final LNG prices for each export terminal. The dark blue bars represent the base LNG price (without any carbon cost), while the lighter colored segments show the additional costs under each carbon price scenario (\$40/tCO_2 in blue, \$80/tCO_2 in purple, and \$120/tCO_2 in red). Error bars indicate the price variation based on low and high emission intensity estimates for each terminal.

The impact of carbon pricing varies significantly across terminals. Qatar's Ras Laffan terminal, with the lowest CI among major exporters, sees the smallest price increases: only \$0.34 increments at \$40/tCO_2, \$0.68 at \$80/tCO_2, and \$1.02 at \$120/tCO_2. Several Australian terminals, including Pluto, Gorgon, and Wheatstone, also experience relatively modest price increases. In contrast, terminals with higher CI face more substantial price impacts. Indonesia's Tangguh terminal would see the largest increases, with prices rising by \$1.10, \$2.20, and \$3.31 per MMBtu at the three respective carbon price levels. Similarly, Malaysia's Bintulu facility would experience increases of \$1.03, \$2.06, and \$3.09 per MMBtu.

Under the highest carbon price scenario (\$120/tCO_2), most terminals would see price increases ranging from 7% to 25% above their base prices. For terminals with lower base prices but higher emissions, such as Tangguh (base price of \$9.84/MMBtu), the percentage increase is particularly significant at approximately 34%. These findings suggest that carbon pricing could significantly impact the competitive landscape of global LNG markets, potentially altering trade flows as buyers prioritize lower-carbon sources to mitigate cost impacts.

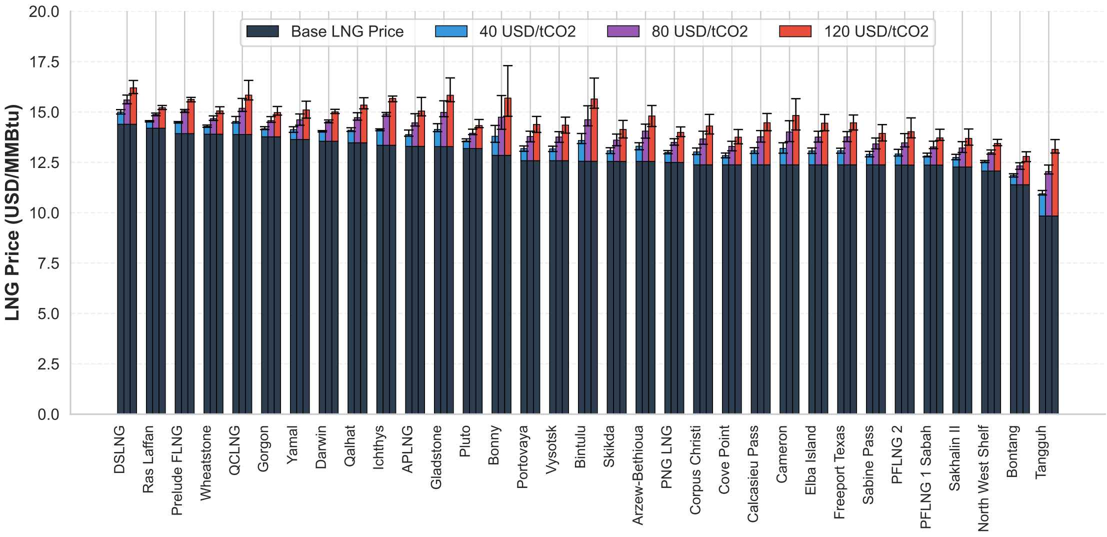

Figure 70: **Impact of carbon prices on LNG export prices.** The dark blue bars show base LNG prices at each export terminal without carbon costs. Colored segments represent additional costs under three carbon price scenarios: \$40/tCO_2 (blue), \$80/tCO_2 (purple), and \$120/tCO_2 (red). Error bars indicate price variation based on low and high emission intensity estimates. Terminals are arranged in descending order of base price. Qatar's Ras Laffan terminal shows the smallest carbon price impacts, while high-emission terminals like Indonesia's Tangguh and Malaysia's Bintulu face more substantial price increases.

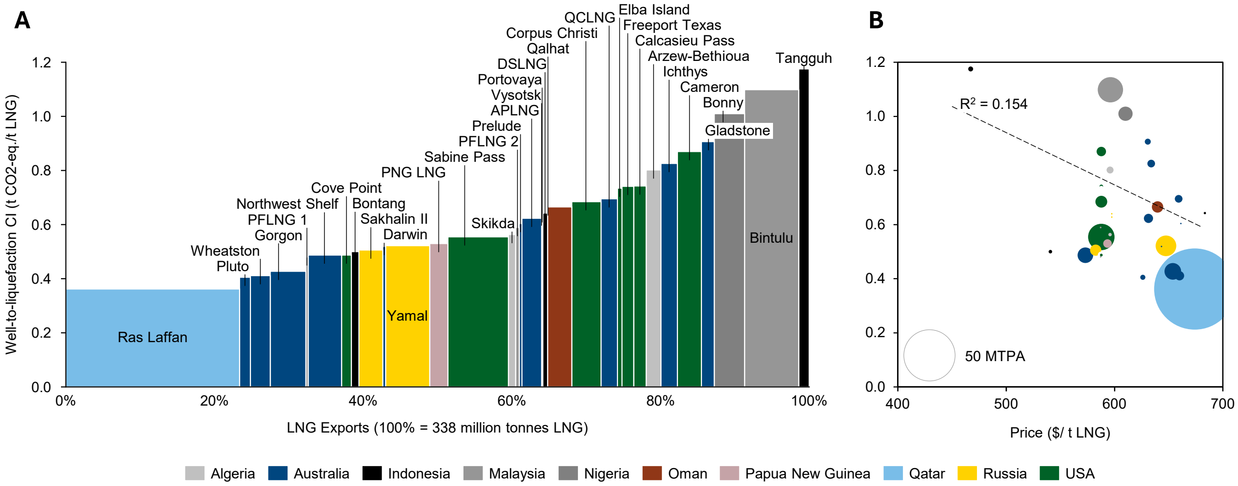

Figure 71: **Carbon intensity and terminal price across global LNG export projects. (A)** Mekko chart presenting the global LNG export supply curve, illustrating well-to-liquefaction carbon intensity (t CO_2eq. per t LNG) across individual projects. **(B)** Parity plot comparing project-level carbon intensity with estimated terminal price (USD/t LNG). Circle size indicates annual LNG export capacity, with larger circles representing higher capacities. Color intensity reflects emissions levels, with red denoting higher carbon intensity and blue indicating lower intensity. The weak correlation (R^2 = 0.15) highlights that emissions performance and price are not systematically aligned. Some project labels have been omitted for clarity; see SM for the complete data table.

16 Comparing against previous studies

16.1 Methane loss rate comparison

We evaluated our methane loss rate estimates against the International Energy Agency (IEA) methodology for upstream gas emissions (*23*). The IEA uses country-specific scaling factors relative to a U.S. baseline to account for variations in methane emissions across global natural gas production regions. To perform a systematic comparison, we calculated equivalent scaling factors using our country-level MLR results.

Table 33 presents methane intensities from this study across major LNG-exporting countries. These values represent the percentage of gas production emitted as methane across the supply chain. Nigeria shows the highest average MLR (14.95%), significantly exceeding other exporters. Malaysia follows with 3.94%, while the remaining countries range between 1.25% (Qatar) and 2.31% (Oman). The U.S., used as our reference case, shows an average MLR of 1.61%.

Table 33: **Methane loss rate by country from LNG CI analysis.** Values represent percentage of gas production emitted as methane, showing significant variations across exporting regions.

Country	Low	Average	High
Algeria	0.92%	1.64%	2.41%
Australia	1.03%	1.32%	1.97%
Indonesia	1.79%	2.15%	2.69%
Malaysia	3.24%	3.94%	5.57%
Nigeria	11.86%	14.95%	20.53%
Oman	1.97%	2.31%	2.97%
Papua New Guinea	1.22%	1.57%	2.02%
Qatar	1.09%	1.25%	1.44%
Russia	0.91%	1.55%	2.26%
USA (Reference)	1.01%	1.61%	2.29%

To compare with IEA's approach, we calculated country-specific scaling factors relative to the U.S. baseline using Equation 57:

$$SF_{country} = \frac{MLR_{country}}{MLR_{US}} \tag{57}$$

where $SF_{country}$ is the scaling factor for a specific country, $MLR_{country}$ is that country's MLR, and MLR_{US} is the U.S. MLR. To account for uncertainty ranges, we calculated lower and upper bounds using Equation 58:

$$SF_{low} = \frac{MI_{country,low}}{MI_{US,high}} \quad \text{and} \quad SF_{high} = \frac{MI_{country,high}}{MI_{US,low}} \tag{58}$$

Table 34 compares our calculated scaling factors with IEA values for upstream gas emissions. Our results show strong alignment with IEA factors for several countries, particularly Algeria (our average: 1.02, IEA: 2.1), Indonesia (1.33 vs. 2.1), and Russia (0.96 vs. 1.7). Other countries show similar relative rankings between methods. The most significant divergence appears for Nigeria, where this study indicates substantially higher relative emissions (9.26) compared to IEA's estimate (2.4), suggesting potential underestimation in the IEA approach for this region.

Table 34: **Methane emission scaling factors relative to U.S. baseline.** Comparison between our calculated scaling factors and IEA upstream gas factors shows general alignment in relative rankings with some significant quantitative differences.

Country	Low Bound	Average	High Bound	IEA Upstream Gas
Algeria	0.40	1.02	2.38	2.1
Australia	0.45	0.82	1.95	0.6
Indonesia	0.78	1.33	2.66	2.1
Malaysia	1.42	2.44	5.52	1.5
Nigeria	5.18	9.26	20.33	2.4
Oman	0.86	1.43	2.94	1.0
Papua New Guinea	0.53	0.97	2.00	–
Qatar	0.47	0.77	1.43	1.0
Russia	0.40	0.96	2.24	1.7

The broad alignment between our empirically-derived scaling factors and IEA's methodology provides mutual validation for both approaches. Countries with similar scaling factors across methodologies (Algeria, Russia) suggest robust characterization of relative emission patterns. Discrepancies, particularly for Nigeria and Malaysia, highlight regions where measurement-based approaches may capture emissions sources overlooked by inventory-based methods. These differences underscore the value of combining multiple methodological approaches for comprehensive emissions accounting across diverse production regions.

16.2 OPGEE version comparison

We compare our Python version against OPGEE v2.0c (*14*). Our Python version includes several key improvements over v2.0c. These improvements include better handling of multiphase flow in wellbores, more accurate pressure calculations using thermodynamic properties, updated water injection modeling, and the inclusion of gas gathering systems. The Python version also allocates fugitive emissions by process rather than aggregating them (*53*). These enhancements are described in Dixit et al. (2023). Other major updates include more accurate cumulative production calculations incorporating both oil and gas energy content, refined pressure calculations using field-specific thermodynamic data, more accurate water injection calculations with updated gravitational gradient (0.433 psi/ft), process-specific allocation of fugitive and operational venting emissions, and integration of vapor recovery units in the crude oil storage system.

Figure 72 shows CI estimates from both versions across all LNG exporters. The Python version generally predicts higher CI. This is due to improved emissions modeling and the inclusion of superemitter data. Only Oman shows lower values in the Python version, reflecting its minimal superemitter emissions. Combustion emissions are also generally higher in the Python version. However, Australia, Oman, and Qatar show slight decreases. These results suggest that OPGEE v2.0c may underestimate LNG field emissions.

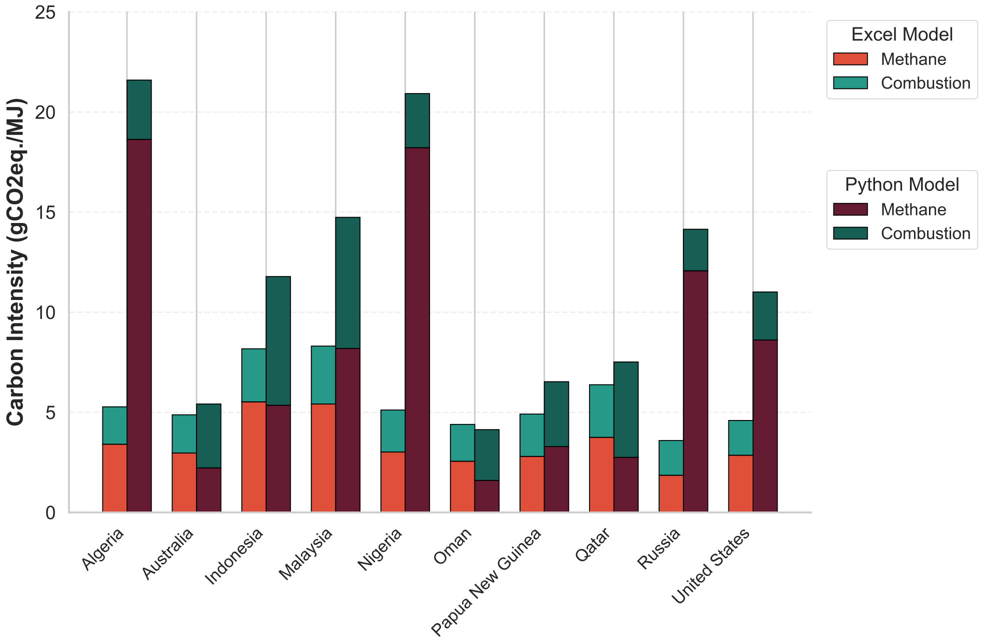

Figure 72: **Comparison of carbon intensity estimates between OPGEE versions.** Stacked bars show methane (red/purple) and combustion (teal/green) emissions for Excel v2.0c and Python versions. Python version shows consistently higher total emissions except for Oman. Error fields from Excel version were excluded.

16.3 Comparison with Gan et al. LNG model

The LNG CI model developed by Gan et al. (*10*) provides another perspective for analyzing emissions in LNG production. This study specifically focuses on fields that supply LNG to China. While their model covers the complete LNG chain from upstream operations through liquefaction, shipping, and regasification, we focus our discussion on their upstream CI calculation approach.

Their model adopts different assumptions from this study, particularly in field characterization. They model all gas fields as dry gas fields without liquid production, which leads to several simplifications: no water, condensate, or oil production is considered; no pumping units are required for production; no energy is allocated to water treatment; and no natural gas liquids (NGLs) are extracted.

The processing system in their model includes basic operations. The main processes considered are gas dehydration and acid gas removal, with CO_2 from acid gas treatment classified as flaring emissions. Their model uses specific operating conditions that differ from our assumptions: wellhead pressure of 50 psia, processing pressure of 800 psia, wellhead temperature of 197°F, and all streams at standard conditions.

Their analysis reveals variations in CI across China's LNG supplier countries. Production and extraction account for the largest share of emissions, reaching 13.33 gCO_2/MJ in Malaysia. This observation aligns with our wellhead pressure sensitivity analysis discussed in Section 14.3. Their results show that venting emissions, primarily from CO_2 removal, constitute a significant portion of total emissions, while surface processing contributes relatively less across all regions.

Their approach differs from this study in several aspects: superemitter emissions are not included; gas composition effects on compression are not considered; real gas behavior (Z-factor) is not incorporated; and driver fuel consumption is treated as constant.

They utilize emission factors from the Greenhouse Gas Reporting Program for emissions calculations, covering liquid unloading, well workover, well completion, and well leakage. Their model also incorporates CO_2 capture considerations, specifically a 90% capture rate for the Chang & Song field in China. This regional focus on China's LNG value chain provides valuable insights for understanding CI in a specific market context.

16.4 Liquefaction validation

To validate our liquefaction CI estimates, we compared our results with established literature values from Gan et al. (2020) (*10*). For alignment, we updated Gan's emissions factors (originally reported in Btu per kilogram of natural gas) to g CO_2eq./MJ using a conversion factor of 18.18, with base emission factors of 71,000 gCO_2eq./MMBtu for natural gas combustion and 79,200 gCO_2eq./MMBtu for diesel combustion. Table 35 presents a side-by-side comparison of CI estimates from both approaches across the global LNG liquefaction fleet, organized by country and facility.

This study reveals several significant patterns. The SGE-based model generally produces lower CI estimates, with a global average of 2.90 g CO_2eq./MJ compared to 5.32 g CO_2eq./MJ in Gan et al.'s approach. This difference stems from our process-based modeling, which accounts for facility-specific technological configurations, heat integration strategies, and operational efficiencies. While Gan et al. assigned similar emission factors within countries (e.g., all Russian facilities at 5.32 g CO_2eq./MJ), our model identifies significant intra-country variations. Russian facilities range from 1.91 g CO_2eq./MJ (Yamal) to 3.06 g CO_2eq./MJ (Portovaya), reflecting technology differences not captured in the emission factor approach. Floating LNG facilities (Prelude FLNG, PFLNG 1 Sabah, PFLNG 2) show substantially lower emissions in our model (1.49-1.88 g CO_2eq./MJ) compared to Gan et al.'s estimates (5.32-5.37 g CO_2eq./MJ), reflecting advanced technology and higher efficiency standards in these newer facilities.

Conversely, our model identifies several high-emission outliers, particularly three U.S. facilities (Calcasieu Pass, Elba Island, and Freeport Texas) with CI of 5.87-6.73 g CO_2eq./MJ, significantly higher than Gan et al.'s uniform 4.82 g CO_2eq./MJ for all U.S. facilities. The most dramatic divergence occurs with Australia's Ichthys facility (10.26 g CO_2eq./MJ vs. 5.37 g CO_2eq./MJ), reflecting complex processing requirements and unusually high flaring rates during the assessment period. Indonesian facilities show the largest systematic reduction, with our estimates (1.94-2.03 g CO_2eq./MJ) substantially lower than Gan et al.'s uniform 6.50 g CO_2eq./MJ, resulting from our more accurate accounting of recent efficiency improvements and technological upgrades.

Overall, while both approaches identify similar broad patterns, our SGE-based methodology provides more nuanced insights by incorporating actual operational data, technological configurations, and process-level emissions accounting. This comparison demonstrates that emission-factor

Table 35: **Comparison of carbon intensity estimates between Gan et al. (2020) and our SGE-based approach.** Values are presented in g CO_2eq./MJ. The SGE-based approach generally produces lower CI estimates, particularly for facilities with advanced technologies and operational optimization.

Country	Liquefaction Terminal	Gan et al. (2020)	SGE-based Model
Algeria	Arzew-Bethioua	5.32	2.39
Algeria	Skikda	5.32	2.21
Australia	APLNG	5.14	2.11
Australia	Darwin	5.14	2.10
Australia	Gladstone	5.37	2.05
Australia	Gorgon	5.37	1.99
Australia	Ichthys	5.37	10.26
Australia	North West Shelf	5.37	2.02
Australia	Pluto	5.37	2.01
Australia	Prelude FLNG	5.37	1.88
Australia	QCLNG	5.14	2.07
Australia	Wheatstone	5.37	1.95
Indonesia	Bontang	6.50	2.03
Indonesia	DSLNG	6.50	2.03
Indonesia	Tangguh	6.50	1.94
Malaysia	Bintulu	5.32	1.60
Malaysia	PFLNG 1 Sabah	5.32	1.50
Malaysia	PFLNG 2	5.32	1.49
Nigeria	Bonny	5.46	1.93
Oman	Qalhat	4.43	2.03
Papua NG	PNG LNG	6.53	2.12
Qatar	Ras Laffan	4.98	2.00
Russia	Portovaya	5.32	3.06
Russia	Sakhalin II	5.32	2.07
Russia	Vysotsk	5.32	2.79
Russia	Yamal	5.32	1.91
United States	Calcasieu Pass	4.82	5.87
United States	Cameron	4.82	2.08
United States	Corpus Christi	4.82	1.99
United States	Cove Point	4.82	2.04
United States	Elba Island	4.82	6.22
United States	Freeport Texas	4.82	6.73
United States	Sabine Pass	4.82	2.07

approaches may overestimate emissions for advanced facilities while potentially missing significant emissions from specific high-intensity operations.

References and Notes

1. Office of Fossil Energy and Carbon Management, Liquefied Natural Gas (LNG), U.S. Department of Energy (2021), the United States is the world's largest producer of natural gas, with significant international LNG trade and a focus on regulatory oversight for LNG exports.

2. A. R. Brandt, *et al.*, OPGEE v3.0b User Guide And Technical Documentation, GitHub (2022).

3. W. Long, *Improving the Oil Production Greenhouse Gas Emissions Estimator (OPGEE): Validation, Modeling, and System Design*, Ph.D. thesis, Stanford University, Stanford, California (2023), submitted to the Department of Energy Resources Engineering. Degree committee members include Adam Brandt, Ines Azevedo, and Anthony Kovscek. Associated with Stanford Doerr School of Sustainability.

4. M. S. Masnadi, *et al.*, Global carbon intensity of crude oil production. *Science* **361** (6405), 851–853 (2018), doi:10.1126/science.aar6859.

5. S. T. Brennan, J. L. Rivera, B. Varela, A. J. Park, L. A. Agyepong, Natural Gas Compositional Analyses Dataset of Gases from United States Wells, U.S. Geological Survey (2021), doi: 10.5066/P9TR93E3, this dataset documents natural occurrences of helium and carbon dioxide in gases from wells across the United States and is sourced primarily from publicly available data from the Bureau of Land Management and the U.S. Geological Survey.

6. R. Allis, *et al.*, Natural CO2 reservoirs on the Colorado Plateau and southern Rocky Mountains: Candidates for CO2 sequestration, in *Proceedings of the First National Conference on Carbon Sequestration* (U.S. Department of Energy, National Energy Technology Laboratory) (2001), pp. 14–17.

7. N. S. Huang, G. E. Aho, B. H. Baker, T. R. Matthews, R. J. Pottorf, Integrated Reservoir Modeling of a Large Sour-Gas Field With High Concentrations of Inerts. *SPE Reservoir Evaluation & Engineering* **14** (4), 418–432 (2011), doi:10.2118/146082-PA.

8. United States Environmental Protection Agency, Monitoring, Reporting and Verification (MRV) Plan for Shute Creek Facility, United States Environmental Protection Agency (2019),

mRV Plan Approval Number 1002150-2. The MRV plan is approved for the Shute Creek Facility under 40 CFR Part 98, Subpart RR of the Greenhouse Gas Reporting Program.

9. A. Ali, V. Mehta, D. O. Ogbe, V. A. Kamath, S. L. Patil, Fluid Characterization for Compositional Simulation with Application to Endicott Field, Alaska, in *SPE Western Regional Meeting*, vol. SPE Western Regional Meeting (1994), pp. SPE–27874–MS, doi:10.2118/27874-MS.

10. Y. Gan, *et al.*, Carbon footprint of global natural gas supplies to China. *Nature Communications* **11** (1), 824 (2020), doi:10.1038/s41467-020-14606-4.

11. M. S. Masnadi, *et al.*, Well-to-refinery emissions and net-energy analysis of China's crude-oil supply. *Nature Energy* **3** (3), 220–226 (2018), doi:10.1038/s41560-018-0090-7.

12. H. M. El-Houjeiri, A. R. Brandt, Oil Production Greenhouse Gas Emissions Estimator (OPGEE) (2012).

13. H. M. El-Houjeiri, A. R. Brandt, J. E. Duffy, Open-Source LCA Tool for Estimating Greenhouse Gas Emissions from Crude Oil Production Using Field Characteristics. *Environmental Science & Technology* **47** (11), 5998–6006 (2013), doi:10.1021/es304570m.

14. H. M. El-Houjeiri, M. S. Masnadi, K. Vafi, J. Duffy, A. R. Brandt, Oil Production Greenhouse Gas Emissions Estimator OPGEE v2.0 User Guide & Technical Documentation, Stanford University (2017).

15. M. S. Masnadi, *et al.*, Oil Production Greenhouse Gas Emissions Estimator (OPGEE v3.0a) User Guide & Technical Documentation, Stanford University (2019), cited by 5.

16. M. S. Masnadi, P. R. Perrier, J. Wang, J. Rutherford, A. R. Brandt, Statistical Proxy Modeling for Life Cycle Assessment and Energetic Analysis. *Energy* **194**, 116882 (2020), doi:10.1016/j.energy.2019.116882.

17. J. S. Rutherford, *et al.*, Closing the methane gap in US oil and natural gas production emissions inventories. *Nature Communications* **12** (1), 4715 (2021), doi:10.1038/s41467-021-25017-4.

18. American Petroleum Institute, Fugitive Hydrocarbon Emissions from Oil and Gas Production Operations, API Publication Number 4589 (1993), prepared under contract by Star Environmental, Torrance, CA.

19. Z. Zhang, E. D. Sherwin, A. R. Brandt, Estimating global oilfield-specific flaring with uncertainty using a detailed geographic database of oil and gas fields. *Environmental Research Letters* **16** (12), 124039 (2021), doi:10.1088/1748-9326/ac3956.

20. G. Plant, *et al.*, Inefficient and unlit natural gas flares both emit large quantities of methane. *Science* **377** (6614), 1566–1571 (2022), doi:10.1126/science.abq0385.

21. T. Lauvaux, *et al.*, Global assessment of oil and gas methane ultra-emitters. *Science* **375** (6580), 557–561 (2022), doi:10.1126/science.abj4351.

22. J.-P. W. MacLean, *et al.*, Offshore methane detection and quantification from space using sun glint measurements with the GHGSat constellation. *Atmospheric Measurement Techniques* **17** (2), 863–874 (2024), doi:10.5194/amt-17-863-2024.

23. International Energy Agency (IEA), Global Methane Tracker 2024, IEA (2024), licence: CC BY 4.0.

24. J.-P. W. MacLean, *et al.*, Offshore methane detection and quantification from space using sun glint measurements with the GHGSat constellation. *EGUsphere* **2023**, 1–18 (2023), doi: 10.5194/egusphere-2023-1772.

25. A. Foulds, *et al.*, Quantification and assessment of methane emissions from offshore oil and gas facilities on the Norwegian continental shelf. *Atmospheric Chemistry and Physics* **22** (7), 4303–4322 (2022), doi:10.5194/acp-22-4303-2022.

26. J. D. Maasakkers, *et al.*, Global distribution of methane emissions, emission trends, and OH concentrations and trends inferred from an inversion of GOSAT satellite data for 2010–2015. *Atmospheric Chemistry and Physics* **19** (11), 7859–7881 (2019), doi:10.5194/acp-19-7859-2019.

27. X. Lu, *et al.*, Methane emissions in the United States, Canada, and Mexico: evaluation of national methane emission inventories and 2010–2017 sectoral trends by inverse analysis of

in situ (GLOBALVIEWplus CH_4 ObsPack) and satellite (GOSAT) atmospheric observations. *Atmospheric Chemistry and Physics* **22** (1), 395–418 (2022), doi:10.5194/acp-22-395-2022.

28. Z. Chen, *et al.*, Satellite quantification of methane emissions and oil–gas methane intensities from individual countries in the Middle East and North Africa: implications for climate action. *Atmospheric Chemistry and Physics* **23** (10), 5945–5967 (2023), doi: 10.5194/acp-23-5945-2023.

29. T. R. Scarpelli, *et al.*, Updated Global Fuel Exploitation Inventory (GFEI) for methane emissions from the oil, gas, and coal sectors: evaluation with inversions of atmospheric methane observations. *Atmospheric Chemistry and Physics* **22** (5), 3235–3249 (2022), doi: 10.5194/acp-22-3235-2022.

30. G. Janssens-Maenhout, *et al.*, EDGAR v4.3.2 Global Atlas of the three major greenhouse gas emissions for the period 1970–2012. *Earth System Science Data* **11** (3), 959–1002 (2019), doi:10.5194/essd-11-959-2019.

31. E. D. Sherwin, *et al.*, US oil and gas system emissions from nearly one million aerial site measurements. *Nature* **627** (8003), 328–334 (2024), doi:10.1038/s41586-024-07117-5.

32. E. D. Sherwin, *et al.*, Single-blind test of nine methane-sensing satellite systems from three continents. *Atmospheric Measurement Techniques* **17** (2), 765–782 (2024), doi:10.5194/amt-17-765-2024.

33. Environmental Defense Fund, New MethaneSAT Data Reveal Previously Undetectable Methane Emissions, https://data.methanesat.org (2025), published March 7, 2025. Accessed April 20, 2025. Environmental Defense Fund.

34. Carbon Mapper Coalition, New Methane Data from Tanager-1 Satellite Added to Carbon Mapper's Portal, https://data.carbonmapper.org (2025), published February 5, 2025. Accessed April 20, 2025. Public methane and carbon dioxide plume data from Tanager-1, covering over 25 countries and multiple sectors.

35. GHGSat Inc., GHGSat Announces Rapid Expansion, Nearly Doubling its Fleet of Methane Emissions-Monitoring Satellites by 2026, https://www.ghgsat.com/en/newsroom/press-

releases/ghgsat-announces-rapid-expansion-nearly-doubling-its-fleet-of-methane-emissions-monitoring-satellites-by-2026 (2024), press release published November 10, 2024. Accessed April 20, 2025. GHGSat will add nine new satellites to expand methane monitoring capability and support global emissions mitigation efforts.

36. E. Winarno, W. Hadikurniawati, R. N. Rosso, Location based service for presence system using haversine method, in *2017 International Conference on Innovative and Creative Information Technology (ICITech)* (2017), pp. 1–4, doi:10.1109/INNOCIT.2017.8319153.
37. E. W. Dijkstra, A note on two problems in connexion with graphs. *Numerische Mathematik* **1** (1), 269–271 (1959), doi:10.1007/BF01386390.
38. S. Xu, *et al.*, Life cycle assessment of carbon emission from natural gas pipelines. *Chemical Engineering Research and Design* **185**, 267–280 (2022), doi:10.1016/j.cherd.2022.07.018.
39. G. Molnar, Economics of gas transportation by pipeline and LNG, in *The Palgrave Handbook of International Energy Economics* (Springer International Publishing Cham), pp. 23–57 (2022).
40. NaturalGas.org, The Transportation of Natural Gas, Natural gas pipeline and transportation overview (2013), accessed.
41. *ASME B31.8-2003: Gas Transmission and Distribution Piping Systems*, Tech. Rep. B31.8-2003, American Society of Mechanical Engineers, New York, NY (2003).
42. C. Trozzi, R. De Lauretis, International maritime navigation, international inland navigation, national navigation (shipping), national fishing, military (shipping), and recreational boats, in *EMEP/EEA Air Pollutant Emission Inventory Guidebook 2019* (European Environment Agency), pp. 28–30 (2020), oct 2020 Update.
43. US EPA, Regulatory Impact Analysis: Control of Emissions of Air Pollution from Category 3 Marine Diesel Engines (2009).
44. T. Sturtz, M. Zatko, C. Lindhjem, G. Yarwood, Ocean-Going Tanker Vessel Lightering Emissions in the Gulf of Mexico, Ramboll Environ US Corporation (2017), work Order No. 582-17-72097-24, Contract No. 582-15-50417, Tracking No. 2017-24, prepared under contract from the Texas Commission on Environmental Quality.

45. S. A. Roman-White, *et al.*, LNG Supply Chains: A Supplier-Specific Life-Cycle Assessment for Improved Emission Accounting. *ACS Sustainable Chemistry & Engineering* **9** (32), 10857–10867 (2021), doi:10.1021/acssuschemeng.1c03307.

46. D. Dobrota, B. Lalic, I. Komar, Problem of Boil-Off in LNG Supply Chain. *Transactions on Maritime Science* **2** (2), 91–100 (2013), doi:10.7225/toms.v02.n02.001.

47. National Energy Technology Laboratory (NETL), Unit Process Library - Combustion of Diesel (2021), accessed: 2021.

48. A. Miyamoto, C. Ishiguro, The contents of this paper are the authors' sole responsibility. They do not necessarily represent the views of the Oxford Institute for Energy Studies or any of its members, Oxford Institute for Energy Studies (2018), doi:10.26889/9781784671242.

49. R. Agarwal, *et al.*, LNG Regasification Terminals: The Role of Geography and Meteorology on Technology Choices. *Energies* **10** (12), 2152 (2017), doi:10.3390/en10122152.

50. IGU World LNG Report 2017 (2017), liquefied natural gas (LNG) experienced a dynamic 2016, with global trade reaching a record 258 million tonnes (MT), an increase of 13 MT over 2015. Supply ramped up at projects spanning the globe, from the United States to Australia, and LNG found new markets in a diverse array of countries. At the same time, delays and plant outages kept supply growth subdued. LNG prices remained below the cost of new supply as demand grows to reach balance.

51. Oil and Gas Climate Initiative (OGCI), OGCI Progress Report 2024: Methane Intensity Target and Aiming for Zero Methane Emissions, OGCI's collective methane reduction achievements and targets (2024), accessed.

52. European Commission, Carbon Border Adjustment Mechanism (CBAM), https://ec.europa.eu/taxation_customs/cbam_en (2024), accessed: 18 December 2024. Content includes legislative documents, sectoral information, and guidance for the CBAM transitional and definitive phases.

53. Y. Dixit, *et al.*, Carbon intensity of global crude oil trading and market policy implications. *Nature Communications* **14** (1), 5975 (2023), doi:10.1038/s41467-023-41701-z.